Nonlinear and Multidimensional Terahertz Spectroscopy of Liquids and Crystalline Solids

Thesis by
Haw-Wei Lin

In Partial Fulfillment of the Requirements for the
Degree of
Doctor of Philosophy

CALIFORNIA INSTITUTE OF TECHNOLOGY
Pasadena, California

2024
Defended Jan 4th, 2024

Haw-Wei Lin
ORCID: 0000-0002-5208-7385

ACKNOWLEDGEMENTS

Graduate school has been a wild journey, with unexpected twists and turns. Thank you to my advisor, Geoff Blake, for supporting my scientific explorations and curiosities throughout my journey. Conversations with you always spark bright new ideas and novel things to explore. Thank you to my committee members, Bill Goddard, Scott Cushing, and Ryan Hadt, for all the insightful comments and feedback you have provided on my research projects and proposals.

Thank you to all the members of the Blake group that I have had the privilege to work with: Griffin, Olivia, Cam, Kyle, Alex, Sadie, Tomislav, Albert, Jax, Evan, and Evie. Your comradery has kept me motivated and sane through the highs and lows, especially during the late experimental nights, the unexpected instrument breakdowns, and the uncertainty of COVID times. I joined the Blake group because of the environment you created, and I truly appreciate you all. Special thanks to my grad student mentor Griffin, who helped me navigate the often confusing world of nonlinear THz spectroscopy when I first started. Thank you Kyle for always being welcoming to chat about science, food, culture, life, and everything in between. I truly enjoyed our long conversations in and out of lab.

Thank you to my collaborators, both domestic and abroad, for broadening my graduate school experience with all the expertise and perspectives you bring. Special thanks to Christine, Kim, Satoshi, Ioan, and Vladimir, for all the finished and ongoing projects that we have worked together on.

Thank you to Erik, Emily, and Xavier. I look forward to the spontaneous fun next time we meet.

Thank you to my long-time friends and high school classmates, Robert, Kenny, and CJ, for the many hotpot and board games filled holidays we spent together. It has truly been a joy to reunite with you.

Thank you to my friends from ACT, especially Yu-Li, Hsiao-Yi, Allen, Yun-Ting, Wen, Li-En, Steve, Chi-Fang, Po, and Benjamin, for all the social events and off-campus adventures. Thank you to my friends back in Taiwan. You have been a consistent source of joy online during the difficult times of COVID.

Thank you to my parents, Jason and Cynthia, for always being loving and supportive. To my siblings Peter and Wendy, I am so proud of all you have accomplished. I will

always cherish the times we get to spend together as a family in the US and back home.

ABSTRACT

The delocalized and correlated nuclear degrees of freedom in the terahertz (THz) regime strongly influences the room temperature chemical and physical properties of condensed matter systems, yet detailed understanding of the photo-induced dynamics and anharmonicities of the vibrational modes have remained elusive. In hydrogen-bonded liquids, these information facilitates the development of accurate force field models to aid simulations of biological processes of proteins and DNAs. In the field of nonlinear phononics, anharmonic lattice vibrations form the foundation for ultrafast coherent control of material properties, which has become an indispensable technique in the engineering toolbox for quantum materials. In this thesis, we demonstrate the development and application of nonlinear 1D THz Kerr effect (TKE) and 2D THz-THz-Raman (2D-TTR) ultrafast THz spectroscopies, which are specially designed to induce resonant coherent excitations of the correlative nuclear degrees of freedom in liquids and crystalline solids. By analyzing the temporal evolution of the nuclear THz-driven dynamics, insights into the excitation mechanisms, nonlinear coupling interactions, and the dominant source(s) of anharmonicity may be determined. Specifically, we developed a nonlinear imaging method based on the third-order response of electro-optic crystal GaP, which significantly improved the alignment consistency and the signal strength of 2D-TTR spectroscopy. Further, we extended an echelon-based single-shot detection scheme, originally developed in 1D TKE spectroscopy, to 2D-TTR spectroscopy, which led to up to two orders-of-magnitude reduction in acquisition time. Armed with these instrument advancements, we measured 2D-TTR spectra of liquid halogenated methanes with significantly improved signal-to-noise and a larger temporal window, which led to the identification of a novel competing sum-frequency THz excitation pathway. On the other hand, we investigated resonant driven-dynamics of the phonon-polariton modes in semiconductor $LiNbO_3$, which revealed nonlinear coupling interactions between two phonon branches that are attributed to mechanical anharmonicity. In addition, we directly observed photo-induced coherent phonon wavepackets for the layered semiconductors transition metal dichalcogenide using 1D TKE spectroscopy, which are attributed to the sum-frequency excitation pathway. These works highlight the rigorous experimental considerations and careful spectral analysis required to extract essential insight into excitation mechanisms and anharmonic contributions, while avoiding spectral artifacts due to the instrument

response function. In order to provide clarity to these often misunderstood spectroscopies in the THz regime, this thesis further summaries the theories behind 1D TKE and 2D-TTR spectroscopies and the lessons we have learned from experimental realization of these exotic instruments and the analysis of complex spectral features.

PUBLISHED CONTENT AND CONTRIBUTIONS

1. Griffin Mead, **Haw-Wei Lin**, Ioan B. Magdău, Thomas F. Miller, Geoffrey A. Blake. "Sum-frequency signals in 2D-Terahertz-Terahertz-Raman spectroscopy." *Journal of Physical Chemistry B* 124.40 (2020), pp. 8904–8908. DOI: 10.1021/acs.jpcb.0c07935

   H.W. Lin and G. Mead developed the instrument, collected all experimental data, and analyzed the results. H.W. Lin prepared parts of the publication and revised the manuscript.

2. **Haw-Wei Lin**, Griffin Mead, Geoffrey A. Blake. "Mapping $LiNbO_3$ phonon-polariton nonlinearities with 2D THz-THz-Raman spectroscopy." *Physical Review Letters*, 129 (2020), pp. 207401. DOI: 10.1103/PhysRevLett.129.207401

   H.W. Lin performed the experiments and analyzed the results. H.W. Lin prepared the manuscript with input from G. Mead and G.A. Blake.

3. **Haw-Wei Lin**, Pin-Hsun Hsieh, Griffin Mead, Geoffrey A. Blake. "Characterization of the nonlinear THz focus for 2D THz spectroscopy." *Journal of the Optical Society of America B* (2024), *Accepted*.

   H.W. Lin and P.H. Hsieh developed the technique and performed the experiments. H.W. Lin prepared the manuscript with input from P.H. Hsieh, G. Mead, and G.A. Blake.

4. Satoshi Kusaba, **Haw-Wei Lin**, Ryo Tamaki, Ikufumi Katayama, Jun Takeda, Geoffrey A. Blake. "Terahertz sum-frequency excitation of coherent optical phonons in the two-dimensional semiconductor WSe_2." (2024), *Submitted*.

   H.W. Lin and S. Kusaba contributed equally on this work. H.W. Lin and S. Kusaba performed all the experiments, analyzed the results, and developed the models. H.W. Lin and S. Kusaba and prepared the manuscript.

TABLE OF CONTENTS

Acknowledgements . . . iii
Abstract . . . v
Published Content and Contributions . . . vii
Table of Contents . . . vii
List of Illustrations . . . ix
Chapter I: Introduction . . . 1
1.1 Motivation . . . 1
1.2 Overview of chapters . . . 2
1.3 Fundamental motions in the terahertz frequency range . . . 2
Chapter II: Fundamentals of Nonlinear and Multidimensional THz Spectroscopy 12
Chapter III: Characterization of the Nonlinear THz Focus for 2D THz Spectroscopy . . . 34
3.1 Abstract . . . 34
3.2 Introduction . . . 34
3.3 Experimental Setup . . . 37
3.4 Results and Discussion . . . 38
3.5 Conclusion . . . 44
Chapter IV: Sum-Frequency Signals in 2D-Terahertz-Terahertz-Raman Spectroscopy . . . 47
4.1 Abstract . . . 47
4.2 Main text . . . 47
4.3 Supplemental information . . . 55
Chapter V: Mapping $LiNbO_3$ Phonon-Polariton Nonlinearities with 2D THz-THz-Raman Spectroscopy . . . 64
5.1 Abstract . . . 64
5.2 Main text . . . 64
5.3 Supplemental information . . . 73
Chapter VI: Terahertz Sum-Frequency Excitation of Coherent Optical Phonons in the Two-Dimensional Semiconductor WSe_2 . . . 85
6.1 Introduction . . . 85
6.2 Sample preparation and experimental setup . . . 86
6.3 Results and discussion . . . 88
6.4 Conclusion . . . 92
Chapter VII: Conclusion and Future Directions . . . 95
7.1 Summary . . . 95
7.2 Future work . . . 96
Appendix A: Operation procedures for the nonlinear THz spectrometer . . . 100

LIST OF ILLUSTRATIONS

Number *Page*

1.1 The electromegnetic spectrum and the relevant fundamental motions and resonant excitations in gas, liquid, and solid phase systems. . . . 1

1.2 H-bond bending, stretching, and libration modes in the THz region. The THz spectra of water is digitized from [32] and reproduced. . . . 4

1.3 Atomic motion associated with the $A_1(TO_1)$ and $E(TO_1)$ phonon modes of lithium niobate in the hexagonal unit cell [41]. Displacement vectors obtained from *ab initio* calculations by Caciuc et al. [42]. 5

1.4 Mechanism of nonlinear phononics optical control in a two phonon mode model system with quadratic-linear coupling. See main text for explanation. 6

2.1 Terahertz Kerr effect spectroscopy. (a) Nonlinear THz spectroscopy with an anisotropic probe detection scheme. The observables measured experimentally are the phase shifts and probe polarization rotation caused by the photo-induced transient birefringence. (b) Example time domain TKE spectra of liquid bromoform using 800 nm probe pulses. Signals originated from orientation relaxation (exponential decay) and coherent phonon dynamics (oscillatory) are observed. 15

2.2 Types of spectral broadening. (Left) Inhomogeneous broadening caused by an ensemble of vibrational modes, each slightly shifted in frequency due to variations in the local chemical environment. (Right) Homogeneous broadening, where the peak width is related to the natural lifetime of the mode through the uncertainty principle. 17

2.3 Signatures of vibrational coupling in 2D-IR spectra. (Top) A system with two purely harmonic vibrational modes at different frequencies. The 2D-IR spectrum shows no off-diagonal cross peaks. (Bottom) With strong nonlinear coupling between the two modes, clear off-diagonal features will emerge in the 2D-IR spectrum, allowing unambiguous determination. 18

2.4 Pulse sequence and time variables of 2D-TTR spectroscopy. The polarization of each ultrafast pulse is shown in the circles at the top. . 20
2.5 Two example 2D-TTR excitation pathways under the dipole-mediated response function are shown in (a,b) and (c,d), respectively. The pathways are shown in (a,c) the ladder diagram representation and (b,d) the double-sided Feynman diagram representation. (e) The 2D frequency positions of pathway A and B on a 2D-TTR spectra. 21
2.6 Schematic of the home-built 2D-TTR spectrometer. The purple and black dashed boxes show the setup for the conventional stage scan and single-shot methods, respectively. BS: beam-splitter; WGP: wire-grid polarizer; P: polarzier; $\lambda/4$: quarter-wave plate; $\lambda/2$: half-wave plate; S: sample; DL: optical delay line; CAM: camera; PD: photodiode. 26
2.7 Differential chopping scheme for the selective isolation of 2D-TTR signals. Vertical lines indicate when the signals are on. The camera is only employed in the single-shot detection scheme. 27
2.8 Echelon-based single-shot detection scheme. (a) "Time-to-pixel" mapping in the single-shot detection scheme. (b) Horizontal slice of the camera image encodes the time-delay information. The different between the THz pump on and pump off images yield the TKE spectra. 28
2.9 Screenshot of the 2D-TTR GUI during a measurement. Channels A, B, and C corresponds to the demodulated signals at $\frac{1}{2}$, $\frac{1}{3}$, and $\frac{1}{6}$ of the laser repetition rate, respectively. 29
3.1 Experimental layout for the nonlinear imaging technique. F: 20 THz long-pass filter (QMC Instruments); P: polarizers; WGP: wire-grid polarizer; S: sample/100 μm GaP; ND: neutral density filter; LP: 750 nm long-pass filter; L: imaging lens. Green: 1.4 μm pump pulse; Red: 800 nm probe; Blue: THz pump pulse. 36
3.2 Characterization of the THz pulse shape. (a) Time-resolved, EO sampled THz_A pulse shape in air. (b) Corresponding bandwidth of THz_A obtained from Fourier Transform. 38

3.3 The differential chopping scheme. (Left) Time series of each individual nonlinear contribution to the camera response as a function of time. THz-on (purple) and THz-off (blue) frames are represented by 1 and 0 values. The camera trace shows the normalized amplitude of the center pixel in first 10 frames of a typical experimental measurement. (Right) Corresponding Fourier transform of each time series. The modulation frequencies (333 and 500 Hz) and the difference frequency (166 Hz) are highlighted. 39
3.4 Characterization of the THz beam profile with the nonlinear imaging technique. (a) Nonlinear beam profile of 2D-TTR spectroscopy. Grey contours show the best fit 2D Gaussian distribuion. (b) Simulated nonlinear beam profile from the product of experimentally measured E_A^{THz} (red contours) and E_B^{THz} (blue contours) distributions. 42
3.5 THz field strength dependence of the three differentially modulated channels (a) S_A, (b) S_B, and (c) S_{A+B}. 43
4.1 A resonant TTR signal requires dipole nonlinearities to excite a vibrational coherence — a representative process is illustrated in the Res-TKE (resonant terahertz Kerr effect) ladder and Feynman diagrams. In contrast, a sum-frequency excited molecular coherence is produced through interactions linear in the polarizability operator. The virtual state in SF-TKE is short-lived, and therefore the signal is highly dependent upon overlap between the two pump pulses. The familiar optical Kerr effect (SF-OKE) illustrates fundamental similarities with SF-TKE. 49
4.2 Top and bottom rows compare the experimental (Exp) bromoform and chloroform time-domain data to the SF-RDM models. The calculated IRF, whose THz electric fields are used as inputs to the SF-RDM model, is shown for reference (right column). Identical pulse shapes and IRFs are used for both SF-RDM models of bromoform and chloroform. 50
4.3 Top and bottom rows compare the experimental (Exp) bromoform and chloroform frequency-domain data to the SF-RDM model. The calculated IRF is shown for reference with vertical lines indicating where each HMs intramolecular vibrational mode samples the IRF. Note that the experimental and SF-RDM spectra are well matched, and arise from sampling the same IRF at different f_2 frequencies. . . 52

4.4 Comparison of experiment and IRF/RDM model. (a) Slices along f_1 at f_2=eigenmode of the IRF/RDM model and experimental response demonstrate the quality of fit for the bromoform data. Chloroform (b) is reproduced by slicing along the same IRF/SF-RDM model as shown in (a) at f_2=7.8 THz, instead of at bromoform's f_2=4.7 THz. . 53
4.5 Comparison of the experimental and model THz pulse shapes (a,b) and corresponding bandwidths (c,d). See the SI for more detail on the optimization process used to obtain the model pulse shapes. . . . 53
4.6 The optical path of the 2D-TTR single-shot spectrometer. Seen in an inset are the polarizations of the two THz pump and 800 nm probe fields, and the experimental time definitions. 56
4.7 Top and bottom rows compare the experimental (Exp) bromoform time-domain data under two different THz pumping regimes. Slight changes to the emitted THz fields result in different time-domain IRFs. SF-RDM models using the THz electric fields that produce each IRF fully reproduce the experimental data. 58
4.8 Top and bottom rows compare the experimental (Exp) bromoform frequency-domain data under two different THz pumping regimes. Slight changes to the emitted THz fields result in different frequency-domain IRFs. SF-RDM models with the THz electric fields that produce each IRF reproduce the experimental spectra. 59
4.9 Bromoform and chloroform intramolecular vibrational responses are detected in 1D-TKE measurements. The THz bandwidth of the DAST emission as measured in diamond is shown in blue shading. 60
5.1 Experimental details. (a) $LiNbO_3$ crystal structure in the hexagonal unit cell [21, 22]. (b) Schematic of the 2D-TTR experiment, pulse sequence, and time definitions. The polarization of each pulse is indicated in the circles. Coordinates $\{x, y, z\}$ refer to the crystal axes of x-cut $LiNbO_3$, where x and z coincide with unit cell vectors a and c, and y is orthogonal to x and z. (c) Red: PhP dispersion curve for E-symmetry phonon modes [23]. Black: wavevector matching condition of the 800 nm probe for forward (k_+, solid) and backward (k_-, dashed) propagating PhPs [19]. The shaded regions show the THz bandwidth of E_A^{THz} and E_B^{THz}. 66

5.2 Analysis of the 2D-TTR spectra of $LiNbO_3$. (a) 2D-TTR spectra in the frequency domain for four pump-probe polarization configurations, taken from the combination of two crystal orientations and two THz polarization orderings (positive and negative t_1 quadrants). The spectra have been deconvolved by the IRF to reveal true intensity and frequency positions. Guiding lines are provided at $f_1 = 3.85$ THz (violet), $f_1 = 7.1$ THz (teal), $f_2 = \pm 3.25$ THz (violet) and $f_2 = \pm 3.85$ THz (teal). (b) Zoom-in of peaks II to IV for polarization $R^{(3)}_{zyzy}$. (c) Select Feynman pathways for the observed nonlinear peaks (I, I') and III. Depending on the THz polarizations, III (yz) or III (zy) is selectively observed. See SI for full assignment. (d) THz polarization dependence of the FT amplitude of peaks III and IV. (e) THz field strength dependence of the $E(TO_1)$ ($A_{3.85}$) and $E(TO_3)$ ($A_{7.1}$) features along f_1. Best linear fits are shown as dashed lines. 68

5.3 Third-order models based on different excitation mechanisms and sources of anharmonicity. Identical guiding lines are added. For reference, the overlayed contours depict the $R^{(3)}_{zyzy}$ experimental spectra. 69

5.4 Characterization of the THz pulse shapes and instrument response function. (a) Bandwidths of the two THz pump pulses in 2D-TTR. The time domain pulse shapes are shown in the inset. (b) Instrument response function (IRF) of 2D-TTR in 2D frequency space. 74

5.5 Time orderings and polarization configurations of 2D-TTR spectroscopy. (a) Time domain 2D-TTR spectra for two crystal orientations of x-cut $LiNbO_3$. (b) Polarization configurations, crystal orientation, and third-order element measured by each quadrant of the 2D-TTR spectra. Coordinates $\{x, y, z\}$ refer to the crystal axes of x-cut $LiNbO_3$, where x and z coincide with unit cell vectors a and c, and y is orthogonal to x and z. 77

5.6 Complete Feynman pathway analysis for the four 2D features observed. Symmetry-allowed lowest energy pathways are assigned for each THz polarization. Polarization requirements for THz transitions are labelled. 78

5.7 THz field strength dependence of the 2D-TTR signal along t_1 for (a-d) E_A^{THz} and (e-h) E_B^{THz}. The time domain signals are shown in a and e. The corresponding Fourier transforms are shown in b and f. Zoom-in of the 7.1 THz peak is shown in c and g. (d,h) Normalized amplitude at E(TO_1) (3.85 THz) and E(TO_3) (7.1 THz) PhP frequencies are plotted against the varied THz field strength. Best linear fits are provided as dashed lines. 79

5.8 Energy and momentum conservation requirements for the THz transitions in Feynman pathways (a) IV (zy) and (b) IV (yz). Physical parameters of the E-symmetry phonon branches are obtained from Barker et al. [23]. The dispersion of the THz electric field is digitized from experimental measurements by Kojima et al. [20]. 80

5.9 Energy and momentum conservation requirements for a nonlinear transition involving a scattered A_1-symmetry PhP. Physical parameters of the E- and A_1-symmetry phonon branches are obtained from Barker et al. [23]. The dispersion of the THz electric field is digitized from experimental measurements by Kojima et al. (E: [20], A_1: [37]). 81

6.1 TKE spectroscopy of WSe_2. (a) THz pulse shape measured with electro-optic sampling (EOS) on 100 μm GaP. (b) Corresponding THz bandwidth of (a). (c) Schematic of the TKE spectrometer. WGP: wire-grid polarizer; P1, P2: polarizers; S: sample; PD: photodiode; DL: optical delay line; $\lambda/2$: half-wave plate; $\lambda/4$: quarter-wave plate. Inset: Polarization of the THz pump and optical probe pulses relative to the crystal axes of WSe_2. 87

6.2 Free standing sample mount for thin film WSe_2 samples. (left) Photo of the free standing WSe_2 mounted on a 400 μm diameter pinhole. (right) Schematic of the WSe_2 sample assembly. 88

6.3 Crystal structure and phonon modes of WSe_2. (top) Crystal lattice structure of WSe_2. (bottom) Lattice motion of IR- and Raman-active modes of WSe_2. 89

6.4 TKE spectra for WSe_2. (red) TKE time domain signal of WSe_2 thin films. The polarization of the THz pump and optical probe pulses are parallel to the AC direction. (green) Difference trace with the exponential decay component subtracted to isolate the oscillatory signal. (inset) The corresponding FT of the difference signal, which reveals the $\sim$ 7.5 THz E_{2g} phonon peak. 90

6.5 THz field strength dependence of the TKE spectra for WSe_2. (a) TKE signal of WSe_2 at different THz electric field strengths. (b) Corresponding FT spectra of (a). (c) The FT spectra in (b) zoomed in to highlight the phonon peak. Integrated FT amplitude between (d) 1-2 THz and (e) 7-8 THz as a function of THz field strength. . . 91

A.1 Screenshot of the stage-scan control GUI. 100

Chapter 1

INTRODUCTION

1.1 Motivation

Spectroscopy has been an indispensable part of numerous research fields for decades, providing essential characterization capabilities for the physical, chemical, and biological world [1–8]. Fundamentally, spectroscopies exploit the response of a sample upon irradiation, so-called light-matter interactions, to determine properties of the sample. Depending on the energy (or frequency) of the incident photons, distinct resonant and non-resonant light-matter interactions are dominant, leading to spectroscopic techniques that are uniquely sensitive to certain degrees of freedom (DOFs) of a sample. Specifically in chemistry, the primary interests lie in the nuclear and electronic DOFs of molecular and solid state systems [9–11]. A number of important elementary motions in chemistry and their corresponding energy scales with respect to the electromagnetic spectrum are shown in Fig. 1.1, including molecular rotations in the microwave region [12], chemical bond vibrations in the infrared (IR) region [13], and electronic excitations (core and valence) at visible and higher frequencies [14]. Sandwiched in between the microwave and IR regions is the terahertz (THz), or far IR, frequency range (0.1-20 THz, 3-660 cm^{-1}), which is home to long-ranged, delocalized, intermolecular DOFs that strongly influence the chemical

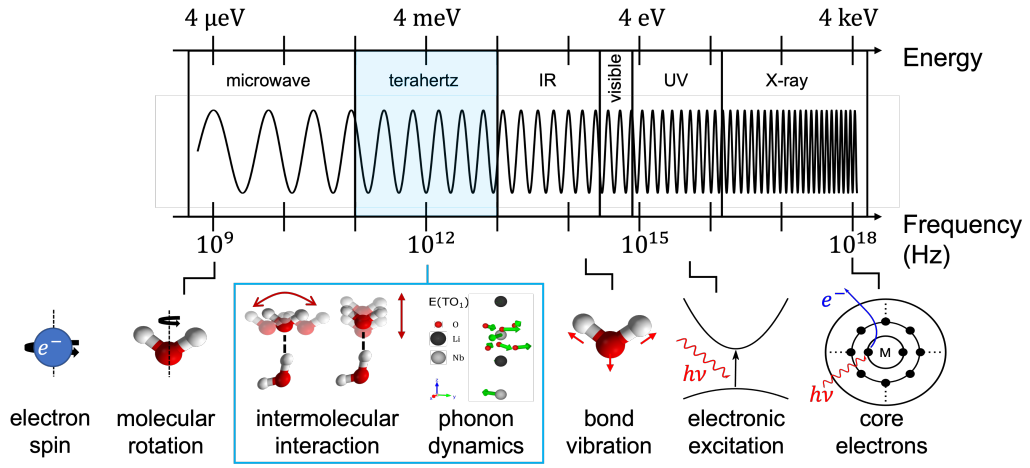

Figure 1.1: The electromegnetic spectrum and the relevant fundamental motions and resonant excitations in gas, liquid, and solid phase systems.

and physical properties of condensed matter at room temperature [15–20]. Due to the fundamental importance of these long-ranged and correlative interactions, THz science has grown rapidly in the past decade following breakthroughs in THz light sources suitable for various THz spectroscopies.

1.2 Overview of chapters

In this thesis, we build on previous expertise of the Blake group in THz spectroscopy to continue exploring elusive correlative interactions in condensed matter. Our goal is to provide clarity on the experimental implementation and spectral interpretation of these novel and often misunderstood spectroscopies. The rest of the introduction section will discuss in detail the nature of the intermolecular DOFs in liquids and crystalline solids. Emphasis will be placed on describing the current challenges and potential applications in understanding these under-explored interactions. A deep dive into the theoretical and experimental considerations of nonlinear ultrafast THz spectroscopy will be presented in Chapter 2, with a focus on third-order THz Kerr effect spectroscopy and our home-built 2D THz-THz-Raman spectroscopic instrument. We will discuss the specific signals that these exotic spectroscopies are sensitive to and the unique scientific questions they are designed to answer. Chapters 3 through 6 presents the development and application of nonlinear THz spectroscopies on real-world samples, including organic liquids and semiconductor materials. A summary of the current work and a brief discussion of future directions will be included in Chapter 7.

1.3 Fundamental motions in the terahertz frequency range

Long-ranged, delocalized, intermolecular interactions in molecular and solid state systems are fascinating, yet elusive, research areas [19, 20]. These features are particularly impactful to the chemical and physical properties of condensed matter at room temperature due to their low barriers and excitation energies. Specifically, the energy required to resonantly excite these interactions are often in the THz regime (few to 10s of meV), which is comparable to the available thermal energy at room temperature estimated by the product of the Boltzmann constant and temperature $k_B \cdot T$ (25 meV or equivalent to the photon energy at 6 THz). As a result, the first excited state of these modes are often readily thermally populated. Further, the collective and delocalized nature of these intermolecular interactions implies that the nuclear motions associated with these modes often leads to significant change in the relative position of atoms and molecules. Thus, these intermolecular interactions

strongly affects the room temperature equilibrium position of atoms and molecules in condensed phase systems, which in turn strongly affects the chemical and physical properties [17, 19, 20].

Liquids

Fundamentally, intermolecular interactions are what distinguishes liquids from gases, where the intermolecular potential energy surface, which governs the attractive and repulsive forces between molecules, dictates the chemical and physical properties of the liquid [21, 22]. Intermolecular interactions in liquids are typically described by the electrostatic pair involved, which also generally implies the strength of the interaction. From strongest to weakest, intermolecular forces include dipole-dipole (Keesom force), dipole-induced-dipole (Debye force), and induced-dipole-induced-dipole (London dispersion) interactions. Of particular interest is the hydrogen bonding (H-bond) interaction, which is an extreme form of dipole-dipole interaction involving a hydrogen atom and an electronegative atom, typically N, O, or F. The H-bond interactions are stronger than typical dipole-dipole interactions and underlie chemical and biological phenomenons such as protein folding and DNA structures [23–25], the unusually fast proton mobility in liquid water [26, 27], and the tetrahedrality of water structures [28]. Due to its fundamental importance in chemistry and biology, hydrogen-bonding has remained a favorite topic of research for the past century. Yet despite decades of investigation, the understanding of H-bonds remains controversial, particularly on the microscopic length-scale and ultrafast time-scale, where the quantum-mechanical nature of the H-bond is dominant [20]. These disagreements have hindered development of accurate water models that are critical to molecular dynamics (MD) simulations of biomolecular processes [29]. The primary challenge for understanding intermolecular interactions in liquid water, including H-bond bending ($\sim$ 2 THz), H-bond stretching ($\sim$ 5 THz), and librational (hindered rotation) modes ($\sim$ 10 – 30 THz), lies in the strong inhomogeneity and overlapping energy, time, and length scales [16, 30, 31]. As shown in Fig. 1.2, the H-bond modes that dictate the dynamics of the water network are significantly broadened in the THz spectra. The extent of the spectral broadening that is caused by inhomogeneity and nonlinear coupling between H-bond modes remains an open question to this day. Experiments in the IR regime have utilized individual OD bond vibrations of dilute HDO in H_2O as reporters of the local H-bond environment to elucidate inhomogeneous lifetimes [33, 34]; while other investigations utilized X-ray scattering spectroscopy to capture instantaneous snapshots of the atomic positions

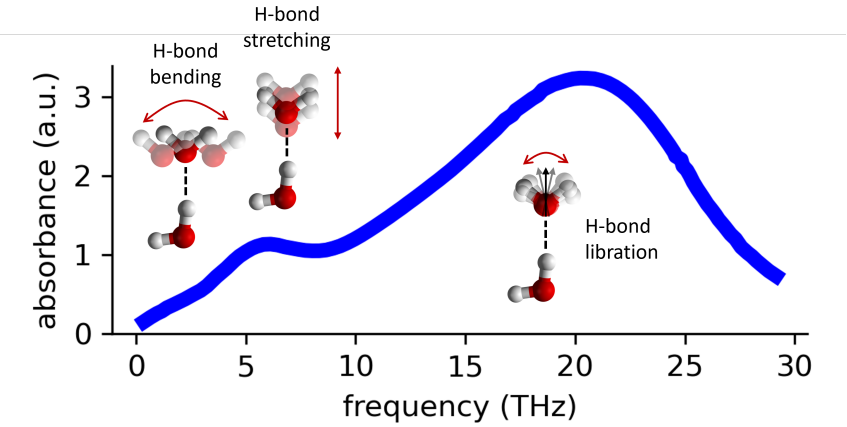

Figure 1.2: H-bond bending, stretching, and libration modes in the THz region. The THz spectra of water is digitized from [32] and reproduced.

in the water H-bond network to unveil microscopic length-scale information [35]. THz spectroscopy provides an unique perspective as it directly and resonantly probes the correlative intermolecular modes in question. Recent works have determined inhomogeneous lifetimes (~100 fs) that appear to be significantly shorter than that determined by the OD reporter (~ 1 ps) [16], implying that THz spectroscopy may provide a complementary *delocalized* picture of the water network as opposed to the *localized* picture non-resonant techniques probe [36]. As THz spectroscopies continue to explore intermolecular interactions in liquids, simulations will be able to refine their force field models to better describe and match the microscopic structural and dynamical measurements obtained using THz spectroscopic techniques.

Crystalline solids

THz research on crystalline solids has gain significant attention due to the diverse quantum phenomena that have energy levels in the THz regime, including phonons [37], magnons [38], polaritons [39], and many more [40]. While key aspects of these quantized particles have been explored with various non-resonant optical spectroscopic techniques, THz science has enabled resonant access to not only probe, but also strongly *drive* excitation of these particles [19, 20]. In this thesis, we will focus on phonons, which are quantized vibrations of the crystalline lattice, as well as phonon-polaritons, which result from the strong coupling of photons and optical phonons of similar energy in a lattice.

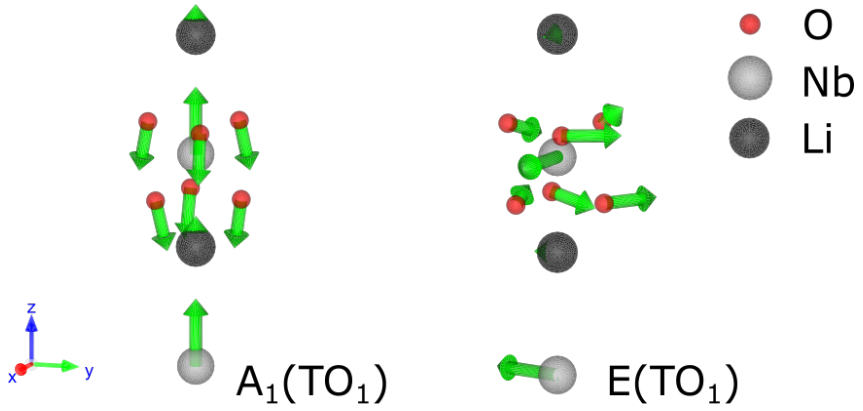

Figure 1.3: Atomic motion associated with the $A_1(TO_1)$ and $E(TO_1)$ phonon modes of lithium niobate in the hexagonal unit cell [41]. Displacement vectors obtained from *ab initio* calculations by Caciuc et al. [42].

Phonons in the THz frequency range are unique due to the delocalized nature of the lattice vibrations that involve the movement of most/all atoms in the unit cell, such as the transverse optical (TO) phonon modes of lithium niobate ($LiNbO_3$) shown in Fig. 1.3. Consequently, strong excitation of THz phonon modes have the potential to transiently distort lattice structures, which in turn affects the bulk properties of the crystal. Research into methods to manipulate material properties through photo-excited phonon modes and other collective modes in the THz regime has been coined *Nonlinear Phononics* [18, 19, 39]. Notable demonstrations of nonlinear phononics span a wide range of important condensed matter subjects, including switching of the ferroelectric polarization of $LiNbO_3$ [43, 44], a photo-induced phase transition of $SrTiO_3$ [45], and enhancing superconductivity in cuprate systems [46], to name a few. Nonlinear phononics utilizes ultrashort femtosecond (fs) light pulses to induce material property changes on the ultrafast time scale, which is orders of magnitude faster compared to material manipulation with electric fields (generally nanoseconds or slower). Additionally, ordered material states with superconductive or ferroelectric properties can be induced under conditions far removed from the thermodynamic transition temperature [44]. Nonlinear phononics, while still in its infancy, present an important addition to the engineering toolbox for material structures, especially in the quantum regime. In contrast to emerging *static* structural engineering methods, such as Moire heterostructures and nanostructure/morphology engineering, nonlinear phononics provide a *dynamical* method, analogous to electric field or strain, to modify microscopic degrees of freedom in materials and introduce designed electronic and magnetic properties [19].

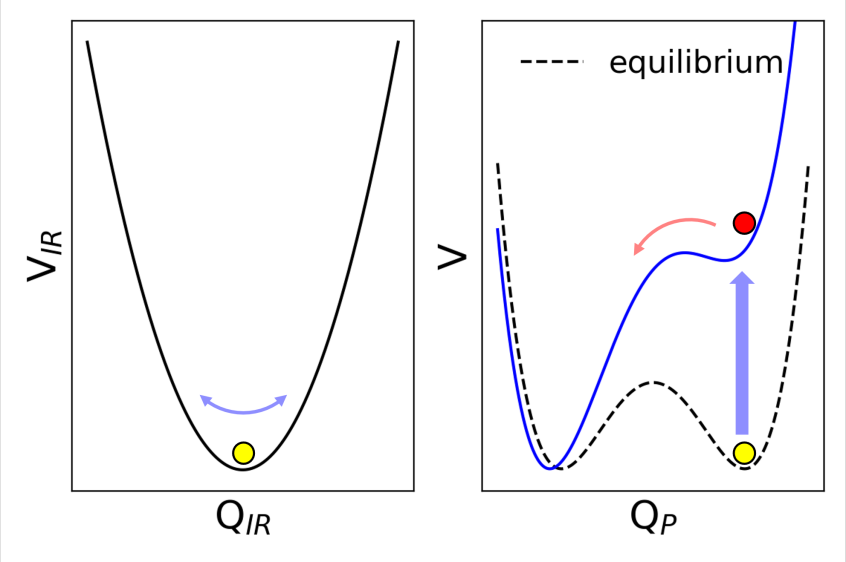

Figure 1.4: Mechanism of nonlinear phononics optical control in a two phonon mode model system with quadratic-linear coupling. See main text for explanation.

These remarkable feats of precise optical control are achieved by large amplitude nonlinear excitations of specific phonon modes, where the anharmonicity of the system rectifies and induces symmetry breaking lattice distortions that alter microscopic interactions and give rise to new material properties and phases [19, 44]. Here, we discuss one particular case of anharmonicity, the quadratic-linear coupling mechanism, to illustrate the optical control scheme in detail. The quadratic-linear coupling mechanism describes a system consisting of two phonon modes (Fig. 1.4): an IR-active phonon, represented by a harmonic potential with coordinate Q_{IR}; and another phonon mode, with a double-well potential that represents two polarizations of a material property along the coordinate Q_P, such as the ferroelectric polarization. Specifically, the two phonon modes are nonlinearly coupled with a quadratic-linear anharmonicity term of the form $Q_{IR}^2 \cdot Q_P$. If we consider direct excitations to the Q_{IR} mode, it causes oscillation along the harmonic well with a net zero average of the Q_{IR} coordinate, resulting in no net displacement of the atomic structure. However, through nonlinear coupling, the phonon mode Q_P experiences a rectified non-zero driving force proportional to Q_{IR}^2, which could distort the double-well potential and cause the current equilibrium position (yellow circle) to no longer be stable (red circle). As a result, spontaneous switching of the material property is achieved upon photo-excitation.

Despite the simplicity of the above model, it nevertheless illustrates the central role of anharmonicity in nonlinear phononic schemes. Specifically, the source of the anharmonicity, the nature of the nonlinear coupling, and the symmetry of the modes involved lead to selection-rules for the allowable structural distortions. For example, in centro-symmetric systems, the $Q_{IR}^2 \cdot Q_P$ term restricts lattice distortions to maintain the point symmetry of the crystal (A_g symmetry) [19]. The possibilities substantially broaden if we consider the general third-order anharmonicity $Q_1^{IR} \cdot Q_2^{IR} \cdot Q_P$ in non-central symmetric crystals, where the term is symmetry-allowed for various combinations of degenerate or distinct phonon modes. In the simple model above, the addition of anharmonicity to the harmonic potential in the form of Q_{IR}^3 would also introduce net non-zero displacement along the Q_{IR} coordinate. It is evident that the form of the anharmonicity and the modes involved in the nonlinear coupling are foundational to understanding and predicting the resulting photo-induced lattice distortions.

The dominant source of anharmonicity in a material system is also crucial to the design of precise optical control schemes for nonlinear phononics [39, 47, 48]. All the anharmonicities described thus far are *mechanical* in nature, meaning that these nonlinear terms reside in the potential energy term ($\hat{V} = \hat{V}_0 + \hat{V}_{anhr}$) of the system Hamiltonian ($\hat{H} = \hat{T} + \hat{V}$). In other words, mechanical anharmonicity describes the anharmonic corrections to the harmonic normal mode picture, in which the phonon modes of a crystal are described by independent harmonic potentials that are not coupled nor interacting with each other. The introduction of higher-order terms account for important nonlinearities in the phonon potential energy surface and couplings between phonon modes.

Another source of anharmonicity, coined *electronic* anharmonicity, describes nonlinear light-matter interactions when the phonon modes are excited by photons. Mathematically, electronic anharmonicity are anharmonic contributions to the electric dipole ($\hat{\mu}$) and/or polarizability ($\hat{\alpha}$) operators that govern the transition probability of IR- and Raman-active modes. Using IR-active transitions as an example, in the harmonic limit, we have the familiar harmonic oscillator selection rule of $\Delta\nu = \pm 1$, where transitions can only occur between adjacent energy levels. This selection rule is relaxed if we consider nonlinear contributions to the dipole operator, $\hat{\mu} = \hat{\mu}_0 + \hat{\mu}_{anhr}$, which leads to non-zero transition probabilities for $\Delta\nu = \pm 2$, $\Delta\nu = \pm 3$, and so on. The fundamental difference between mechanical and electronic anharmonicities is that electronic anharmonicities only affect the excitation process,

whereas mechanical anharmonicities affect both the excitation process and the subsequent relaxation dynamics. In other words, electronic anharmonicities are only in play when photo-induced transitions between different phonon states are concerned, while mechanical anharmonicities remain important after illumination and govern relaxation lifetimes and meta-stability behaviors. Additionally, the mathematical forms and symmetry breaking terms that provide the rectified directional force for lattice distortion are also distinct for the two types of anharmonicities. Thus, characterization of the source and mathematical form of the dominant anharmonicities in the system is crucial to the development of novel nonlinear phononics applications.

References

[1] Calvin Yu et al. "The potential of terahertz imaging for cancer diagnosis: A review of investigations to date." *Quantitative Imaging in Medicine and Surgery* 2.1 (2012), pp. 33–45.

[2] Steffen Wietzke et al. "Terahertz spectroscopy on polymers: A review of morphological studies." *Journal of Molecular Structure* 1006.1-3 (2011), pp. 41–51.

[3] Huib J. Bakker and James L. Skinner. "Vibrational spectroscopy as a probe of structure and dynamics in liquid water." *Chemical Reviews* 110.3 (2010), pp. 1498–1517.

[4] Jérémy R. Rouxel and Shaul Mukamel. "Molecular chirality and its monitoring by ultrafast X-ray pulses." *Chemical Reviews* 122.22 (2022), pp. 16802–16838.

[5] Susanna L. Widicus Weaver. "Millimeterwave and submillimeterwave laboratory spectroscopy in support of observational astronomy." *Annual Review of Astronomy and Astrophysics* 57 (2019), pp. 79–112.

[6] Paola Peluso and Bezhan Chankvetadze. "Recognition in the domain of molecular chirality: from noncovalent interactions to separation of enantiomers." *Chemical Reviews* 122.16 (2022), pp. 13235–13400.

[7] Jonathan Martens et al. "Infrared ion spectroscopy in a modified quadrupole ion trap mass spectrometer at the FELIX free electron laser laboratory." *Review of Scientific Instruments* 87.10 (2016).

[8] Mark A. Blitz and Paul W. Seakins. "Laboratory studies of photochemistry and gas phase radical reaction kinetics relevant to planetary atmospheres." *Chemical Society Reviews* 41.19 (2012), pp. 6318–6347.

[9] Carlos R. Baiz et al. "Vibrational spectroscopic map, vibrational spectroscopy, and intermolecular interaction." *Chemical Reviews* 120.15 (2020), pp. 7152–7218.

[10] Yuan-Pin Chang et al. “Spatially-controlled complex molecules and their applications.” *International Reviews in Physical Chemistry* 34.4 (2015), pp. 557–590.

[11] Yuchao Zhang et al. “Surface-plasmon-driven hot electron photochemistry.” *Chemical Reviews* 118.6 (2018), pp. 2927–2954.

[12] Monika Leibscher, Thomas F. Giesen, and Christiane P. Koch. “Principles of enantio-selective excitation in three-wave mixing spectroscopy of chiral molecules.” *Journal of Chemical Physics* 151.1 (2019).

[13] Peter Hamm and Martin Zanni. *Concepts and Methods of 2D Infrared Spectroscopy*. Cambridge: Cambridge University Press, 2011.

[14] Qiuxiang Meng et al. “Post-processing phase-correction algorithm in two-dimensional electronic spectroscopy.” *Optics Express* 25.6 (2017), p. 6644.

[15] Cecilie Ronne et al. “THz time domain spectroscopy of liquids.” *Terahertz Spectroscopy and Applications II* 3828.September 1999 (1999), p. 266.

[16] Janne Savolainen, Saima Ahmed, and Peter Hamm. “Two-dimensional Raman-terahertz spectroscopy of water.” *Proceedings of the National Academy of Sciences* 110.51 (2013), pp. 20402–20407.

[17] Meredith Henstridge et al. “Nonlocal nonlinear phononics.” *Nature Physics* 18.4 (2022), pp. 457–461.

[18] Michael Först et al. “Nonlinear phononics as an ultrafast route to lattice control.” *Nature Physics* 7.11 (2011), pp. 854–856.

[19] Ankit S. Disa, Tobia F. Nova, and Andrea Cavalleri. “Engineering crystal structures with light.” *Nature Physics* 17.10 (2021), pp. 1087–1092.

[20] Peter Hamm et al. “Perspective: THz-driven nuclear dynamics from solids to molecules.” *Structural Dynamics* 4.6 (2017).

[21] Ju Yeon Jo, Hironobu Ito, and Yoshitaka Tanimura. “Full molecular dynamics simulations of liquid water and carbon tetrachloride for two-dimensional Raman spectroscopy in the frequency domain.” *Chemical Physics* 481 (2016), pp. 245–249.

[22] John J. Karnes and Ilan Benjamin. “Deconstructing the local intermolecular ordering and dynamics of liquid chloroform and bromoform.” *The Journal of Physical Chemistry B* 125.14 (2021), pp. 3629–3637.

[23] Carl Calemana et al. “Atomistic simulation of ion solvation in water explains surface preference of halides.” *Proceedings of the National Academy of Sciences of the United States of America* 108.17 (2011), pp. 6838–6842.

[24] Dongping Zhong, Samir Kumar Pal, and Ahmed H. Zewail. “Biological water: A critique.” *Chemical Physics Letters* 503.1-3 (2011), pp. 1–11.

[25] Marie Claire Bellissent-Funel et al. “Water determines the structure and dynamics of proteins.” *Chemical Reviews* 116.13 (2016), pp. 7673–7697.

[26] Alisée Nguyen et al. “Broadband terahertz radiation from two-color mid- and far-infrared laser filaments in air.” *Physical Review A* 97.6 (2018), pp. 3–7.

[27] Dominik Marx et al. “The nature of the hydrated excess proton in water.” *Nature* 397.6720 (1999), pp. 601–604.

[28] John Russo, Kenji Akahane, and Hajime Tanaka. “Water-like anomalies as a function of tetrahedrality.” *Proceedings of the National Academy of Sciences of the United States of America* 115.15 (2018), E3333–E3341.

[29] Saber Naserifar and William A. Goddard. “Liquid water is a dynamic polydisperse branched polymer.” *Proceedings of the National Academy of Sciences* 8 (2019), p. 201817383.

[30] Klaas-Jan Tielrooij et al. “Anisotropic water reorientation around ions.” *Journal of Physical Chemistry B* 115.43 (2011), pp. 12638–12647.

[31] Keiichiro Shiraga et al. “Reconsideration of the relaxational and vibrational line shapes of liquid water based on ultrabroadband dielectric spectroscopy.” *Physical Chemistry Chemical Physics* 20.41 (2018), pp. 26200–26209.

[32] Hans R. Zelsmann. “Temperature dependence of the optical constants for liquid H2O and D2O in the far IR region.” *Journal of Molecular Structure* 350.2 (1995), pp. 95–114.

[33] Andrei Tokmakoff. “Shining light on the rapidly evolving structure of water.” *Science* 317.5834 (2007), pp. 54–55.

[34] Sean T. Roberts, Krupa Ramasesha, and Andrei Tokmakoff. “Structural rearrangements in water viewed through two-dimensional infrared spectroscopy.” *Accounts of Chemical Research* 42.9 (2009), pp. 1239–1249.

[35] Katrin Amann-Winkel et al. “X-ray and neutron scattering of water.” *Chemical Reviews* 116.13 (2016), pp. 7570–7589.

[36] Peter Hamm and Andrey Shalit. “Perspective: Echoes in 2D-Raman-THz spectroscopy.” *Journal of Chemical Physics* 146.13 (2017).

[37] Sebastian Maehrlein et al. “Terahertz sum-frequency excitation of a Raman-active phonon.” *Physical Review Letters* 119.12 (2017), pp. 1–6.

[38] Dominik M. Juraschek, Derek S. Wang, and Prineha Narang. “Sum-frequency excitation of coherent magnons.” *Physical Review B* 103.9 (2021).

[39] Haw-Wei Lin, Griffin Mead, and Geoffrey A. Blake. “Mapping LiNbO$_3$ phonon-polariton nonlinearities with 2D THz-THz-Raman spectroscopy.” *Physical Review Letters* 129.20 (2022), p. 207401.

[40] Zhiyuan Sun et al. “Collective modes and terahertz near-field response of superconductors.” *Physical Review Research* 2.2 (2020), pp. 1–19.

[41] Koichi Momma and Fujio Izumi. "VESTA 3 for three-dimensional visualization of crystal, volumetric and morphology data." *Journal of Applied Crystallography* 44.6 (2011), pp. 1272–1276.

[42] Vasile Caciuc, Andrei V. Postnikov, and Gunnar Borstel. "Ab initio structure and zone-center phonons in LiNbO 3." *Physical Review B* 61.13 (2000), pp. 8806–8813.

[43] Alaska Subedi. "Proposal for ultrafast switching of ferroelectrics using midinfrared pulses." *Physical Review B - Condensed Matter and Materials Physics* 92.21 (2015), pp. 1–6.

[44] Roman Mankowsky et al. "Ultrafast reversal of the ferroelectric polarization." *Physical Review Letters* 118.19 (2017), pp. 1–5.

[45] Xian Li et al. "Terahertz field–induced ferroelectricity in quantum paraelectric SrTiO3." *Science* 364.6445 (2019), pp. 1079–1082.

[46] Roman Mankowsky et al. "Nonlinear lattice dynamics as a basis for enhanced superconductivity in YBa2Cu3O6.5." *Nature* 516.729 (2014), pp. 71–73.

[47] David Sidler and Peter Hamm. "A Feynman diagram description of the 2D-Raman-THz response of amorphous ice." *Journal of Chemical Physics* 153.4 (2020).

[48] Tomislav Begušić and Geoffrey A. Blake. "Two-dimensional infrared-Raman spectroscopy as a probe of water's tetrahedrality." *Nature Communications* 14.1 (2023).

Chapter 2

FUNDAMENTALS OF NONLINEAR AND MULTIDIMENSIONAL THZ SPECTROSCOPY

The main focus of my thesis work has been the development and demonstration of nonlinear ultrafast THz spectroscopic instruments that are capable of detailed characterization of the low frequency nuclear DOFs, particularly in the field of anharmonic vibrational dynamics in condensed matter. In this section, I will detail the theory behind these nonlinear THz techniques and discuss the unique capabilities of multidimensional THz spectroscopies. The final sections will be dedicated to discussions on 2D-THz-THz-Raman (2D-TTR) spectroscopy, which is the specific type of multidimensional spectroscopy I have worked on during my PhD. I will attempt to provide a comprehensive overview on the theory behind 2D-TTR spectroscopy, the lessons we have learned on the interpretation of 2D spectra, and the experimental realization of the complex spectroscopic instrument.

Theory of nonlinear light-matter interactions

The treatment of nonlinear light-matter interactions summarized here takes heavy influences from the excellent tutorial *Principles of Nonlinear Optical Spectroscopy: A Practical Approach (Mukamel for Dummies)* by Hamm [1] and the book *Nonlinear Optics* by Boyd [2]. The formalism for most spectroscopic theories operate in the semi-classical limit, in which photons are treated classically as oscillating electric fields (with frequency ω and wavevector k) and the sample systems are considered to be quantum-mechanical with discrete states. The key observable in spectroscopy is the macroscopic polarization $P(t)$ of the system, which is induced by the electric field $E(t)$ of the incident photons. In nonlinear optics, the macroscopic polarization is generally expressed as a power series of the electric field strength [2]

$$\begin{aligned} P(t) &= P^{(1)}(t) + P^{(2)}(t) + P^{(3)}(t) + \cdots \\ &= \epsilon_0[\chi^{(1)}E(t) + \chi^{(2)}E(t)^2 + \chi^{(3)}E(t)^3 + \cdots] \end{aligned} \tag{2.1}$$

where ϵ_0 is the vacuum permittivity, $P^{(n)}(t)$ is the n-th order macroscopic polarization, and $\chi^{(n)}$ is the n-th order susceptibility. In general, the susceptibilities are tensor quantities that depend on the frequency and polarization of the incident fields. We also note that in media with inversion symmetry, such as isotropic liq-

uids and centrosymmetric crystals, the even-order susceptibilities vanish. Further more, comprehensive tables have been curated in [2] that list all the non-zero tensor elements of the second- and third-order nonlinear susceptibilities for different symmetry and space groups.

To describe the state-specific quantum mechanical behavior of liquids and solids, we adapt eq. 2.1 with the density matrix formalism under the so-called interaction picture [1]. Here, the density matrix $\rho(t)$ represents a statistical ensemble of the condensed phase system, which is necessary to extend beyond pure quantum states. We consider each electric field interaction as an operator that acts on the density matrix $\rho(t)$ at some time t, which perturbs and evolves the population and coherences of $\rho(t)$. For simplicity, we will first treat only electric dipole interactions, denoted by the operator $\hat{\mu}$. Treatment of hybrid techniques that involve both Raman- and dipole-allowed interactions will be provided later in this chapter. Applying the Liouville von Neumann equation and omitting the derivation, which can be found in several spectroscopic textbooks [1], the n-th order nonlinear macroscopic polarization is given as

$$\begin{aligned} P^{(n)}(t) = &\int_0^\infty dt_n \int_0^\infty dt_{n-1} \cdots \int_0^\infty dt_1 \\ &E(t-t_n)E(t-t_n-t_{n-1})\cdots E(t-t_n-\cdots-t_1)\cdot R^{(n)}(t_n, t_{n-1}, \cdots, t_1) \end{aligned} \tag{2.2}$$

where t_n is the time difference between the n-th and $(n-1)$-th interaction, and $R^{(n)}(t_n, t_{n-1}, \cdots, t_1)$ is the n-th order nonlinear response function, which has the form

$$\begin{aligned} &R^{(n)}(t_n, t_{n-1}, \cdots, t_1) = \\ &(-\frac{i}{\hbar})^n \langle \hat{\mu}(t_n + t_{n-1} + \cdots + t_1)[\hat{\mu}(t_{n-1} + \cdots + t_1), \cdots [\hat{\mu}(0), \rho(-\infty)] \cdots] \rangle \end{aligned} \tag{2.3}$$

where $\rho(-\infty)$ is the equilibrium density matrix, $[\cdots, \cdots]$ is the commutator, and $\langle \cdots \rangle$ is the expectation value. In essence, the response function describes the temporal evolution of the density matrix after the series of quantum operators are applied. It is the quantity that all spectroscopies aim to characterize as it contains the quantum mechanical insights into a given system, including the energies, dynamics, and anharmonicities of the various quantum states. We note that there are $n+1$ dipole operators for the n-th order response function, where the first n interactions describe the field interactions that produce the non-equilibrium density matrix and the final interaction accounts for the *detection* of the resulting perturbations as an

emitted electric field. An important limitation is that the final field interaction needs to transition the density matrix into a population state that does not involve off-diagonal elements [1].

Most spectroscopies induce a series of light-matter interactions and measure the emitted electric field, which is directly produced by the induced macroscopic polarization $P^{(n)}$. This is also true for absorption spectroscopies, where the emitted electric field is out-of-phase and destructively interferes with the incident light field. As shown in equation 2.2, the nonlinear macroscopic polarization is the convolution of the product of the incident electric fields and the nonlinear response function $R^{(n)}$. We can therefore rewrite equation 2.2 as

$$P^{(n)}(t) = IRF(t, t_n, t_{n-1}, \cdots, t_1) \circledast R^{(n)}(t_n, t_{n-1}, \cdots, t_1) \tag{2.4}$$

where the product of the electric fields is denoted as the *instrument response function* (IRF) [3, 4], which is only dependent on the experimental setup and not the nature of the sample. The formulation in equation 2.4 is powerful because it separates the experimental signals into two distinct components: the IRF, which is sample independent and can be characterized for a given experimental setup; and the nonlinear response function $R^{(n)}$, which contains insights about the quantum-mechanical states of the sample and can be compared directly to theory and simulations.

Nonlinear one-dimensional (1D) THz spectroscopy

One of the primary techniques employed in this thesis is ultrafast nonlinear 1D THz spectroscopy with an anisotropic probe setup [5–7]. The basic pulse sequence is shown in Fig. 2.1a, in which an intense THz pump pulse is used to induce a transient birefringence in the sample that is detected by a time-delayed weak probe pulse in the form of phase shifts and polarization rotations. It is an extremely sensitive technique due to the high extinction ratio and near zero background from the cross-polarized anisotropic probe detection scheme. To resolve the condensed phase nuclear dynamics that we are interested in across the THz frequency range, which generally have lifetimes of 100s of femtosecond (fs) to several picoseconds (ps), ultrafast pulses with a duration of 30-40 fs are employed. The dynamics are experimentally measured by varying the time-delay between the pump and probe pulse with time steps of few fs, which trace out the temporal evolution of the transient birefringence. As such, ultrafast THz spectroscopy measures signals in the *time domain* in a phase sensitive manner, allowing direct observation of coherent dynamics in various samples. The name "1D" refers to the single time variable

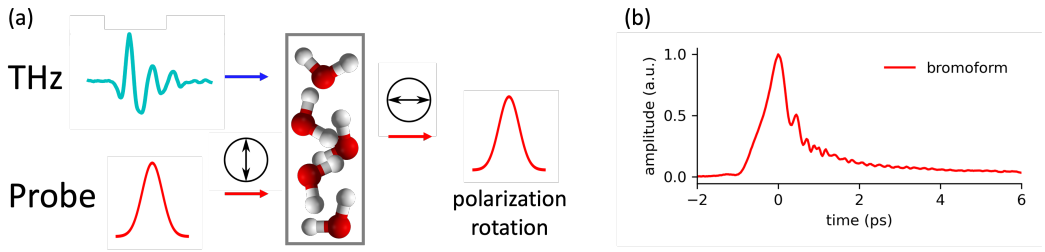

Figure 2.1: Terahertz Kerr effect spectroscopy. (a) Nonlinear THz spectroscopy with an anisotropic probe detection scheme. The observables measured experimentally are the phase shifts and probe polarization rotation caused by the photo-induced transient birefringence. (b) Example time domain TKE spectra of liquid bromoform using 800 nm probe pulses. Signals originated from orientation relaxation (exponential decay) and coherent phonon dynamics (oscillatory) are observed.

scanned in the experiment, in contrast to *multidimensional* techniques described in the next section that employ multiple pulses with more than one time variable.

The photo-induced transient birefringence in nonlinear THz spectroscopy can originate from a number of excited dynamics in the sample, depending on the frequency content and field strength of the THz pulse as well as the nature of the sample [8, 9]. For liquid systems, even-order nonlinear light-matter interactions vanish due to inversion symmetry. Thus, the lowest order nonlinear interaction is third-order, and higher order effects are generally neglected due to the limited field strength of ultrafast THz pulses. In literature, third-order THz spectroscopy is often call THz Kerr effect (TKE) spectroscopy [7] due to similarities to optical Kerr effect spectroscopy that employs optical pump pulses throughout.

The primary nuclear responses in liquids originate from orientational and vibrational dynamics, which govern the relaxation processes in liquids upon THz excitation [6, 9, 10]. A key feature of experimentally generated ultrafast THz pulses is that they are single or few-cycle pulses whose electric field has a non-zero average in time. This is in stark contrast to fs optical pulses that enclose hundreds of cycles within a pulse envelope, such that the average electric field is considered to be zero over the entire pulse. The net THz electric field acts on the rotational DOFs to preferentially align the molecules along the direction of the THz polarization, thus inducing an anisotropic angular distribution from an initially isotropic liquid [9]. The relaxation process is directly related to macroscopic viscosity, microscopic correlation functions, and additional contributions from *bath modes* of the liquid system. The orientational response is generally well-modelled by bi-exponential

decays with unique features added for specific bath modes for the liquid system, such as contributions from librational motions.

For vibrational dynamics, there are two primary processes to consider [3, 6], namely, the polarizability-mediated (Raman) process

$$\langle \hat{\alpha}(t)[\hat{\alpha}(0), \rho(-\infty)]\rangle \tag{2.5}$$

and the electric dipole-mediated (resonant) process

$$\langle \hat{\alpha}(t)[\hat{\mu}(0), [\hat{\mu}(0), \rho(-\infty)]]\rangle. \tag{2.6}$$

The final polarizability operator $\hat{\alpha}(t)$ describes the anisotropic probe detection process, which is analogous to a depolarized Raman scattering process. The dominant excitation pathway for a vibrational mode depends on the symmetry, frequency, and anharmonicity of the mode as well as the pulse shape of the THz pulse employed. Vibrational dynamics typically result in damped oscillatory signals in the time domain TKE spectrum, whose oscillation frequency and damping constant provide insight into the energy and lifetime of THz vibrational modes [5, 6]. A typical time domain TKE spectrum of liquid bromoform is provided in Fig. 2.1b, where both orientational (exponential decay) and vibrational (coherent oscillations) responses are observed.

In solid state systems, third-order signals from phonon or phonon-polariton systems can be described identically with the Raman and resonant processes. However, many crystals do not possess inversion symmetry and have strong second-order effects. Due to the final $\hat{\alpha(t)}$ operator, the only possible excitation mechanism is dipole-mediated and of the form

$$\langle \hat{\alpha}(t)[\hat{\mu}(0), \rho(-\infty)]\rangle. \tag{2.7}$$

While relatively simple to perform, 1D THz spectroscopy lacks the spectral resolution necessary to unambiguously determine excitation mechanisms of driven dynamics and important chemical and physical properties of the system [11]. Despite having different field strength dependencies, it is often experimentally challenging to isolate and analyze second- and third-order processes in solids when multiple phonon modes are excited simultaneously [12, 13]. In addition, the Raman- and dipole-mediated third-order pathways are difficult to distinguish in 1D THz spectroscopy, especially when nonlinear coupling between multiple phonon modes is involved due to anharmonicity. In simple cases where the coherent phonon dynamics involve a single phonon mode, such as the case of WSe_2 presented in Chapter

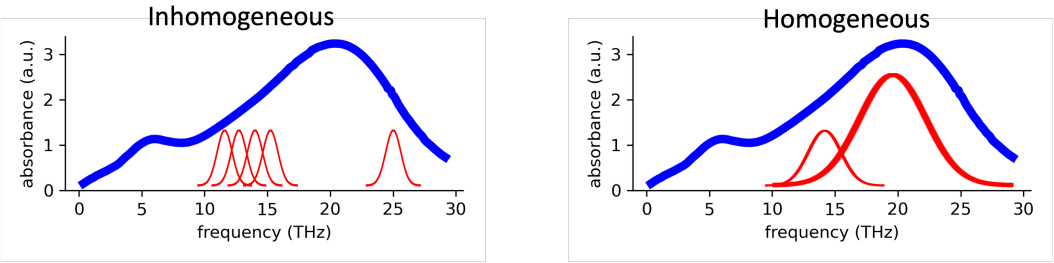

Figure 2.2: Types of spectral broadening. (Left) Inhomogeneous broadening caused by an ensemble of vibrational modes, each slightly shifted in frequency due to variations in the local chemical environment. (Right) Homogeneous broadening, where the peak width is related to the natural lifetime of the mode through the uncertainty principle.

6 of the thesis, one can eliminate other possible mechanisms through symmetry and energy arguments to determine the excitation pathway. However, in complex cases of phonon coupling, signals from different phonon modes that are excited through multiple pathways often overlap in the time domain, making it challenging to isolate and analyze them individually. Further, the limited spectral resolution of 1D spectroscopy also makes it difficult to distinguish the dominant source of anharmonicity and spectral broadening. The former hinders the development of nonlinear phononics methods, which rely on precise understanding of the mathematical form and source of the underlying anharmonicity. The latter refers to two important mechanisms, namely homogeneous and inhomogeneous broadening, that contribute to the spectral width of a peak in the frequency domain [11]. A classic example is the spectrum of liquid water in the THz regime, as shown in Fig. 2.2, which is incredibly broad and nearly featureless. Homogeneous broadening refers to the natural linewidth due to the lifetime of a given mode (shorter lifetimes yield broader peaks); whereas inhomogeneous broadening refers to broadening caused by an ensemble of vibrational modes that are shifted in oscillation frequency due to heterogeneity in the local chemical environment. Both mechanisms could be fit to the 1D THz spectrum of water, but represent two distinct chemical interpretations of the nature of the liquid water environment. Successful characterization of the chemical environment of water will be a major step forward in assisting the development of accurate water models for molecular dynamics simulations [14].

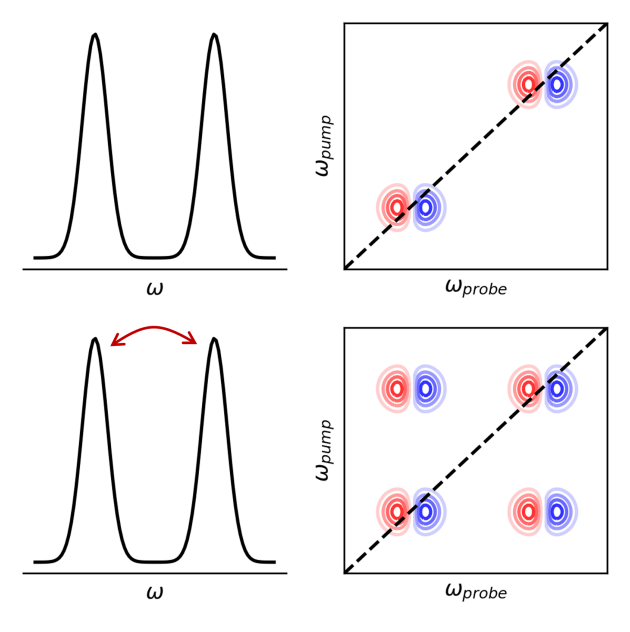

Figure 2.3: Signatures of vibrational coupling in 2D-IR spectra. (Top) A system with two purely harmonic vibrational modes at different frequencies. The 2D-IR spectrum shows no off-diagonal cross peaks. (Bottom) With strong nonlinear coupling between the two modes, clear off-diagonal features will emerge in the 2D-IR spectrum, allowing unambiguous determination.

Multidimensional THz spectroscopy

Multidimensional spectroscopies employ multiple time-delayed pulses to resolve spectral features from dynamical processes that are ambiguous in 1D spectroscopies, including spectral broadening, anharmonicities, and excitation mechanisms [11, 15, 16]. Each time variable in the multi-time pulse sequence corresponds to a time axis in the measured time domain spectrum or, equivalently, a frequency axis in the Fourier transformed frequency domain spectrum. In effect, multidimensional spectroscopy improves spectra resolution and reduces spectral congestion by spreading spectral information onto additional axes. Further, the additional axes allow correlations between features at different frequencies to be analyzed and assigned to unique response functions that reveal the precise temporal evolution of the density matrix after every light-matter interaction. While higher-dimensional spectroscopies have been demonstrated [17], two-dimensional (2D) spectroscopies are the most common due to the exponential time scaling with respect to the number of time axes. A well-established example is 2D-IR spectroscopy [11, 18, 19], where cross peak features emerge when there are correlations or energy exchanges between two vibrational modes, as shown in Fig. 2.3. We note that the projection of the 2D spectrum onto a

single frequency axis generally recovers the 1D spectrum.

The particular flavor of 2D spectroscopy I have worked on in my PhD is coined "2D THz-THz-Raman" (2D-TTR) spectroscopy [3, 20, 21], which is an extension of the TKE spectroscopy described above. The name reflects the pulse sequence employed, as shown in Fig. 2.4, which involves two orthogonally-polarized THz pump pulses and an anisotropic Raman probe pulse that are separated by time variables t_1 and t_2. It belongs to the family of hybrid 2D spectroscopies where pulses of different color (frequency) are employed to probe distinct DOFs of the system [4, 14, 20, 22, 23]. Hybrid 2D THz spectroscopies emerged due to technical challenges for 2D-THz and 2D-Raman spectroscopies, which were both initially proposed by theorists to investigate low frequency dynamics and anharmonicities in liquids [24–28]. Specifically, due to the low conversion efficiency of ultrafast THz pulse generation, pure 2D-THz spectroscopy–that is analogous to 2D-IR spectroscopy–has been limited to solid samples with large nonlinear susceptibilities, until very recently [29, 30]. On the other hand, fifth-order 2D-Raman spectroscopies are hindered by competing third-order cascade signatures that require complex wavevector matching schemes to reject [31–33]. Hybrid 2D THz techniques are able to significantly boost signal strength by replacing one or more THz pulses with more efficient light sources in the near IR or visible frequency ranges. One example of hybrid 2D THz techniques is the 2D Raman-THz spectroscopic family, which replaces two Raman interactions in 2D-Raman spectroscopy with THz interactions, resulting in three time orderings: 2D-TTR (this work), 2D-TRT and 2D-RTT [4, 34]. All three spectroscopies have now been realized experimentally and applied to water [4], aqueous salt solutions [34], organic liquids [3], and semiconductor solids [21].

The response functions of 2D Raman-THz spectroscopies have been analyzed in detail by Hamm and coworkers for the case of a single vibrational mode [35] and that of two nonlinearly coupled modes [36]. An important difference between the hybrid 2D Raman-THz techniques and "conventional" 2D-IR (and 2D-THz) techniques is the number of field interactions involved, where the former employs three pulses (2-in-1-out) and the latter employs four pulses (3-in-1-out). As noted in the theory section, the final field interaction must result in a population state, which indicates that hybrid Raman-THz techniques must involve a zero- or two-quanta *nonlinear* transition, whereas 2D-IR techniques involve only *linear* one-quanta transitions. While higher-quanta transitions may be possible, a pathway involving two one-quanta and a single zero- or two-quanta transition is the lowest order nonlinear

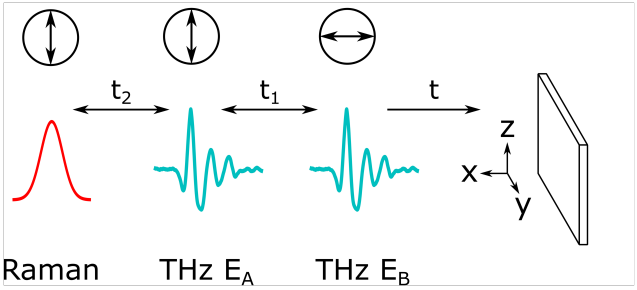

Figure 2.4: Pulse sequence and time variables of 2D-TTR spectroscopy. The polarization of each ultrafast pulse is shown in the circles at the top.

pathway and would likely be dominant in signal strength. Because the zero- and two-quanta transitions are forbidden in the harmonic limit, hybrid Raman-THz spectra are significantly more complex than 2D-IR spectra and uniquely sensitive to the anharmonicities and nonlinear couplings of the excited vibrational modes. The "resonant" response function of 2D-TTR spectroscopy is given as

$$S^{Res}_{TTR}(t_1, t_2) \propto \langle \hat{\alpha}(t_1 + t_2)[\hat{\mu}(t_1), [\hat{\mu}(0), \rho(-\infty)]]\rangle \tag{2.8}$$

which is determined from the time ordering of the THz (dipole) and Raman (polarizability) interactions of the 2D-TTR pulse sequence. We note that the nonlinear interaction may occur due to electronic anharmonicity in the $\hat{\mu}$ and $\hat{\alpha}$ operators or mechanical anharmonicity in the system Hamiltonian, which leads to distinct sets of possible pathways. Compared to TKE spectroscopy, where both $\hat{\mu}$ interactions occur at time $t = 0$, 2D-TTR spectroscopy separates the two interactions by the experimentally controlled time variable t_1. By scanning t_1 and t_2 on a 2D grid, the coherent dynamics are measured along each axis, which reveal the quantum state the system is in after each field interaction. A 2D Fourier transform on the 2D time domain spectra further analyzes the correlations between different frequency components, which correspond to different quantum states. As a result, the 2D frequency position of a given peak directly reveals the time evolution of the density matrix for an excitation pathway.

To illustrate the relation between an excitation pathway and the 2D-TTR response, we provide two example pathways, given two coupled vibrational modes A and B with frequencies ω_A and ω_B, respectively. Pathway A involves a one-quanta excitation of mode A in the first THz interaction, followed by a two-quanta nonlinear coherence transfer from mode A to mode B, and ending with a one-quanta Raman scattering interaction on mode B. The ladder diagram representation for this pathway is shown

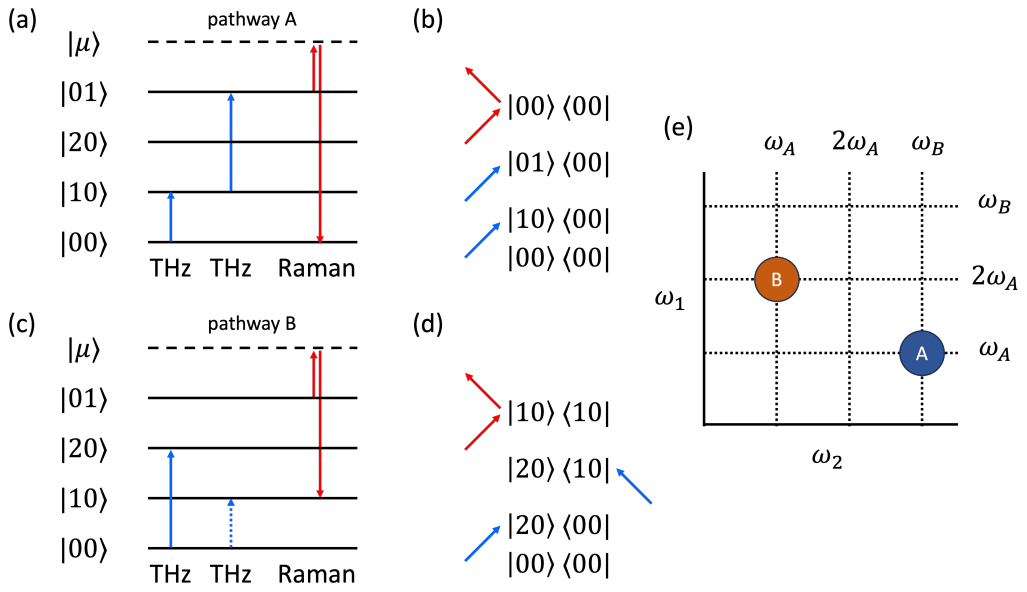

Figure 2.5: Two example 2D-TTR excitation pathways under the dipole-mediated response function are shown in (a,b) and (c,d), respectively. The pathways are shown in (a,c) the ladder diagram representation and (b,d) the double-sided Feynman diagram representation. (e) The 2D frequency positions of pathway A and B on a 2D-TTR spectra.

in Fig. 2.5a, where interactions with light are represented by blue (THz) and red (Raman) arrows. Ket and bra side field interactions are typically represented with solid and dotted arrows, respectively. The quantum states are denoted using $|n_A n_B\rangle$ with quantum numbers n_A and n_B for modes A and B, respectively, and the state $|\mu\rangle$ denotes the virtual state for the Raman interaction. The preferred notation within the 2D spectroscopy is the doubled-sided Feynman diagram notation [11], as shown in Fig. 2.5b for the same pathway. In this notation, the arrows again represent field interactions, with inward and outward arrows corresponding to excitation and de-excitation processes, respectively. The quantum states are written in full with both the bra and ket sides, making it convenient to denote bra and ket side interactions (instead of solid and dotted arrows). 2D-TTR pathways may also involve anharmonic interactions in a single phonon mode, as demonstrated by pathway B shown in Fig. 2.5c and d. Here, a ket side two-quanta excitation of mode A brings the system to the coherence state $|20\rangle\langle 00|$. It is followed by a bra side one-quanta excitation of the same mode, resulting in the coherence state $|20\rangle\langle 10|$. The final Raman interaction acts on the ket side to transition the system back to the population state $|10\rangle\langle 10|$, thus completing the Feynman pathway.

The 2D frequency position of each pathway is precisely determined by the coherence state the system is in after every field interaction. Specifically, excitation into a coherence state generates an off-diagonal element of the density matrix that oscillates and relaxes due to dephasing. The oscillation frequency is determined by the energy difference between the bra and ket quantum states that are in coherence. This oscillatory signal, sometimes called a free-induction decay, can be detected in phase-sensitive spectroscopic techniques, including 2D-TTR spectroscopy. Using pathway B as an example, the system is in the coherence state $|20\rangle\langle 00|$ after the first THz interaction, indicating that an oscillatory signal would be observed along t_1 with a frequency of $2\omega_A$. After the second THz interaction, the system is in the coherence state $|20\rangle\langle 10|$, which correspond to an oscillatory signal along t_2 with frequency ω_A. Thus, pathway B corresponds to a 2D peak in the 2D-TTR spectra at $(\omega_1, \omega_2) = (2\omega_A, \omega_A)$, as shown in Fig. 2.5e. We note that all other pathways that generate a 2D peak at $(\omega_1, \omega_2) = (2\omega_A, \omega_A)$ have field interactions with identical quantum number changes and only differ in the starting population state. In general, the Feynman pathway presented in Fig. 2.5d would be the dominant contributor to the $(2\omega_A, \omega_A)$ peak because the ground state $|00\rangle\langle 00|$ is more populated than the first excited population state $|10\rangle\langle 10|$ and any higher excited states. We note that in certain crystalline solids, symmetry selection rules may forbid a pathway that starts from the ground state, making the lowest energy symmetry-allowed pathway most dominant.

The ultimate goal of 2D-TTR spectroscopy is to provide insight into the underlying nonlinear coupling interactions and dominant source of anharmonicities in condensed matter systems. Electronic and mechanical anharmonicities lead to distinct scenarios in the design of tailored pulses for material manipulation [14, 21, 36, 37], yet distinguishing between the two cases is no easy task. Typically, these properties are only accessible through careful quantum chemical calculations of the material, such as Density Functional Theory (DFT) [21], which can be theoretically and computationally challenging for complex quantum materials or H-bonded liquids. In general, the two types of anharmonicities produce similar spectral features. Specifically, the commonly observed vibrational overtones, difference frequency peaks, and higher order features in Raman and IR spectroscopies can be due to both mechanical and electronic anharmonicities. Extracting these important molecular and material insights therefore require a careful analysis of 2D spectra. As demonstrated above, 2D-TTR spectroscopy directly reveals the linear and nonlinear transitions induced by each field interaction. In particular, Feynman pathway

analysis may reveal nonlinear coupling interactions, such as coherence transfers between two vibrational normal modes, i.e., the $|10\rangle \rightarrow |01\rangle$ transition in pathway A. Further, the set of nonlinear transitions that are symmetry-allowed is strongly dependent on the source of the anharmonicity. A detailed derivation is provided by Sidler et al. [36], where electronic and mechanical anharmonicities lead to distinct sets of 2D frequency peaks with different relative intensities. As a result, a simple calculation yields the expected 2D-TTR spectra from each source of anharmonicity, which can be compared directly with the experimentally measured 2D-TTR spectra to determine the dominant source of anharmonicity.

In addition to the dipole-mediated "resonant" 2D-TTR response function, our work in 2020 [3] has identified a novel polarizability-mediated sum-frequency (SF) THz excitation pathway in 2D-TTR spectroscopy with a response function that is identical to TKE spectroscopy, namely,

$$S_{TTR}^{SF}(t_1, t_2) \propto \langle \hat{\alpha}(t_1 + t_2)[\hat{\alpha}(0), \rho(-\infty)]. \rangle \tag{2.9}$$

The SF THz pathway is purely linear in polarizability, where each $\hat{\alpha}$ interaction induces an one-quanta transition of a Raman-active vibrational mode. THz SF excitation is induced via a two-photon process, in which the combined energy of the two photons matches the mode energy. Further, only one time variable separates the two operators, namely, $t = t_1 + t_2$, indicating that it is effectively an "1D" spectroscopic response. Consequently, it is challenging to determine anharmonicity and nonlinear coupling information from the SF THz excitation pathway.

The resonant and SF THz excitation pathways are competing pathways in nonlinear THz spectroscopy owing to the unique properties of ultrafast THz pulses, where the bandwidth of the THz pulse is comparable to the center frequency of the THz pulse. The bandwidth of an ultrafast pulse is fundamentally governed by the Heisenberg uncertainty principle,

$$\Delta\omega \cdot \Delta t \geq \frac{\hbar}{2} \tag{2.10}$$

where $\Delta\omega$ is the pulse bandwidth, Δt is the pulse duration, and $\hbar$ is the reduced Planck's constant. In the context of ultrafast laser pulses, the time-bandwidth product (TBP) is more widely used, which is a rearrangement of the uncertainty principle with convenient experimental observables,

$$TBP = \Delta\nu \cdot \Delta\tau \tag{2.11}$$

where $\Delta\nu$ is the spectral width (full-width-at-half-max, FWHM) in units of hertz (Hz) and $\Delta\tau$ is the pulse duration (FWHM) in units of seconds (s). The minimum value for TBP is dependent on the pulse shape, where Gaussian pulse envelopes require $TBP \geq \frac{2\log 2}{\pi} \approx 0.441$ (pulses with minimum possible TBP are called transform-limited pulses). Therefore, for an ultrafast THz pulse with a duration of ~ 150 fs, the minimum bandwidth of the THz pulse is ~ 3 THz, which is comparable to the center frequency of the THz pulse. Further, THz pulses are generally far from transform-limited, resulting in significantly broader THz bandwidths in practice. For example, THz pulses generated from organic emitter crystals typically have a bandwidth of ~ 10 THz with a center frequency of ~ 4 THz. The experimental consequences of the unique $\Delta\omega \approx \omega$ property of ultrafast THz pulses are two-fold. First, for any sensible frequency of interest at ω, there is always substantial power at $\omega/2$. Thus, experiments that employ ultrafast THz pulses to drive coherent excitations must always consider both the resonant (one-photon) and SF (two-photon) THz excitation pathways. This is in stark contrast to 2D-IR and 2D electronic spectroscopies (2D-ES), where ultrafast IR and visible pulses have spectral widths of 10s of THz and center frequencies of several 100s of THz ($\Delta\omega \ll \omega$). As a result, 2D-IR and 2D-ES techniques may tailor the frequency of their ultrafast pulses to selectively induce one of the excitation pathways. Secondly, the broad frequency content of ultrafast THz pulses relative to their center frequency makes it challenging to implement wavevector matching techniques, such as the BoxCARS geometry, which is commonly used in 2D-IR and 2D-ES spectroscopies to spatially isolate photons from distinct nonlinear pathways. Instead, the colinear phase matching geometry is employed in most THz spectroscopies, where photons from the input beams and all possible light-matter interactions remain colinear after the sample. Thus, a crucial aspect of the experimental design of nonlinear THz spectroscopies is the selective isolation of the desired weak nonlinear signal and the rejection of more intense background photons. For instance, 2D-TTR spectroscopy achieves sensitive, selective, and background-free detection of the third-order nonlinear signals by utilizing a cross-polarized probe detection scheme, which rejects background probe photons with an extinction ratios of over 100,000, and a differential-chopping scheme with lock-in detection, which isolates the third-order 2D nonlinear signal.

Our discovery highlights the importance to understand competing sources of signals in 2D-TTR spectroscopy in order to avoid inaccurate spectral interpretation and inference. A key difference between the resonant and the polarizability response functions lie in the temporal extent of each signal. Specifically, both THz pump

pulses need to interact with the sample at the same time in the polarizability response function, indicating that the THz SF pathway can only exist in the temporal overlap region along the t_1 axes, which is roughly equivalent to the pulse duration of the THz pulses (0.4-0.6 ps). In contrast, the t_1 extent of the resonant response function is dependent on the spectral width of the excited vibrational mode, which is directly related to the relaxation lifetime (typically few ps) and inhomogeneity of the mode.

Chapters 4 to 6 include our published works on the application of nonlinear 1D and 2D THz spectroscopies to various condensed matter systems. Chapters 4 and 5 present the application of 2D-TTR spectroscopy to a liquid system (halogenated methanes) and a semiconductor solid (lithium niobate), respectively. Specifically, these works demonstrate considerations of the IRF in equation 2.4, determination of the dominant response function, and subsequent interpretation of the 2D frequency spectra to extract insights into nonlinear couplings and source of anharmonicities. Chapter 6 demonstrate the investigation of driven phonon dynamics for WSe_2, an emerging layered semiconductor material, using nonlinear 1D THz spectroscopies.

Experimental design of a versatile nonlinear 1D and 2D THz spectrometer

Here, we provide a detailed description of the home-built nonlinear THz spectrometer in the Blake group to highlight the different capabilities of the instrument. Please see Appendix I for a practical guide on the daily operation of the instrument and use of various control programs.

The layout of the full home-built 2D-TTR spectrometer is shown in Fig. 2.6. A Legend Elite-USP regenerative amplifier (Coherent) seeded by a Micra oscillator (Coherent) provides the 800 nm, 40 fs ultrafast light source for the spectrometer. 85% of the amplifier output is used to seed a TOPAS-C optical parametric amplifier (OPA) to produce 1.4 μm, 0.5 mJ pulses, which is split equally to pump two DSTMS (4-N,N-dimethylamino-4'-N'-methyl-stilbazolium 2,4,6-trimethylbenzenesulfonate) crystals (Swiss Terahertz) to produce broadband ultrafast THz pulses that extend up to $\sim$ 10 THz [38, 39]. A number of THz mesh filters (QMC Instruments) are introduced in the THz beam path to block residual 1.4 μm light, which eliminate contamination of nonlinear signals from residual mid-IR light. A half-wave plate ($\lambda/2$) is introduced to one of the two THz pump lines prior to the DSTMS crystal to rotate the polarization of the THz pulse. The two THz pulses are orthogonally-polarized so that they can be recombined with a high-efficiency THz wire-grid polarizer (WGP). To achieve the intense THz field strengths necessary for nonlinear 1D and 2D THz

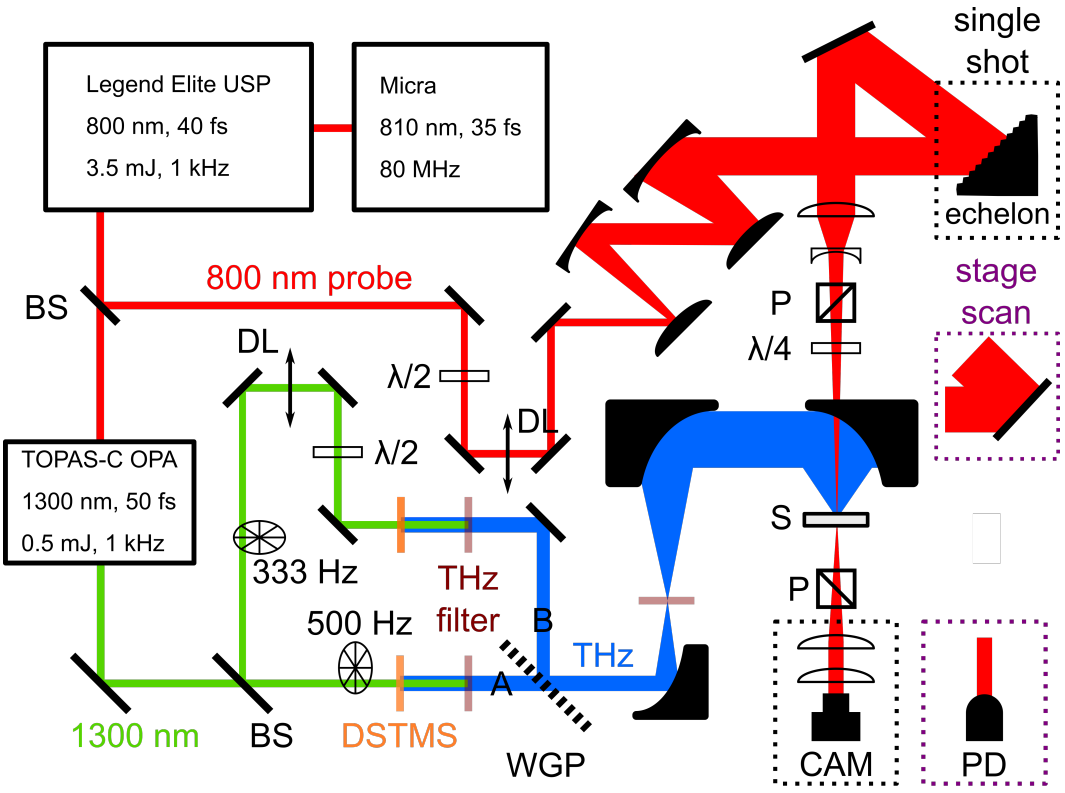

Figure 2.6: Schematic of the home-built 2D-TTR spectrometer. The purple and black dashed boxes show the setup for the conventional stage scan and single-shot methods, respectively. BS: beam-splitter; WGP: wire-grid polarizer; P: polarzier; $\lambda/4$: quarter-wave plate; $\lambda/2$: half-wave plate; S: sample; DL: optical delay line; CAM: camera; PD: photodiode.

spectroscopy (typically $>$ 500 kV/cm), an off-axis parabolic (OAP) mirror relay is used to expand and refocus the THz beam down to near diffraction-limited spot sizes. The two THz pump pulses are modulated using optical choppers to allow lock-in detection of the small nonlinear signals in both TKE and 2D-TTR experiments.

The remaining 15% of the Legend output is used as the probe beam. An iris is inserted to reduce the beam diameter to $\sim$ 2 mm. The beam then reflects off a pair of negative group-velocity dispersion (GVD) mirrors a total of 7 times to compensate for the positive GVD introduced by the series of lenses and polarization optics downstream, ensuring that the probe pulse duration remains $\sim$ 40 fs when it interacts with the sample. The path length of the probe line is controlled by a retro-reflector mounted on an optical delay stage. Our nonlinear THz spectrometer supports two distinct detection methods, namely, the conventional stage-scan and

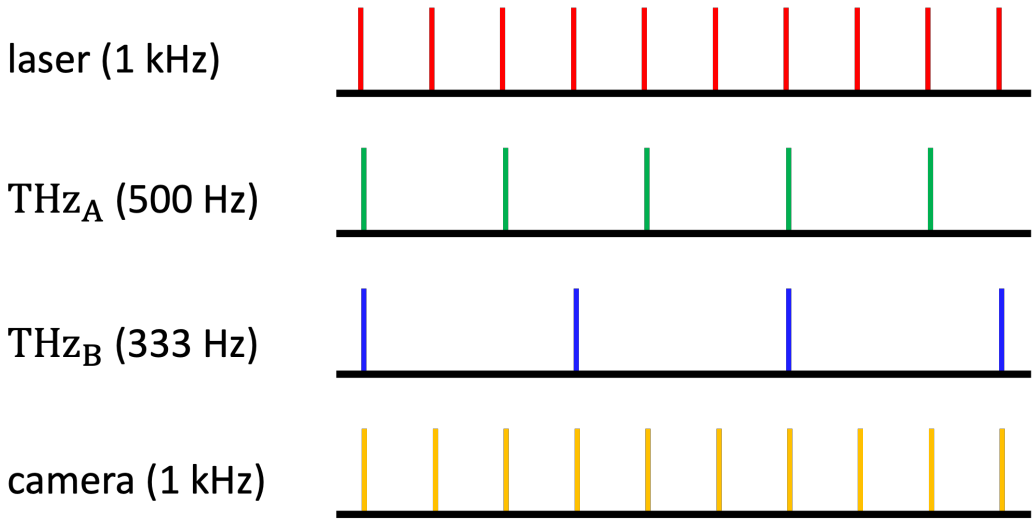

Figure 2.7: Differential chopping scheme for the selective isolation of 2D-TTR signals. Vertical lines indicate when the signals are on. The camera is only employed in the single-shot detection scheme.

the single-shot detection schemes, as shown in the purple and black dashed boxes in Fig. 2.6, respectively.

In the conventional stage-scan detection scheme, the probe beam is focused through a 1 mm through hole on the final OAP mirror to the same position in space as the THz focus. The sample is mounted on a computer-controlled translation stage to position the sample precisely at the THz focus. For 1D TKE spectroscopy, only one of the two THz pump pulses is used. Temporal overlap between the THz pump and 800 nm probe pulse is achieved by controlling the optical path length of the probe pulse. The THz-induced transient birefringence of the sample is measured through the rotation of the probe polarization, which is detected with a pair of crossed polarizers and a photodiode. Phase-sensitive detection is achieved by a heterodyne scheme, where a quarter-wave plate ($\lambda/4$) is introduced with the fast axis slightly detuned to create a local oscillator (LO) component that is orthogonal to the probe polarization. This LO passes through the analyzing polarizer and heterodynes with the signal electric field on the photodiode to amplify the detected signal and enable phase-sensitive detection. The THz pump beam is modulated at $\frac{1}{2}$ of the laser repetition rate to enable lock-in detection, which isolates the small nonlinear signal and rejects common mode noise. Finally, the TKE spectra is measured in the time domain by scanning the probe delay stage and recording the lock-in amplifier output with a data acquisition (DAQ) card (National Instrument).

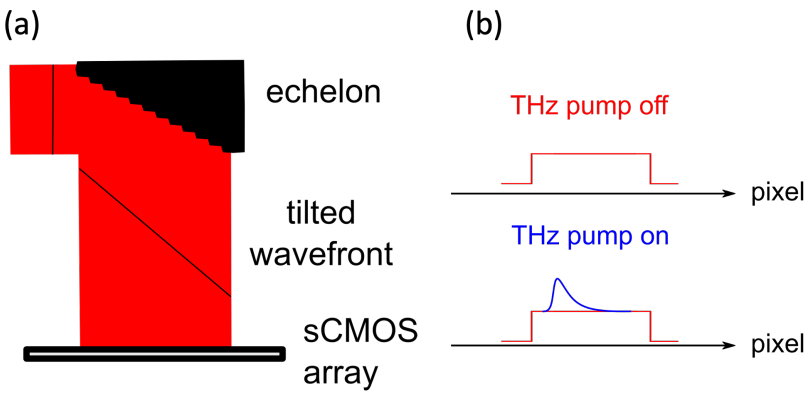

Figure 2.8: Echelon-based single-shot detection scheme. (a) "Time-to-pixel" mapping in the single-shot detection scheme. (b) Horizontal slice of the camera image encodes the time-delay information. The different between the THz pump on and pump off images yield the TKE spectra.

To perform 2D-TTR experiments, both THz beams are introduced into the OAP relay and onto the sample. The linear THz beam profile at the focus is characterized with real-time 2D electro-optic (EO) imaging [40] to achieve good spatial and temporal overlap between the THz pulses. We have further developed an imaging method, described in detail in Chapter 3, to characterize the nonlinear THz focus and directly optimize for 2D-TTR signal. A spot size of 160 μm in diameter is typically achieved for the nonlinear THz beam profile in our 2D-TTR experiments, which is close to diffraction limit for our broadband THz pulses. The two THz beams are modulated at $\frac{1}{2}$ and $\frac{1}{3}$ of the laser repetition rate, respectively. This differential-chopping scheme (Fig. 2.7) enables the selective detection of the 2D-TTR signal using a lock-in amplifier at the difference frequency, which is $\frac{1}{6}$ of the laser repetition rate. The time delays t_1 and t_2 are controlled by optical delay stages in the THz B pump beam and the probe beam, respectively. In practice, we typically step the t_1 delay stage to specific values and measure the response from the sample along t_2. The full 2D-TTR spectra is then re-constructed from a series of t_2 slices at equally-stepped t_1 positions. The time domain 2D-TTR spectra is generally sampled at 30 fs resolution, which corresponds to a Nyquist frequency of $\sim$ 17 THz.

The single-shot detection scheme for TKE spectroscopy was developed by my mentor Griffin [5] when I first joined the group. The heart of the single-shot method is a reflective echelon [41, 42], manufactured from nickle using computer numerically controlled (CNC) machines in Japan, that has 1000 steps inset horizontally across the surface. The steps of the echelon effectively act as 1000 independent mirrors,

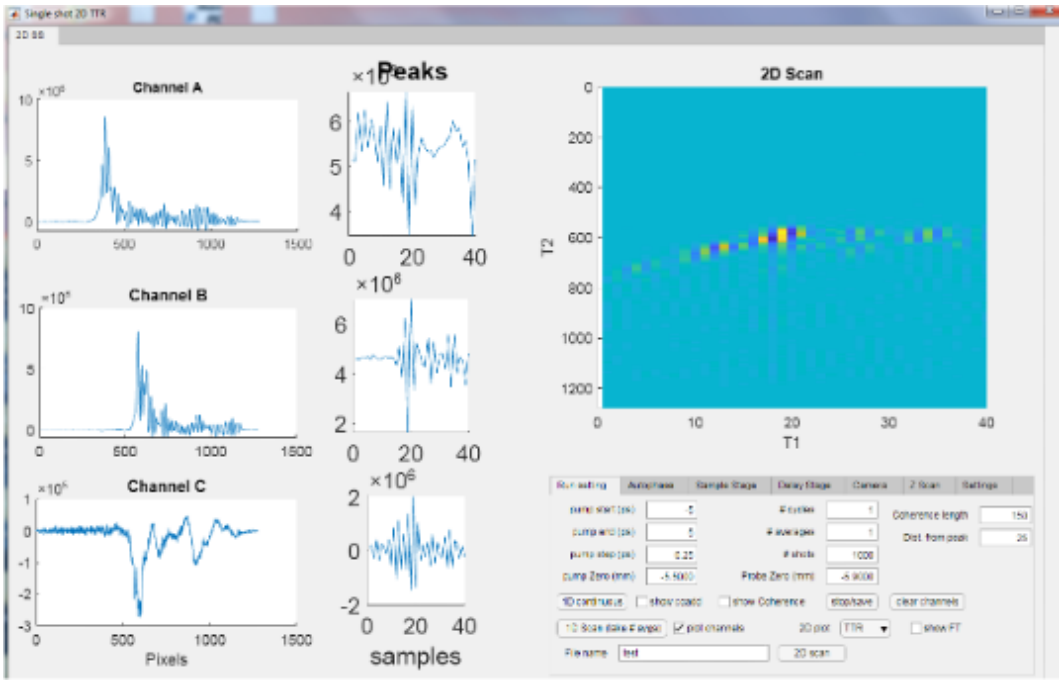

Figure 2.9: Screenshot of the 2D-TTR GUI during a measurement. Channels A, B, and C corresponds to the demodulated signals at $\frac{1}{2}$, $\frac{1}{3}$, and $\frac{1}{6}$ of the laser repetition rate, respectively.

each with a slight optical delay relative to the adjacent steps defined by the depth of each step. This results in a "tilted wavefront," in which the optical time delay varies linearly across the beam diameter. The echelon typically employed in our work has a step depth of 5 μm, which corresponds to ~30 fs of optical delay between adjacent beamlets. To illuminate the whole echelon, the beam is expanded using two reflective telescopes to reach $\sim$ 30 mm in diameter. A series of lenses are used to transfer the image of the echelon surface onto a sCMOS camera detector array (ANDOR Zyla) with a roughly 1:1 magnification to create a "time-to-pixel" mapping. In other words, the series of beamlets, which are reflected off the echelon surface and encode the time-delay information, are mapped onto $\sim$ 1000 pixels across the sCMOS array, as shown in Fig. 2.8a. The time domain TKE spectra is obtained from the difference between horizontal slices of the THz pump-on and the pump-off images, as shown in Fig. 2.8b.

To extend the single-shot detection scheme to 2D-TTR spectroscopy, a lock-in detection routine was implemented in MATLAB to enable selective detection of the 2D-TTR signal [3]. The same differential-chopping scheme described in Fig. 2.7 is employed. Analogous to the stage scan method for 2D-TTR, the two THz pump

beams are modulated at $\frac{1}{2}$ and $\frac{1}{3}$ of the laser repetition rate, respectively, and the 2D-TTR signal is detected selectively at $\frac{1}{6}$ of the laser repetition rate. The camera is externally triggered by the TTL output of the Legend Elite at 1 kHz to capture every laser shot. Typically, series of 1000 (1 second) or 5000 (5 seconds) images are taken for a single average. To ensure consistent phase of the signals between different image series, the TTL signals of the optical choppers are also digitized and used in the demodulation process. Specifically, we ensure that both THz pump pulses are on in the first camera frame of the image series. I developed a graphic user interface (GUI) that supports simultaneous demodulation of all three signal channels at $\frac{1}{2}$, $\frac{1}{3}$, and $\frac{1}{6}$ of the laser repetition rate. As shown in Fig. 2.9, the three channels are independently recorded and the 2D-TTR spectra is constructed slice by slice. The GUI further incorporates all the opto-mechanical elements to automate measurement of 2D-TTR spectra, which allows overnight averaging of weak 2D-TTR signals.

The single-shot detection scheme effectively replaces one optical delay stage with a multiplexed camera, which significantly reduces experimental time for 2D-TTR spectroscopy (recall that the acquisition time for multidimensional spectroscopy scale exponentially with the number of axes). In practice, the acquisition time for a typical 6-by-6 ps 2D-TTR spectra is reduced from 2 hours for the stage-scan method to only few minutes for the single-shot method, making investigation into weak signals or long nuclear dynamics in liquids possible. Note that in the single-shot detection scheme, the tilted wavefront of the probe pulse may introduce significant artifacts if the *wavevectors* of the probe pulse play a role in the nonlinear process, such as the excitation and detection of phase-matched phonon-polaritons. Imaging aberrations in crystalline solids may also limit the Nyquist detection frequency to $\sim$ 10 THz, leading to artificially broadened responses for high frequency features, such as the onset of the electronic response. We therefore optimize and directly characterize the image transfer function, which is fit to edge-spread functions to quantify the degree of broadening. This minimizes imaging aberrations and ensures accurate single-shot measurements.

References

[1] Peter Hamm. *Principles of Nonlinear Optical Spectroscopy: A Practical Approach or: Mukamel for Dummies*. 2005.

[2] Robert W. Boyd. *Nonlinear Optics*. Vol. 53. Elsevier, 2003, pp. 1–578.

[3] Griffin Mead et al. “Sum-frequency signals in 2D-Terahertz-Terahertz-Raman spectroscopy.” *The Journal of Physical Chemistry B* 124.40 (2020), pp. 8904–8908.

[4] Janne Savolainen, Saima Ahmed, and Peter Hamm. “Two-dimensional Raman-terahertz spectroscopy of water.” *Proceedings of the National Academy of Sciences* 110.51 (2013), pp. 20402–20407.

[5] Griffin Mead et al. “An echelon-based single shot optical and terahertz Kerr effect spectrometer.” *Review of Scientific Instruments* 90.5 (2019), p. 053107.

[6] Marco A. Allodi, Ian A. Finneran, and Geoffrey A. Blake. “Nonlinear terahertz coherent excitation of vibrational modes of liquids.” *Journal of Chemical Physics* 143.23 (2015).

[7] Matthias C. Hoffmann et al. “Terahertz Kerr effect.” *Applied Physics Letters* 95.23 (2009), pp. 2007–2010.

[8] David A. Turton et al. “A complete experimental and numerical study of the terahertz dynamics of methanol.” *Optics InfoBase Conference Papers* (2006), pp. 1–3.

[9] Mohsen Sajadi, Martin Wolf, and Tobias Kampfrath. “Transient birefringence of liquids induced by terahertz electric-field torque on permanent molecular dipoles.” *Nature Communications* 8 (2017), pp. 1–9.

[10] Hang Zhao et al. “Ultrafast hydrogen bond dynamics of liquid water revealed by terahertz-induced transient birefringence.” *Light: Science and Applications* 9.1 (2020).

[11] Peter Hamm and Martin Zanni. *Concepts and Methods of 2D Infrared Spectroscopy*. Cambridge: Cambridge University Press, 2011.

[12] Brittany E. Knighton et al. “Examining nonlinear terahertz photonic and phononic excitation with two-dimensional spectroscopy.” *International Conference on Infrared, Millimeter, and Terahertz Waves, IRMMW-THz* 2019-Septe (2019), pp. 45–47.

[13] Brittany E. Knighton et al. “Terahertz waveform considerations for nonlinearly driving lattice vibrations.” *Journal of Applied Physics* 125.14 (2019).

[14] Tomislav Begušić and Geoffrey A. Blake. “Two-dimensional infrared-Raman spectroscopy as a probe of water’s tetrahedrality.” *Nature Communications* 14.1 (2023).

[15] Andrei Tokmakoff. “Orientational correlation functions and polarization selectivity for nonlinear spectroscopy of isotropic media. I. Third order.” *The Journal of Chemical Physics* 105.1 (1996), pp. 1–12.

[16] Yoshitaka Tanimura and Shaul Mukamel. “Two-dimensional femtosecond vibrational spectroscopy of liquids.” *The Journal of Chemical Physics* 99.12 (1993), pp. 9496–9511.

[17] William O. Hutson, Austin P. Spencer, and Elad Harel. “Ultrafast four-dimensional coherent spectroscopy by projection reconstruction.” *Journal of Physical Chemistry Letters* 9.5 (2018), pp. 1034–1040.

[18] Huib J. Bakker and James L. Skinner. “Vibrational spectroscopy as a probe of structure and dynamics in liquid water.” *Chemical Reviews* 110.3 (2010), pp. 1498–1517.

[19] Martin Thämer et al. “Ultrafast 2D IR spectroscopy of the excess proton in liquid water.” *Science* 350.6256 (2015), pp. 78–82.

[20] Ian A. Finneran et al. “2D THz-THz-Raman photon-echo spectroscopy of molecular vibrations in liquid bromoform.” *Journal of Physical Chemistry Letters* 8.18 (2017), pp. 4640–4644.

[21] Haw-Wei Lin, Griffin Mead, and Geoffrey A. Blake. “Mapping LiNbO$_3$ phonon-polariton nonlinearities with 2D THz-THz-Raman spectroscopy.” *Physical Review Letters* 129.20 (2022), p. 207401.

[22] Tibbets Clara. *Coherent Multidimensional Spectroscopy*. Vol. 226. 2019, pp. iii–xvii.

[23] Maksim Grechko et al. “Coupling between intra-and intermolecular motions in liquid water revealed by two-dimensional terahertz-infrared-visible spectroscopy.” *Nature Communications* 9.1 (2018).

[24] Ko Okumura and Yoshitaka Tanimura. “Two-dimensional THz spectroscopy of liquids: Non-linear vibrational response to a series of THz laser pulses.” *Chemical Physics Letters* 295.4 (1998), pp. 298–304.

[25] Hironobu Ito, Taisuke Hasegawa, and Yoshitaka Tanimura. “Calculating two-dimensional THz-Raman-THz and Raman-THz-THz signals for various molecular liquids: The samplers.” *Journal of Chemical Physics* 141.12 (2014).

[26] Tatsushi Ikeda, Hironobu Ito, and Yoshitaka Tanimura. “Analysis of 2D THz-Raman spectroscopy using a non-Markovian Brownian oscillator model with nonlinear system-bath interactions.” *Journal of Chemical Physics* 142.21 (2015).

[27] Hironobu Ito, Taisuke Hasegawa, and Yoshitaka Tanimura. “Calculating two-dimensional THz-Raman-THz and Raman-THz-THz signals for various molecular liquids: The samplers.” *Journal of Chemical Physics* 141.12 (2014).

[28] Ju Yeon Jo, Hironobu Ito, and Yoshitaka Tanimura. “Full molecular dynamics simulations of liquid water and carbon tetrachloride for two-dimensional Raman spectroscopy in the frequency domain.” *Chemical Physics* 481 (2016), pp. 245–249.

[29] Carmine Somma et al. “High-field terahertz bulk photovoltaic effect in lithium niobate.” *Physical Review Letters* 112.14 (2014).

[30] Ahmed Ghalgaoui et al. “Terahertz polaron oscillations of electrons solvated in liquid water.” *Physical Review Letters* 126.9 (2021), p. 097401.

[31] Ilan Hurwitz et al. “Single beam low frequency 2D Raman spectroscopy.” *Optics Express* 28.3 (2020), p. 3803.

[32] A. Tokmakoff et al. “Two-dimensional Raman spectroscopy of vibrational interactions in liquids.” *Physical Review Letters* 79.14 (1997), pp. 2702–2705.

[33] David A. Blank, Laura J. Kaufman, and Graham R. Fleming. “Fifth-order two-dimensional Raman spectra of CS2 are dominated by third-order cascades.” *The Journal of Chemical Physics* 111.7 (1999), pp. 3105–3114.

[34] Andrey Shalit et al. “Terahertz echoes reveal the inhomogeneity of aqueous salt solutions.” *Nature Chemistry* 9.3 (2017), pp. 273–278.

[35] David Sidler and Peter Hamm. “Feynman diagram description of 2D-Raman-THz spectroscopy applied to water.” *Journal of Chemical Physics* 150.4 (2019).

[36] David Sidler and Peter Hamm. “A Feynman diagram description of the 2D-Raman-THz response of amorphous ice.” *Journal of Chemical Physics* 153.4 (2020).

[37] Beliz Sertcan et al. “Low-frequency anharmonic couplings in crystalline bromoform: theory.” *The Journal of Chemical Physics* 195107.2020 (2022).

[38] Balazs Monoszlai et al. “High-energy terahertz pulses from organic crystals: DAST and DSTMS pumped at Ti:sapphire wavelength.” *Optics Letters* 38.23 (2013), p. 5106.

[39] Carmine Somma et al. “Ultra-broadband terahertz pulses generated in the organic crystal DSTMS.” *Optics Letters* 40.14 (2015), p. 3404.

[40] Q. Wu, T. D. Hewitt, and Xi-Cheng Zhang. “Two-dimensional electro-optic imaging of THz beams.” *Applied Physics Letters* 69.8 (1996), pp. 1026–1028.

[41] Yuki Ikegaya et al. “Real-time observation of phonon-polariton dynamics in ferroelectric LiNbO3 in time-frequency space.” *Applied Physics Letters* 107.6 (2015).

[42] Tomonori Kuribayashi et al. “Anharmonic phonon-polariton dynamics in ferroelectric LiNbO3 studied with single-shot pump-probe imaging spectroscopy.” *Journal of Applied Physics* 123.17 (2018).

Chapter 3

CHARACTERIZATION OF THE NONLINEAR THZ FOCUS FOR 2D THZ SPECTROSCOPY

Adapted with permission from:

Haw-Wei Lin, Pin-Hsun Hsieh, Griffin Mead, Geoffrey A. Blake. "Characterization of the nonlinear THz focus for 2D THz spectroscopy." *Journal of the Optical Society of America B* (2024), *Accepted*.

3.1 Abstract

We present a sensitive imaging method capable of the selective characterization of the nonlinear THz beam profile, providing a direct handle to optimize $\chi^{(3)}$ light-matter interactions that are critical to two-dimensional (2D) THz spectroscopies. In particular, this method facilitates the development of experimentally-challenging 2D THz spectroscopies with multiple THz emitters, which enables direct investigations of fast picosecond dynamics in liquids and solids that are challenging in single-emitter 2D THz spectroscopic setups.

3.2 Introduction

In recent years, advancements in the generation of ultrafast broadband terahertz (THz) pulses, reaching above 1 MV/cm in peak electric field strengths and exceeding 10 THz in bandwidth, have enabled novel investigations of various condensed matter phenomenon using nonlinear THz spectroscopy [1, 2]. In particular, ultrafast two-dimensional (2D) THz spectroscopic techniques have attracted significant attention due to their unique capability to deconvolve and extract dynamics and coupling information from broad THz spectral features [3]. Recent demonstration of various types of 2D THz spectroscopies have provided detailed characterization of the fast reorientation dynamics (100s of fs) of water and aqueous solutions [4, 5], measured nonlinear rotational echos (100s of ps) in the gas phase [6], and directly observed nonlinear coupling interactions of phonon-polariton (5-10 ps) [7] as well as magnon (10s of ps) modes [8].

A number of the available 2D THz techniques, including 2D THz spectroscopy [6, 8, 9] and 2D THz-THz-Raman (2D-TTR) spectroscopy [7, 10], employ multiple

THz pump pulses that must be temporally and spatially overlapped at the sample. Researchers have developed two primary experimental layouts for 2D THz spectroscopy to achieve this. In the single-emitter geometry, two time-delayed optical or mid-infrared (mid-IR) pump beams are combined co-linearly prior to the THz emitter crystal to generate two co-linear THz emission pulses, which are focused with off-axis parabolic (OAP) mirrors to achieve sufficiently high THz peak field strengths [6, 8, 9, 11]. While this method provides ease of alignment, time-delays within a few ps cannot be easily accessed due to nonlinear interactions between pump pulses in the THz emitter crystal [6], making investigation of room-temperature vibrational dynamics (typically < 10 ps in lifetime) in liquids and solids challenging.

To access fast nuclear dynamics, one can instead combine two THz pulses from two individual THz emitters to eliminate interactions in the emitter crystal. 2D-TTR spectroscopy with this two-emitter geometry has successfully demonstrated investigation of ps-vibrational dynamics in organic halogenated liquids [10] and nonlinear couplings of phonon-polaritons in $LiNbO_3$ [7]. Typically, a wire-grid polarizer (WGP) is used to combine two orthogonally polarized THz beams co-linearly into the OAP relay due to the lack of THz-compatible beam splitters. The tight-focusing OAP relay can introduce significant aberrations to the THz mode quality and the spatial overlap of the multiple THz pulses if not properly aligned, leading to significant decrease in signal-to-noise. Thus, characterization of the spatial, temporal, and field strength parameters of the co-linear THz pump pulses at the sample position is crucial to ensure consistent and reliable measurements with 2D THz spectroscopy. For the temporal and field strength information of the THz pulses, there are several well-established methods such as electro-optic (EO) sampling [12, 13] and air-breakdown coherent detection (ABCD) [14]. However, imaging tools available for visualizing the spatial distribution of intense THz pulses at the focal region are significantly more limited [15]. Off-the-shelf THz camera products often employ bolometer- or pyroelectric-based detectors [16], which have large pixel sizes (typically $> 15\mu$m), slow response times, and long read-out times [17]. The use of additional filters and attenuators are generally necessary to block ambient thermal background and prevent saturation, which can disperse and distort the spatial profile of the THz focus. More recently, Si-based charge-coupled device (CCD) cameras have been shown to be able to directly detect THz photons through an electron tunneling mechanism [17, 18]. However, due to the large mismatch in THz photon energy (few meV) and the bandgap of Si ($\sim$1.1 eV), the sensitivity is moderate with a detection limit around 5 MV/cm in THz field strength [18].

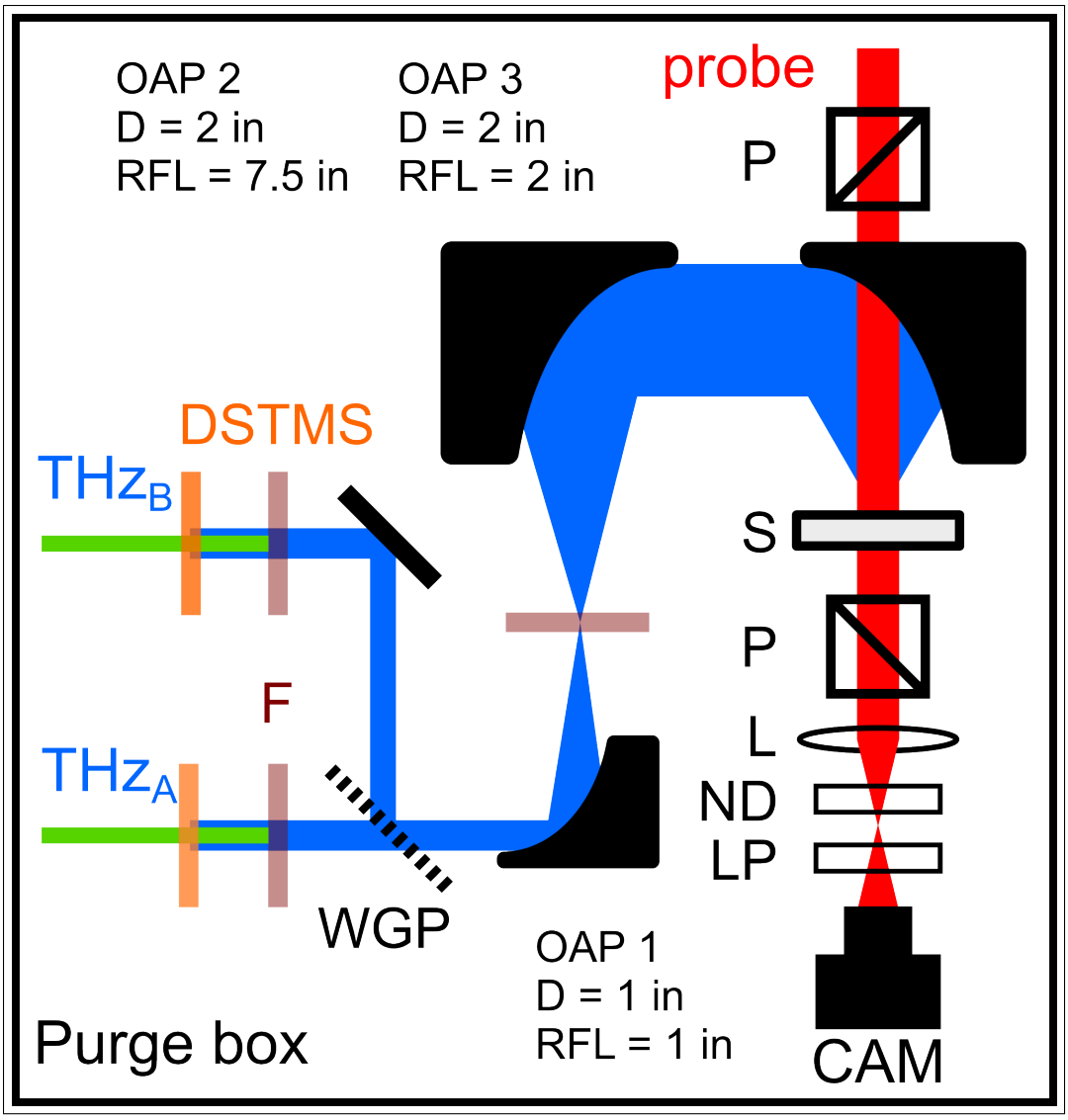

Figure 3.1: Experimental layout for the nonlinear imaging technique. F: 20 THz long-pass filter (QMC Instruments); P: polarizers; WGP: wire-grid polarizer; S: sample/100 μm GaP; ND: neutral density filter; LP: 750 nm long-pass filter; L: imaging lens. Green: 1.4 μm pump pulse; Red: 800 nm probe; Blue: THz pump pulse.

2D-EO imaging techniques, initially developed by Wu et. al.[19], utilizes the $\chi^{(2)}$ response of EO crystals to measure THz electric field distributions. However, as the $\chi^{(2)}$ response is linear in THz field strength, 2D-EO imaging does not provide adequate characterization of the nonlinear focus where $\chi^{(3)}$ light-matter interactions measured by 2D THz spectroscopy take place. Thus, there is need for a sensitive imaging method to selectively characterize the nonlinear beam profile of two-emitter 2D THz spectroscopies to allow rigorous signal optimization.

In this work, we utilize the $\chi^{(3)}$ response of GaP to provide spatial characterization of the nonlinear THz focus. Using differential chopping and a fast frame-rate camera, the $\chi^{(3)}$ interaction area of 2D THz spectroscopy was selectively isolated from other lower order signals. We demonstrate the ease of implementation of this novel imaging method in 2D-TTR spectroscopy, where modifications were made only to the probe beam path. This technique will facilitate the development of 2D THz spectroscopies in the study of important fast vibrational dynamics in liquids and solids.

3.3 Experimental Setup

An experimental schematic of the nonlinear imaging technique applied to 2D-TTR spectroscopy is shown in Fig. 3.1. Two broadband THz pump pulses (1-8 THz) are generated from two DSTMS [20] emitter crystals (Swiss THz) with the 1.4 μm output of an optical parametric amplifier (OPA), each 250 μJ per pulse. The THz pulses are orthogonally-polarized and combined with a wire-grid polarizer to be co-linear before entering a three-OAP relay, which expands and tightly focuses the THz pulses at the sample position. Crucially, the imaging technique makes no insertion or modification to the THz beam paths. As a result, optimized THz pulses can be directly incorporated into 2D-TTR spectroscopy with only changes to probe detection optics. A 100 μm thick, <110> oriented GaP crystal is placed precisely at the focus of the last OAP with a computer-controlled stepper-motor stage. A near-IR probe pulse (800 nm, 35 fs) illuminates an area of the crystal larger than that of the THz focus. We adapted the cross-polarized detection scheme in 2D-EO imaging [19], which provides extremely low background and greater than 10^8 extinction ratios. This sensitive detection scheme is critical to the detection of the 2D optical intensity of rotated probe photons due to nonlinear interactions between the probe and THz pulses. A biconvex lens (f = 200 mm) is used to image the surface of the GaP crystal onto a fast frame rate sCMOS camera (ANDOR Zyla 5.5MP) with a 1:1 magnification. A 750 nm long-pass filter and a 2.00 ND filter are placed in front of the sCMOS camera to remove background contributions and avoid saturation. The filters are placed after the GaP crystal to avoid distortion of the THz beam. The typical EO sampled THz pulse shape and bandwidth in air is shown in Fig. 3.2a and 3.2b respectively. The oscillatory features after the main THz pulse are due to water vapor.

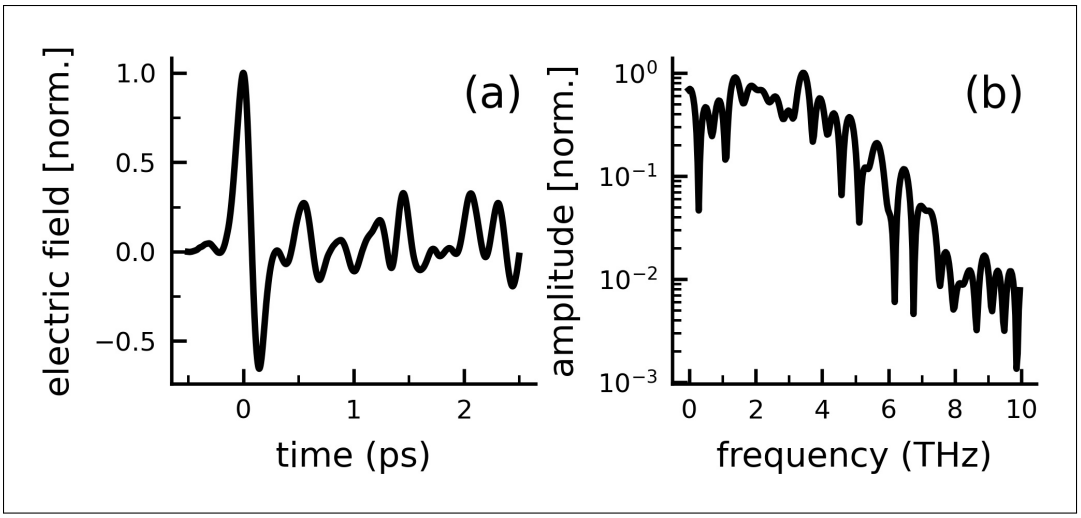

Figure 3.2: Characterization of the THz pulse shape. (a) Time-resolved, EO sampled THz_A pulse shape in air. (b) Corresponding bandwidth of THz_A obtained from Fourier Transform.

3.4 Results and Discussion

The key to selective isolation of the nonlinear THz overlap region is the differential chopping scheme we employ. Specifically, the camera operates at the laser repetition rate (1 kHz) with a region of interest (ROI) set to 40-by-40 pixels and an exposure time of 880 μs. The two THz beams THz_A and THz_B are modulated at $\frac{1}{2}$ (500 Hz) and $\frac{1}{3}$ (333.33 Hz) of the laser repetition rate, respectively. Due to the cross-polarized detection scheme, the camera response is sensitive to anisotropic light-matter interactions. Given the MV/cm THz field strengths employed in 2D THz spectroscopies, we consider both second-order (EO effect) and third-order (Kerr effect) anisotropic contributions to the image S, which is given as [21]

$$S \propto \chi^{(2)}(E_A^{THz} + E_B^{THz}) + \chi^{(3)}(E_A^{THz} + E_B^{THz})^2 \tag{3.1}$$

where E_A^{THz} and E_B^{THz} are the field strengths of the THz pulses THz_A and THz_B, and $\chi^{(2)}$ and $\chi^{(3)}$ are the second- and third-order nonlinear susceptibility of GaP, respectively. Expanding Eq. 3.1 yields fives nonlinear terms, which are the second-order terms $\chi^{(2)}E_A^{THz}$ and $\chi^{(2)}E_B^{THz}$, and the third-order terms $\chi^{(3)}(E_A^{THz})^2$, $\chi^{(3)}(E_B^{THz})^2$, and $\chi^{(3)}(E_A^{THz}E_B^{THz})$. The third-order term $\chi^{(3)}(E_A^{THz}E_B^{THz})$ in particular is proportional to the electronic component in a 2D-TTR spectra, which is given as

$$S_{TTR}^{el} \propto \chi^{(3)} I_{probe} E_A^{THz} E_B^{THz} \tag{3.2}$$

where I_{probe} is the probe intensity. Specifically, the electronic component provides a quantitative estimate of the signal strength of 2D-TTR spectroscopy [7, 10]. As a

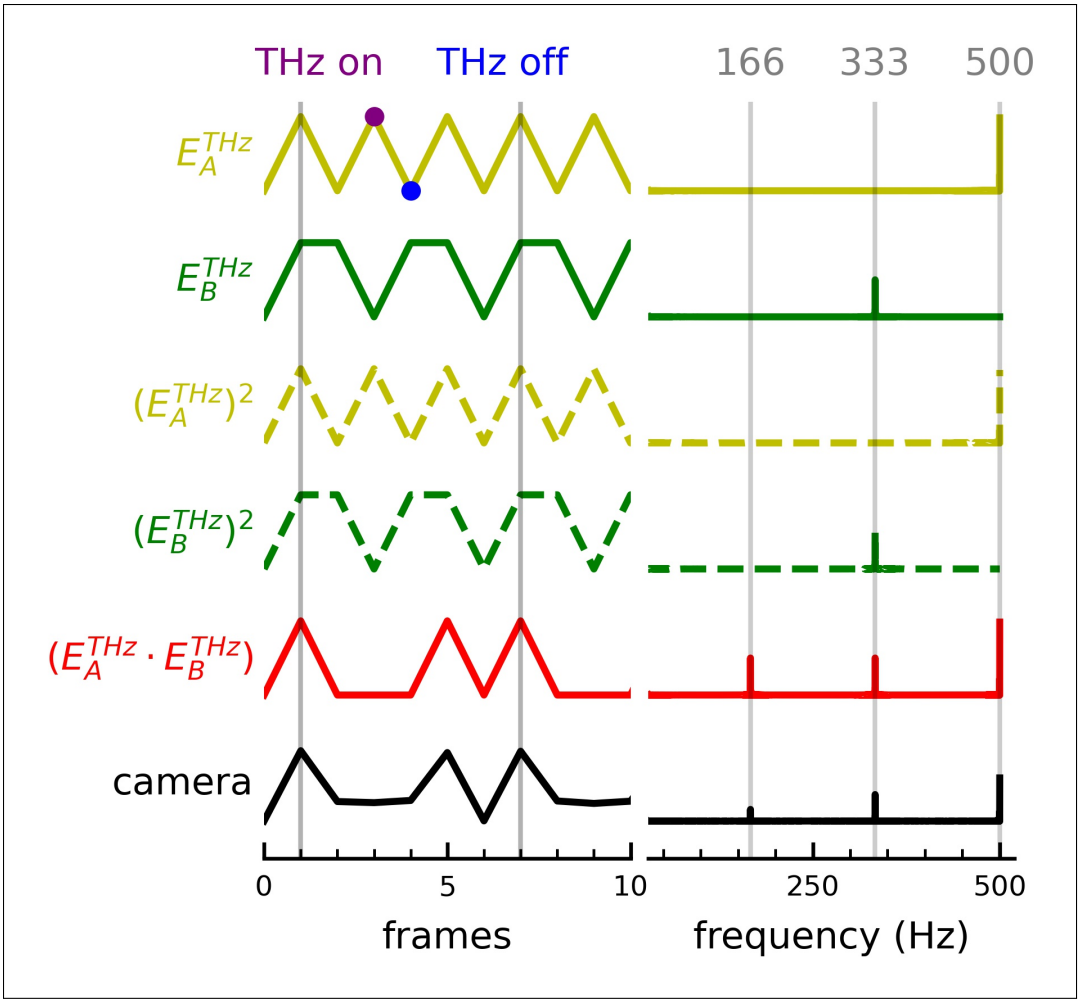

Figure 3.3: The differential chopping scheme. (Left) Time series of each individual nonlinear contribution to the camera response as a function of time. THz-on (purple) and THz-off (blue) frames are represented by 1 and 0 values. The camera trace shows the normalized amplitude of the center pixel in first 10 frames of a typical experimental measurement. (Right) Corresponding Fourier transform of each time series. The modulation frequencies (333 and 500 Hz) and the difference frequency (166 Hz) are highlighted.

result, imaging the intensity distribution of $\chi^{(3)} E_A^{THz} E_B^{THz}$, denoted as the nonlinear beam profile herein, on the surface of GaP provides a direct handle to optimize and improve the reliability of 2D-TTR experiments.

Figure 3.3 shows the modulation of the five nonlinear terms as a function of time, where a THz-on and a THz-off frame are represented by 1 and 0 values, respectively (the magnitude of the nonlinear susceptibility tensors are omitted for clarity). The time traces for E_A^{THz} and E_B^{THz} are constructed according to their experimental

modulation frequencies, while that for $(E_A^{THz})^2$, $(E_B^{THz})^2$, and $(E_A^{THz}E_B^{THz})$ are obtained from simple multiplications of the E_A^{THz} and E_B^{THz} traces. We note that the phase of the optical chopper for THz_B is chosen to result in an on-on-off time sequence that minimizes the number of laser shots blocked, as shown for the E_B^{THz} and $(E_B^{THz})^2$ traces. The Fourier transform of each time trace is shown at right, where clear peaks are observed at the modulation frequencies of E_A^{THz} (500 Hz), E_B^{THz} (333.33 Hz), and the difference frequency (166.66 Hz). In particular, the nonlinear term $\chi^{(3)}(E_A^{THz}E_B^{THz})$, which is precisely the signals of interest in 2D THz spectroscopy, is the only signal present at 166.66 Hz.

The experimentally measured camera signal is the sum of the five individual nonlinear contributions, which is shown in Fig. 3.3 with the black curve. To isolate the distinct nonlinear contributions of the image, we perform a phase-sensitive frequency demodulation routine that is analogous to that of a lock-in amplifier, which measures the amplitude of the underlying signals at a certain frequency. Specifically, a sine-wave (reference signal) with the desired modulation frequency f (166.66, 333.33, or 500 Hz) is generated and multiplied with the camera time series, which frequency shifts each peak in the Fourier spectrum by f. Then, we compute the fast Fourier transform of the multiplication product and measure the amplitude at zero frequency (DC), which is also the amplitude at f in the camera series. The phase of the reference signal is chosen to maximize the amplitude of the demodulated DC peak.

The nonlinear terms that contribute to each modulation frequency are evident from the Fourier transform spectra shown in Fig. 3.3. Applying the demodulation procedure, we decompose the camera signal into three distinct channels: S_{500} at 500 Hz, which includes the $\chi^{(2)}E_A^{THz}$, $\chi^{(3)}(E_A^{THz})^2$, and $\chi^{(3)}E_A^{THz}E_B^{THz}$ contributions; S_{333} at 333.33 Hz, which includes the $\chi^{(2)}E_B^{THz}$, $\chi^{(3)}(E_B^{THz})^2$, and $\chi^{(3)}E_A^{THz}E_B^{THz}$ contributions; and S_{166} at 166.66 Hz, which contains only the nonlinear term $\chi^{(3)}E_A^{THz}E_B^{THz}$. In particular, because the $\chi^{(3)}E_A^{THz}E_B^{THz}$ trace is not an ideal sine-wave, its contribution is not only present at the fundamental frequency of 166.66 Hz, but also its harmonics at 333.33 and 500 Hz. The ratios between the amplitudes at the harmonic frequencies (A_{333} and A_{500}) and the fundamental frequency (A_{166}) are uniquely dependent on the shape of the pulse train and can be determined by computing its Fourier transform, as shown in Fig. 3.3. For the $\chi^{(3)}E_A^{THz}E_B^{THz}$ trace in our work, $\frac{A_{333}}{A_{166}} = 1$ and $\frac{A_{500}}{A_{166}} = 2$. Thus, we can rearrange the demodulation products to obtain

three signals:

$$\begin{aligned} S_A = (S_{500} - 2S_{166}) &\propto \chi^{(2)} E_A^{THz} + \chi^{(3)} (E_A^{THz})^2 \\ S_B = (S_{333} - S_{166}) &\propto \chi^{(2)} E_B^{THz} + \chi^{(3)} (E_B^{THz})^2 \\ S_{A+B} = S_{166} &\propto \chi^{(3)} E_A^{THz} E_B^{THz} \end{aligned}$$

where contributions from the nonlinear third-order signal and that solely from E_A^{THz} and E_B^{THz} are separated. In particular, selective isolation of the nonlinear beam profile $\chi^{(3)} E_A^{THz} E_B^{THz}$ can be achieved by demodulation of the time series at $\frac{1}{6}$ of the laser repetition rate, which yields the S_{A+B} signal. This signal decomposition is verified later in this work through experiments with varying THz electric field strengths.

Figure 3.4a shows the nonlinear beam profile, S_{A+B}, measured on 100 μm GaP obtained by applying the demodulation routine to each individual pixel of the ROI in a 10000-shot (10 seconds) time series. Temporal overlap of the THz_A, THz_B, and probe beams were optimized with two optical delay stages, which controlled the path lengths of the THz_B and probe beams. The optical axis of the GaP crystal is set at 45° between the polarization of the two orthogonally-polarized THz pump beams to minimize second order contributions to S_A and S_B [22]. The nonlinear beam profile is fitted with a general two-dimensional elliptical Gaussian distribution, yielding $(1/e_x^2, 1/e_y^2)$ beam diameters of (147 μm, 187 μm). Recall that the intensity of the nonlinear beam profile is proportional to the nonlinear observable measured in 2D THz spectroscopies. Thus, the nonlinear imaging method enables rigorous optimization of the spatial and temporal overlap of the two THz pump beams to minimize spot size and maximize signal strength of 2D spectroscopy. Further, the high signal-to-noise nonlinear beam profile was obtained with a 10 second time series and few seconds of post-processing, allowing near real-time characterization during experimental alignment procedures. In addition, nonlinear imaging allows precise placement of samples with small physical dimensions within the nonlinear interaction area of the THz pump beams. This is particularly important for the analysis of novel quantum materials, whose synthesis often yield flakes few 100 μm in diameter, which is comparable to the THz interaction area in this work.

To verify the signal decomposition described above, we characterized the THz field strength dependence of the differentially modulate signals S_A, S_B, and S_{A+B}. 10000-shot kinetic series were taken on 100 μm GaP with variable THz_A and

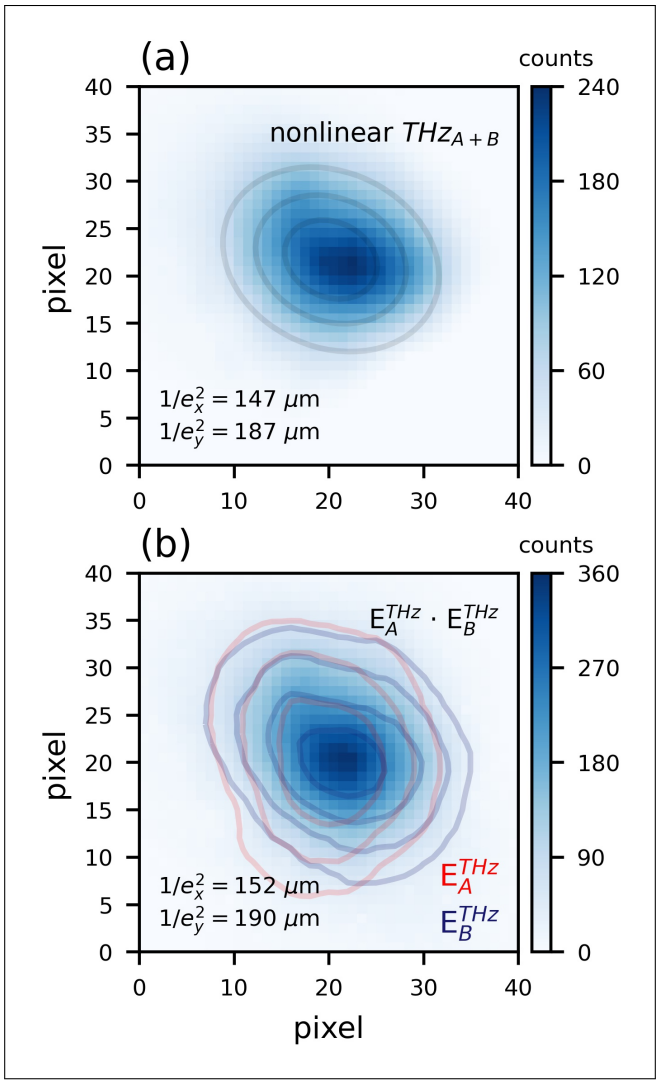

Figure 3.4: Characterization of the THz beam profile with the nonlinear imaging technique. (a) Nonlinear beam profile of 2D-TTR spectroscopy. Grey contours show the best fit 2D Gaussian distribuion. (b) Simulated nonlinear beam profile from the product of experimentally measured E_A^{THz} (red contours) and E_B^{THz} (blue contours) distributions.

fixed THz_B field strengths. The kinetic series of images were processed with the demodulation procedure described previously (including the correction to the harmonic contributions of $\chi^{(3)} E_A^{THz} E_B^{THz}$) to obtain the images of S_A, S_B, and S_{A+B}. For clarity, the total intensity of the 40-by-40 pixel image is analyzed as a function of THz_A field strength for each channel, as shown in Fig. 3.5. We note that the same trends are observed when the intensity of the beam center is used instead. The intensity of S_{A+B} (Fig. 3.5c) displays linear dependence with THz_A field strength, consistent with originating from the $\chi^{(3)} E_A^{THz} E_B^{THz}$ term. On the other hand, the

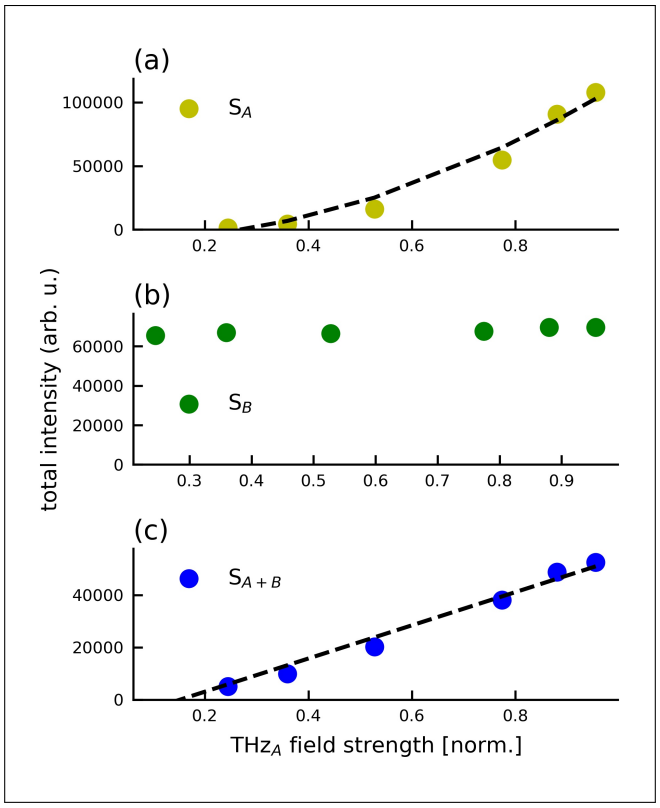

Figure 3.5: THz field strength dependence of the three differentially modulated channels (a) S_A, (b) S_B, and (c) S_{A+B}.

intensity of S_B remains constant while that of S_A exhibits primarily a quadratic dependence with changing THz_A field strength, as shown in Fig. 3.5a and b. This result is again consistent with our previous attribution of second- and third-order light matter interactions in S_A and S_B, which supports the demodulation and the harmonic amplitude correction routines. It further indicates that the third-order term $\chi^{(3)}(E^{THz})^2$ is dominant over the second-order term $\chi^{(2)}(E^{THz})$ at the THz field strengths of our experiments. Given the predominant third-order nature of the S_A and S_B signals, which is proportional to $\chi^{(3)}(E^{THz})^2$, a quantitative estimate of the beam profiles of E_A^{THz} and E_B^{THz} can be obtained from the square-root of the S_A and S_B images, respectively. As shown by the red and dark blue contours in Fig. 3.4b, the two THz beams are spatially well overlapped to within few μm (pixel size of 6.5 μm) with a $1/e^2$ radius of approximately 240 μm on average. The precise spatial overlap achieved between THz_A and THz_B pump beams, which were optimized utilizing the nonlinear imaging method presented in this work, highlights the consistency this method provides for 2D THz experiments. The nonlinear THz beam profile can further be estimated from multiplication of the E_A^{THz} and E_B^{THz}

profiles, as shown with the blue filled contour in Fig. 3.4b. The beam parameters are determined with 2D elliptical Gaussian fitting to be $(1/e_x^2, 1/e_y^2)$ =(152 μm, 190 μm), which agrees well with the direct measurement of the nonlinear beam profile. Slight over-estimations ($\sim$ 3%) of the beam parameters are likely a result of the involvement of second-order effects in the S_A and S_B channels, which are difficult to separate from power-scaling experiments. When the field strength of E_A^{THz} is reduced to 35%, which increases the relative ratio of the second-order contributions, the over-estimations increase to $\sim$ 10%, supporting the above hypothesis. Note that the calculated nonlinear beam profile relies on the results of the THz field strength dependence experiments, which revealed the dominance of the third-order effect at the 100s kV/cm to MV/cm field strengths employed in 2D THz spectroscopies. Under these strong field conditions, 2D EO imaging techniques may significantly misrepresent the true THz beam profiles due to involvement of higher-order effects, if power dependence experiments were not performed. While THz attenuators can be used to reduce the impact of higher-order contributions, they also introduce undesirable spatial and frequency distortions of the THz beam.

3.5 Conclusion

To summarize, we have presented a sensitive imaging method for 2D THz spectroscopy that selectively characterizes the nonlinear beam profile $\chi^{(3)} E_A^{THz} E_B^{THz}$ through differential chopping. Implementation of the nonlinear imaging method is demonstrated on 2D-TTR spectroscopy, where identical THz pump beam paths are retained and only minor modifications to the probe beam paths are made. This eliminates distortions to spatial and frequency distributions of the THz beams caused by attenuators that are often required by off-the-shelf THz imaging solutions or 2D-EO imaging techniques to avoid saturation or higher order effects. We further demonstrated complete assignment of the three differentially modulated signal channels and the light-matter interactions involved, which enabled characterization of the individual THz beam profiles simultaneously. Direct characterization of the nonlinear beam profile enables rigorous spatial and temporal optimization of the THz pump beams to maximize the signal strength of 2D THz spectroscopy, as evident by the precise spatial overlap achieved in this work with two independent THz emitters. This sensitive THz imaging method may open up new opportunities in non-colinear 2D THz spectroscopy to study fast vibrational dynamics within the first few ps, which are difficult to access in more common single-emitter setups.

References

[1] Harold Y. Hwang et al. "A review of non-linear terahertz spectroscopy with ultrashort tabletop-laser pulses." *Journal of Modern Optics* 62.18 (2015), pp. 1447–1479.

[2] Peter Hamm et al. "Perspective: THz-driven nuclear dynamics from solids to molecules." *Structural Dynamics* 4.6 (2017).

[3] Thomas Elsaesser, Klaus Reimann, and Michael Woerner. "Focus: Phase-resolved nonlinear terahertz spectroscopy - From charge dynamics in solids to molecular excitations in liquids." *Journal of Chemical Physics* 142.21 (2015).

[4] Janne Savolainen, Saima Ahmed, and Peter Hamm. "Two-dimensional Raman-terahertz spectroscopy of water." *Proceedings of the National Academy of Sciences* 110.51 (2013), pp. 20402–20407.

[5] Klaus Reimann, Michael Woerner, and Thomas Elsaesser. "Two-dimensional terahertz spectroscopy of condensed-phase molecular systems." *The Journal of Chemical Physics* 154.12 (2021), p. 120901.

[6] Frank Y. Gao et al. "High-speed two-dimensional terahertz spectroscopy with echelon-based shot-to-shot balanced detection." *Optics Letters* 47.14 (2022), p. 3479.

[7] Haw-Wei Lin, Griffin Mead, and Geoffrey A. Blake. "Mapping LiNbO$_3$ phonon-polariton nonlinearities with 2D THz-THz-Raman spectroscopy." *Physical Review Letters* 129.20 (2022), p. 207401.

[8] Jian Lu et al. "Coherent two-dimensional terahertz magnetic resonance spectroscopy of collective spin waves." *Physical Review Letters* 118.20 (2017), pp. 1–6.

[9] Jian Lu et al. "Nonlinear two-dimensional terahertz photon echo and rotational spectroscopy in the gas phase." *Proceedings of the National Academy of Sciences* 113.42 (2016), pp. 11800–11805.

[10] Griffin Mead et al. "Sum-frequency signals in 2D-Terahertz-Terahertz-Raman spectroscopy." *The Journal of Physical Chemistry B* 124.40 (2020), pp. 8904–8908.

[11] Courtney L. Johnson, Brittany E. Knighton, and Jeremy A. Johnson. "Distinguishing nonlinear terahertz excitation pathways with two-dimensional spectroscopy." *Physical Review Letters* 122.7 (2019), p. 73901.

[12] Q. Wu and Xi-Cheng Zhang. "Free-space electro-optic sampling of terahertz beams." *Applied Physics Letters* 67.September 1995 (1995), p. 3523.

[13] Alfred Leitenstorfer et al. "Detectors and sources for ultrabroadband electro-optic sampling: Experiment and theory." *Applied Physics Letters* 74.11 (1999), pp. 1516–1518.

[14] Jianming Dai, Jingle Liu, and Xi Cheng Zhang. "Terahertz wave air photonics: Terahertz wave generation and detection with laser-induced gas plasma." *IEEE Journal on Selected Topics in Quantum Electronics* 17.1 (2011), pp. 183–190.

[15] Hichem Guerboukha, Kathirvel Nallappan, and Maksim Skorobogatiy. "Toward real-time terahertz imaging." *Advances in Optics and Photonics* 10.4 (2018), p. 843.

[16] Antoni Rogalski and Fedir Sizov. "Terahertz detectors and focal plane arrays." *Opto-Electronics Review* 19.3 (2011), pp. 346–404.

[17] Mostafa Shalaby, Carlo Vicario, and Christoph P. Hauri. "High-performing nonlinear visualization of terahertz radiation on a silicon charge-coupled device." *Nature Communications* 6 (2015), pp. 1–5.

[18] Oleg V. Chefonov et al. "Terahertz beam spot size measurements by a CCD camera." *Optics Letters* 44.17 (2019), p. 4099.

[19] Q. Wu, T. D. Hewitt, and Xi-Cheng Zhang. "Two-dimensional electro-optic imaging of THz beams." *Applied Physics Letters* 69.8 (1996), pp. 1026–1028.

[20] Balazs Monoszlai et al. "High-energy terahertz pulses from organic crystals: DAST and DSTMS pumped at Ti:sapphire wavelength." *Optics Letters* 38.23 (2013), p. 5106.

[21] Robert W. Boyd. *Nonlinear Optics*. Vol. 53. Elsevier, 2003, pp. 1–578.

[22] Carlo Vicario, Mostafa Shalaby, and Christoph P. Hauri. "Subcycle extreme nonlinearities in GaP induced by an ultrastrong terahertz field." *Physical Review Letters* 118.8 (2017), p. 083901.

Chapter 4

SUM-FREQUENCY SIGNALS IN 2D-TERAHERTZ-TERAHERTZ-RAMAN SPECTROSCOPY

Adapted with permission from:

Griffin Mead, **Haw-Wei Lin**, Ioan B. Magdău, Thomas F. Miller, Geoffrey A. Blake. "Sum-frequency signals in 2D-Terahertz-Terahertz-Raman spectroscopy." *Journal of Physical Chemistry B* 124.40 (2020), pp. 8904–8908. DOI: 10.1021/acs.jpcb.0c07935

4.1 Abstract

We demonstrate that halogenated methane 2D-Terahertz-Terahertz-Raman (2D-TTR) spectra are determined by the complicated structure of the instrument response function (IRF) along f_1 and by the molecular coherences along f_2. Experimental improvements have helped increase the resolution and dynamic range of the measurements, including accurate THz pulse shape characterization. Sum-frequency excitations convolved with the IRF are found to quantitatively reproduce the 2D-TTR signal. A new Reduced Density Matrix model which incorporates sum-frequency pathways, with linear and harmonic operators fully supports this (re)interpretation of the 2D-TTR spectra.

4.2 Main text

Observing interactions within the low-frequency, thermally populated continuum of bath states is critical to developing a molecular understanding of liquid dynamics at room temperature. This energy regime is predominantly characterized by broad inter-molecular modes with short coherence times (~100s fs) which complicate the measurement and interpretation of potential energy, dipole and polarizability surfaces. One exception to this general observation are the intra-molecular vibrational modes of the halogenated methane (HM) family of liquids, whose well-defined coherent vibrational signals have long been observed in optical Kerr effect (OKE) experiments [1, 2].

Multidimensional time-resolved spectroscopy methods seek to disentangle these ambiguous spectra by introducing an additional time delay which separates dynam-

ics along a second axis. The 5th order Raman technique [3] extends OKE to two dimensions and provides information on electrical and mechanical anharmonicities of the liquid, but practical implementation of this method is quite challenging [4, 5]. A trio of 3^{rd} order terahertz-Raman hybrid spectroscopies have been proposed as alternatives to 5^{th} order Raman spectroscopy that avoid some technical challenges inherent to 5^{th} order spectroscopy [6–10]. However, new challenges emerge in the hybrid techniques, especially compared to the more common 2D-infrared (2D-IR) spectroscopy. First, there are no commercially available dispersive THz spectrometers with adequate sensitivity to directly detect the emitted THz signal in THz-Raman-THz (2D-TRT) and Raman-THz-THz (2D-RTT) measurements. Instead, the 2D-TRT/RTT techniques have used time-domain electro-optic sampling to capture the faint THz emission [11]. 2D-TTR avoids this step by using a Raman probe pulse which generates an easily detected near-IR signal photon. In all the cases of hybrid THz-Raman spectroscopies, the poorly defined THz wave vector precludes a phase-matching box-CARS style geometry that could be used to discriminate between signals originating from different quantum mechanical coherence pathways.

With 2D-TTR spectroscopy, complex spectra have been observed in several halogenated methane (HM) liquids, and were interpreted as signatures of coherent energy transfer pathways between intra-molecular vibrational modes [12–15]. A thorough re-investigation of two HM liquids — bromoform ($CHBr_3$) and chloroform ($CHCl_3$) — casts doubt on this original interpretation. Our new investigation is enabled by the development of a single-shot 2D-TTR spectrometer [16] which records tens of picoseconds of molecular dynamics in a single acquisition. From the order of magnitude speed-up, the new technique provides substantially higher signal-to-noise data which has allowed a much larger region of the molecular response to be measured, and at finer resolution.

We demonstrate through experiment, models, and theoretical simulations that the features observed in the HM 2D-TTR spectra arise from convolutions between the instrument response function (IRF) and linear interactions with the molecular polarizability operator Π. This interaction requires a scattering with two instantaneous THz photons, and is therefore referred to throughout the text as a sum-frequency (SF) excitation process. (Very recent experimental and theoretical works have also observed efficient phonon excitation through the same linear-Π interaction with two

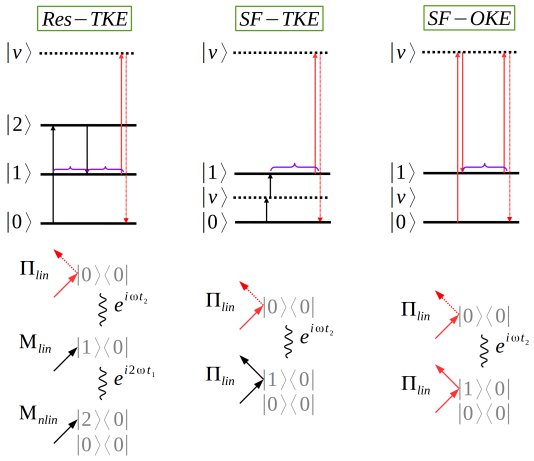

Figure 4.1: A resonant TTR signal requires dipole nonlinearities to excite a vibrational coherence — a representative process is illustrated in the Res-TKE (resonant terahertz Kerr effect) ladder and Feynman diagrams. In contrast, a sum-frequency excited molecular coherence is produced through interactions linear in the polarizability operator. The virtual state in SF-TKE is short-lived, and therefore the signal is highly dependent upon overlap between the two pump pulses. The familiar optical Kerr effect (SF-OKE) illustrates fundamental similarities with SF-TKE.

THz field interactions [17–19].) Resonant nonlinear interactions with the transition dipole operator M, while also in principal weakly allowed, are not detected.

We begin by re-examining the relative importance of the M (resonant) and Π (sum-frequency) excitation pathways in HM vibrational modes. Ladder diagrams in Fig. 4.1 illustrate the two competing pathways as well as the OKE process, which is analogous to SF-TKE. In order to observe the desired nonlinear THz signal, the resonant pathway must have a larger or (at least) comparable magnitude with the sum-frequency pathway. This is a difficult condition to satisfy in HMs since the resonant process is nonlinear with respect to M while the sum-frequency pathway is linear in Π.

Sum-frequency and resonant excitation pathways have distinct t_1 responses. A clear sign of resonant M interactions is a prolonged vibrational response along t_1 which arises from the generation of a vibrational coherence during the first THz field interaction. From 2D-TTR measurements, molecular coherences extending in excess of 5 ps along t_2 have been observed in HMs, suggesting a resonant signal should have a commensurate lifetime along t_1. In contrast, sum-frequency excitation cannot directly generate coherent states through a single field interaction, but instead require two instantaneous interactions. In this case, the extent of a

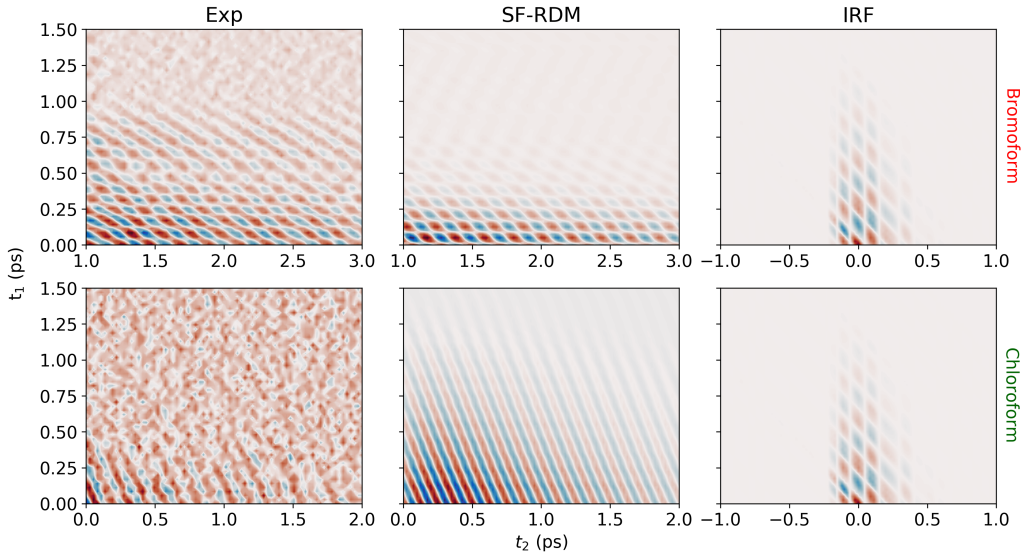

Figure 4.2: Top and bottom rows compare the experimental (Exp) bromoform and chloroform time-domain data to the SF-RDM models. The calculated IRF, whose THz electric fields are used as inputs to the SF-RDM model, is shown for reference (right column). Identical pulse shapes and IRFs are used for both SF-RDM models of bromoform and chloroform.

molecular response along t_1 will be determined by the duration of temporal overlap of the two THz electric field waveforms.

In Fig. 4.2 time-domain bromoform and chloroform measurements recorded under identical experimental conditions are shown. The initial key observation is that while the t_2 response is long-lived, the response along t_1 never extends past the region of THz field overlap. Both bromoform's and chloroform's vibrational coherent responses are therefore far more consistent with a SF excitation mechanism than a resonant process.

The different bandwidth requirements of the two processes provides a second argument supporting SF excitation as the dominant pathway. In both SF and resonant 2D-TTR pathways, a vibrational mode must begin and end the measurement in a population state. In addition, the Raman probe interaction only changes the vibrational quanta by ± 1. If a M non-linearity is present, one of the THz field interactions must produce either a zero-quanta or two-quanta excitation, which in the latter case necessitates a bandwidth spanning $\geq 2\omega$ [20]. (No evidence for zero-quanta transitions in HM vibrational modes have been observed.) Again, this is quite different

from 2D-IR spectroscopies. SF excitation, on the other hand, progresses with a bandwidth $\approx \omega/2$. The experimental THz field bandwidth spans 1-5 THz, and therefore the 2D-TTR experiment lacks the necessary frequency content to produce vibrational coherences arising from M non-linearities in the molecular Hamiltonian.

Given that sum-frequency excitation is the predominant source of the signals observed in 2D-TTR spectroscopy of HMs, a key mystery becomes how this mechanism, whose instantaneous nature precludes separating the two THz field interactions in time, can nonetheless produce a signal which varies along t_1? We interrogate the origins of this complex t_1 response by considering how the observed signal $S(t_1, t_2)$ depends upon the IRF $I(t_1, t_2)$ (Eq. 4.2). In a 2D-TTR experiment, two orthogonally polarized THz fields ($\vec{x}$, $\vec{y}$ in the laboratory frame) create a birefringent response within the room-temperature HM liquid sample. A $\vec{x}$ polarized Raman probe scatters off this birefringence, producing a $\vec{y}$ polarized signal field that is selectively isolated through an analyzing polarizer and differential chopping. The 2D-TTR signal is proportional to the anisotropic third-order molecular response function $R^{(3)}_{xyxy}(t_1, t_2)$, and contains information on the molecular orientational and vibrational correlation functions of the system. During the measurement process, this response is inevitably convolved with the experimental IRF, which in 2D-TTR is determined by the product of the two THz electric fields.

$$S(t_1, t_2) = I(t_1, t_2) \circledast R^{(3)}_{xyxy}(t_1, t_2) \tag{4.1}$$

Through the convolution theorem, the time-domain convolution becomes a multiplication between the IRF spectral power and the HM molecular response function upon transformation to the frequency domain.

$$\tilde{S}(f_1, f_2) = \tilde{I}(f_1, f_2) \cdot \tilde{R}^{(3)}_{xyxy}(f_1, f_2) \tag{4.2}$$

We study the impact of IRF convolution in two ways. First, we generate a time-domain model IRF (Fig. 4.2) using model THz field profiles (Fig. 4.5) that closely resemble experimental pulse shapes (see SI for details). An instantaneous SF process gives a molecular response which is a delta function in the time-domain (t_1) and a flat response in the corresponding frequency domain (f_1). In 2D-TTR, this amounts to a flat response along the f_1 axis, and a delta functions along the f_2 axis centered at the eigenmode frequencies of the molecular sample. Multiplication of this molecular response with the IRF yields the final measured signal. This results

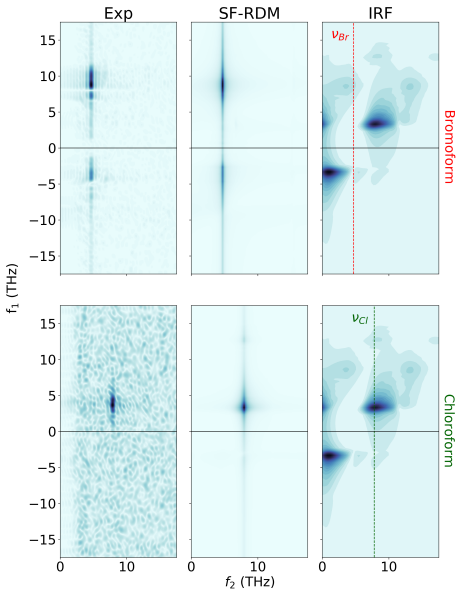

Figure 4.3: Top and bottom rows compare the experimental (Exp) bromoform and chloroform frequency-domain data to the SF-RDM model. The calculated IRF is shown for reference with vertical lines indicating where each HMs intramolecular vibrational mode samples the IRF. Note that the experimental and SF-RDM spectra are well matched, and arise from sampling the same IRF at different f_2 frequencies.

in simply selecting a slice of the IRF along f_1 at the eigenmode frequency. Using this simple model we find excellent agreement with the experimental spectra.

Second, we use the same THz field profiles that produce the IRF model as inputs to RDM simulations that consider sum-frequency excitation processes (SF-RDM). Again, we find near-quantitative agreement between the experimental data and theoretical simulations. Critically, no electrical or mechanical non-linearities are required to reach excellent agreement between the data and the IRF model/RDM simulations. The SF-RDM results precisely reproduce the experimental time-domain (Fig. 4.2) and frequency-domain (Fig. 4.3) responses, substantiating the claim that SF processes dominate the 2D-TTR response of HMs.

The agreement between experiment, SF-RDM, and model IRF are shown in Fig. 4.4. While bromoform and chloroform have different intra-molecular vibrational energies, we reproduce both spectra by slicing the same model IRF at their respective eigenmode frequencies along f_2. Crucially, this model mimics the non-specific sum-frequency excitation of vibrational coherences by the THz electric field. Unlike previous interpretations, here we do not invoke Feynman diagram pathways

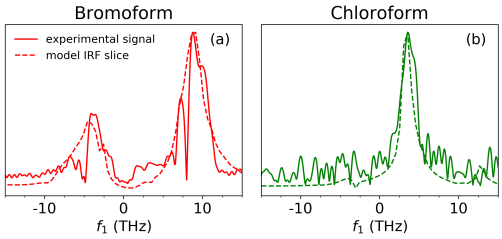

Figure 4.4: Comparison of experiment and IRF/RDM model. (a) Slices along f_1 at f_2=eigenmode of the IRF/RDM model and experimental response demonstrate the quality of fit for the bromoform data. Chloroform (b) is reproduced by slicing along the same IRF/SF-RDM model as shown in (a) at f_2=7.8 THz, instead of at bromoform's f_2=4.7 THz.

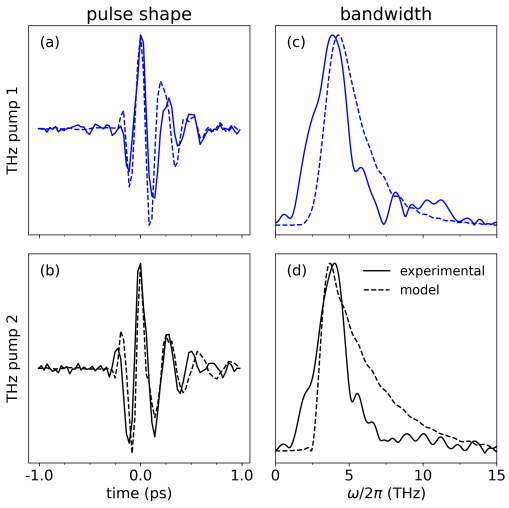

Figure 4.5: Comparison of the experimental and model THz pulse shapes (a,b) and corresponding bandwidths (c,d). See the SI for more detail on the optimization process used to obtain the model pulse shapes.

involving multi-quanta transitions between several vibrational modes; instead, the experimental IRF filtered through a single SF excitation pathway explains our observations.

That a two-quanta sum-frequency excitation pathway is predominantly responsible for vibrational coherences observed in 2D-TTR is also supported by estimations of chloroform and bromoform's transition dipole moments. From THz-TDS measurements and FT-IR literature, the bromoform and chloroform E mode's molar extinction coefficients were $\epsilon \approx 1 M^{-1} cm^{-1}$, suggestive of a vanishingly small transition dipole moment. Ab initio calculations similarly arrive at transition dipole

elements in the few milliDebye range. As a result, it would be very difficult to observe resonant excitation of these HM modes, even in the absence of interfering SF pathways. For comparison, 2D-IR spectroscopy on proteins is often performed by resonantly pumping the amide I stretch at $\sim$ 50 THz, which have ϵ $\sim$200-400 $M^{-1}cm^{-1}$. Not only are these oscillators intrinsically orders of magnitude stronger than HM vibrational modes, but the IR excitation field's $\delta\omega/\omega$ is also substantially narrower, which helps to selectively and resonantly generate the desired coherences while suppressing any SF contribution. Common sources of high intensity, sub-ps THz pulses (organic emitters, LiNbO3, etc) all have $\delta\omega \approx \omega$ and thus both Res and SF pathways must be considered when analyzing responses in the overlapping pump field region.

Finally, we would like to note that our conclusions regarding the excitation mechanism of intra-molecular vibrational modes of HMs in 2D-TTR spectroscopy likely do not alter analyses performed on similar systems in the complementary 2D-TRT and 2D-RTT experiments [11]. Those measurements attributed spectral features that remained post-deconvolution to couplings between a Raman-excited vibrational coherence and a resonant one-quanta interaction with bath modes of the liquid. Our conclusions are consistent with their observation that the IRF strongly determines the observed multi-dimensional experimental response.

In this work we provide extensive new experimental and theoretical data that leads to a simple reinterpretation of previous 2D-TTR measurements of HMs. With this new analysis, we explain the entire spectrum of both bromoform and chloroform through a convolution of the experiment's THz fields with the molecules' intra-molecular vibrational modes. No coherence pathways outside of the SF-TKE process in Fig. 4.1 are required. The new analysis is also fully consistent with the observed magnitudes of transition dipole moments and molecular polarizabilities.

Moving forward, there are two keys lessons. First, large transition dipoles are crucial for performing truly resonant 2D-TTR experiments. Halogenated methanes unfortunately do not satisfy this requirement, and the bright, complex signals observed can easily be mis-attributed to resonant processes. Second, nearly transform-limited half-cycle THz fields would maximize the field strengths achievable, greatly simplify the experimental IRF structure, and reduce ambiguities in the analysis of dynamics in molecular systems.

4.3 Supplemental information

2D-TTR Single shot spectrometer

Greater temporal resolution and sensitivity compared to previous research was achieved by developing a single-shot 2D-TTR spectrometer. This technique eliminates scanning of the probe delay line, producing substantial reductions in experimental acquisition time. With the imaging and echelon combination used for this work, each camera acquisition captures 30 ps of molecular response along t_2 at 28 fs resolution. Equivalent resolution of 28 fs steps are recorded along t_1, while the overall temporal extent of a typical data set spans 30×[5-10] ps ($t_2 \times t_1$). This represents ≥ 10× greater temporal extent compared to previous stage-scan 2D-TTR measurements [14]. Typical acquisition times ranged from a few hours to overnight (For comparison, previous stage-scan experiments required 48 hrs of averaging).

We briefly discuss the overall experimental setup (Fig. 4.6), and then provide specific details on the single-shot spectrometer's construction. A 1 kHz Coherent Legend HE regenerative amplifier, seeded with an 80 MHz Coherent Micra oscillator, is used to pump a Light Conversion TOPAS-C optical parametric amplifier (input 3.2 mJ, ~30% conversion efficiency signal+idler). The 500 μJ 1.4 μm signal output is divided with a 50:50 beam-splitter before illuminating two 6 mm clear aperture DAST THz emitters (4-N,N-dimethylamino-4′-N′-methyl-stilbazolium tosylate, Swiss Terahertz). One OPA pump line is passed off a mechanical stepping delay stage which controls the relative time delay between the two pump fields. Additionally, one of the 1.4 μm pump line's polarization is rotated 90 degrees so that the THz emission from the two sources can be recombined and collimated with a wire-grid polarizer (WGP). After recombination, the THz light is filtered with 4 QMC 18 THz low-pass filters (2 after each crystal) to remove any residual optical bleed-through. The THz light is collected, collimated, and focused with a series of off-axis parabolic (OAP) mirrors before being focused onto the sample. The sample is held in a 1 mm path length Suprasil cuvette with a 4.6 mm diameter hole drilled in the front face. Over this hole a 5×5 mm clear aperture, 1 μm thick silicon nitride membrane window (Norcada, QX10500F) is epoxied. This thin membrane minimizes dispersion differences between the THz pump and optical probe fields and also reduces the window response (previous works used 1 mm thick quartz or 300 μm thick diamond windows).

The probe line beam conditioning for single-shot acquisition is unchanged from a previous study [16]. Signal photons are detected on an Andor Zyla 5.5 MP sCMOS

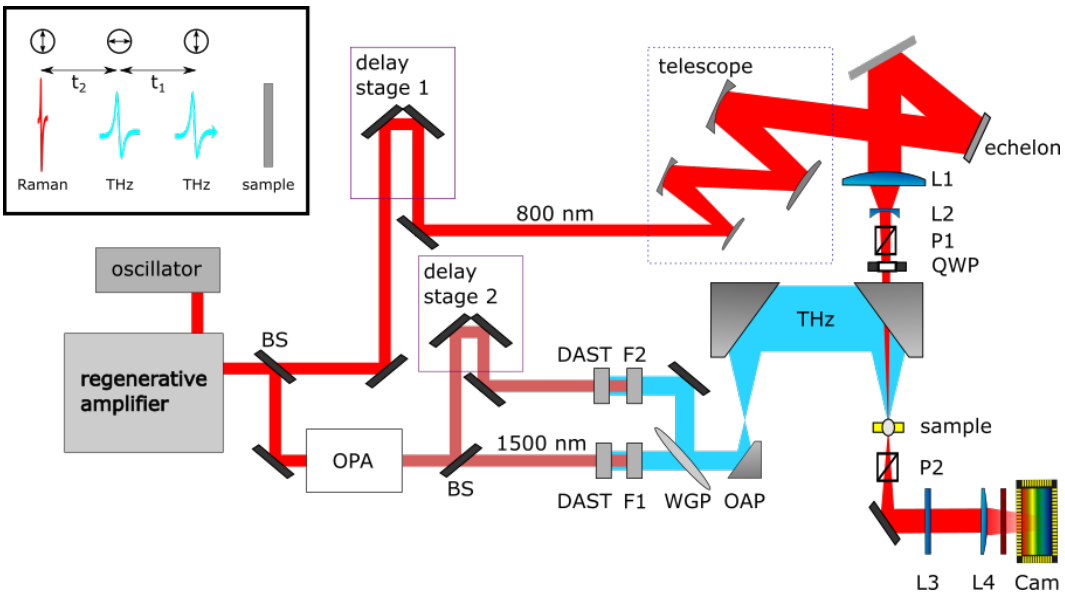

Figure 4.6: The optical path of the 2D-TTR single-shot spectrometer. Seen in an inset are the polarizations of the two THz pump and 800 nm probe fields, and the experimental time definitions.

camera using a pair of crossed 800 nm polarizers with a 10,000:1 extinction ratio (Thorlabs LPVIS050-MP2). Because 2D-TTR uses two orthogonally polarized THz pump fields ($\vec{x}$,$\vec{y}$ polarized in lab coordinates) and crossed probe, signal polarizations ($\vec{x}$,$\vec{y}$ in lab coordinates), the detected signal is sensitive to the anisotropic third order molecular response function $R^{(3)}_{xyxy}(t_1, t_2)$.

All data and experimental parameters were controlled from a MATLAB GUI purpose-built for the experiments. Within the GUI, number of acquisitions per average and number of averages are specified by the user. To capture a data set at a given t_1 time, typical acquisition settings for bromoform are to collect 5 averages with 2,000 shots per average, for a total acquisition time of ~12 seconds, which includes 2 seconds of camera and computational overhead and the 10 seconds of data acquisition. The data set for each average is first collected as a 2000 × 1280 array, with dimensions specified by the number of laser shots captured (e.g., 2000) and the 1280 horizontal binned output pixels from the camera that capture the time-domain molecular response along t_2 at the fixed t_1 time.

Next, we extract the signal from this data array by performing a FFT on each of the 1280 rows of data. Each row corresponds to a single point in time t_2 sampled by the probe pulse. These FFTs must be performed carefully to phase relationship of the two THz fields that produce the signal. To do so, we collect several other pieces of

data while each average is acquired. First, outputs of the two optical choppers that modulate the THz pump fields are recorded on a DAQ card. Second, the camera output signal which confirms the start of a series acquisition is digitized by the same DAQ. From these three trigger signals (chopper A phase, chopper B phase, camera acquisition start), we can measure the signal phase of each average and correct for the phase offset. Doing so ensures that every average at every t_1 time is collected with a single consistent phase, which preserves the overall phase of the 2D signal.

The FFTs are performed by first multiplying each of the 1280 rows of data (each with length 2000 in this example) with an equal length sinusoidal waveform with the measured phase offset and a frequency equal to the difference between the two chopper frequencies (i.e., differential chopping). Multiplication shifts the desired differential signal to the DC position in the frequency domain FFT output. The DC response from all 1280 channels are then saved as a 1×1280 data array for each average, and are co-added until all averages are collected. In essence, this approach creates a software equivalent to the standard digital lock-in amplifier typically used for collection of single channel spectroscopic data.

2D-TTR Sensitivity to IRF

We provide an additional example of the sensitivity of bromoform's 2D-TTR spectrum to the instrument response function, which was first noticed as a result of changing the infrared wavelengths that pump the two THz emitters. Initial 2D-TTR experiments used the two orthogonally polarized signal (1.4 μm) and idler (1.8 μm) outputs of the TOPAS-C OPA were each used to pump one of the DAST crystals. However, we observed that the majority of the idler line's IR power was concentrated in a small ~1 mm diameter point within the larger 8 mm diameter beam. As a result, this concentrated point of power was burning the DAST crystal face. To prevent damage to the emitter crystal, we split the signal beam into two halves, rotated one half's polarization to match the idler polarization, and recorded new 2D-TTR data of bromoform. Dramatic differences in bromoform's time (Fig. 4.7) and frequency (Fig. 4.8) domain response were observed, drawing our attention to the importance of the IRF in 2D-TTR. SF-RDM analysis of the original 1.4/1.8 μm bromoform data yielded similarly excellent agreement between experiment and simulation.

Halogenated methane purification

Bromoform was purchased from Sigma Aldrich. As received the liquid had a orange hue, indicating some degradation and contamination from water. A simple distilla-

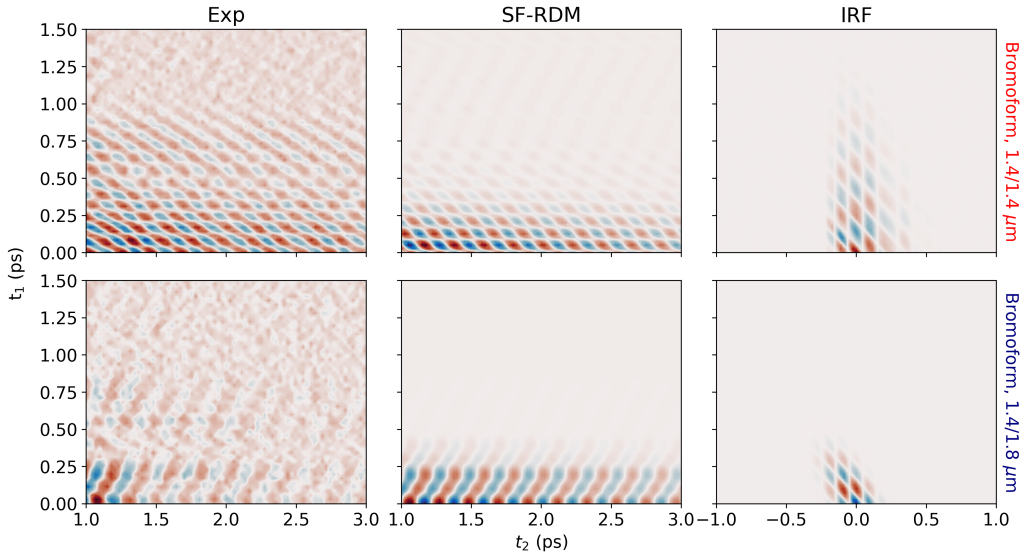

Figure 4.7: Top and bottom rows compare the experimental (Exp) bromoform time-domain data under two different THz pumping regimes. Slight changes to the emitted THz fields result in different time-domain IRFs. SF-RDM models using the THz electric fields that produce each IRF fully reproduce the experimental data.

tion under nitrogen at 150 degree Celsius was performed to purify the bromoform liquid. NMR analysis indicated complete removal of water. The purified sampled was stored in a round-bottom flask with dry sodium sulfate, under argon in a dark refrigerator. Chloroform was purchased from Sigma Aldrich and used as received.

TKE Response of HMs

Terahertz Kerr effect measurements were taken of bromoform and chloroform, and the 2D-TTR response of diamond was measured to gauge the bandwidth of the THz pump fields [14]. As shown in Fig. 4.9, the THz electric field bandwidth is centered at 4 THz. Bromoform's two Raman-active vibrational modes are observed at 4.7 and 6.6 THz, while the Raman-active vibrational mode in chloroform was observed at 7.8 THz. Note that the orientational (low-frequency) response of both liquids was removed prior to taking the FFT, and only the higher frequency spectral content arising from intra-molecular vibrations are seen in Fig. 4.9.

THz field modeling

The frequency domain IRF slices at the eigenmode frequencies for halogenated methanes in this study are highly sensitive to small changes in the THz pump pulse

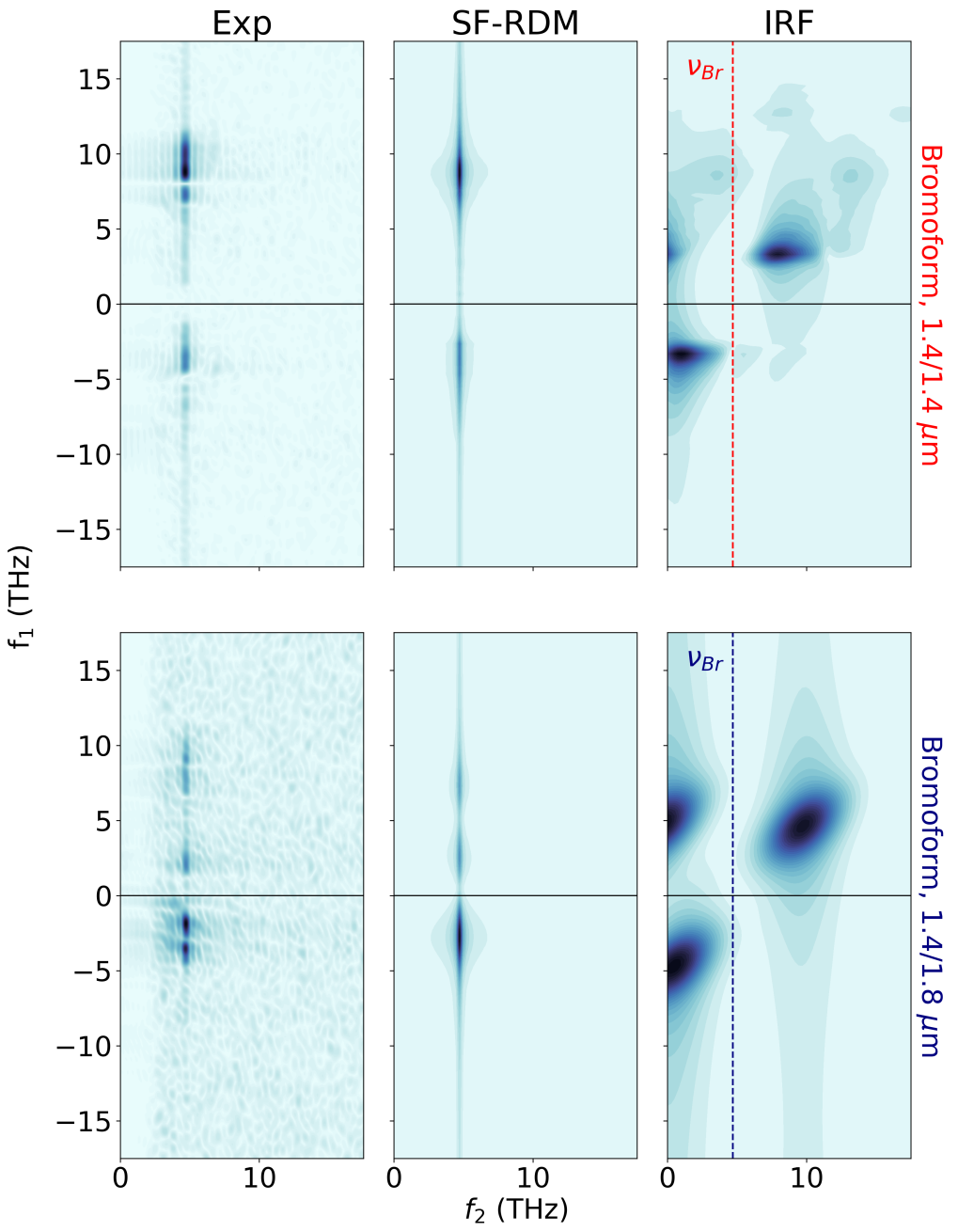

Figure 4.8: Top and bottom rows compare the experimental (Exp) bromoform frequency-domain data under two different THz pumping regimes. Slight changes to the emitted THz fields result in different frequency-domain IRFs. SF-RDM models with the THz electric fields that produce each IRF reproduce the experimental spectra.

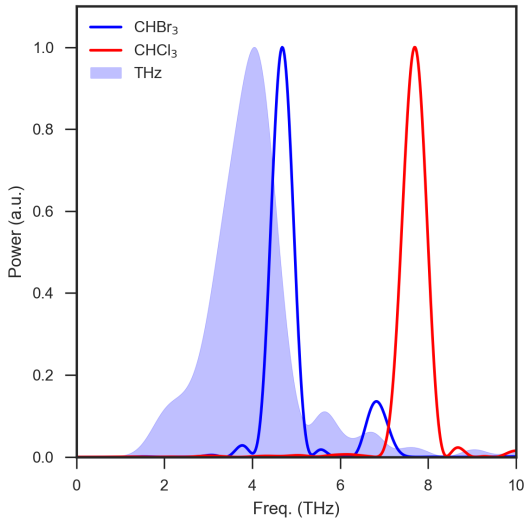

Figure 4.9: Bromoform and chloroform intramolecular vibrational responses are detected in 1D-TKE measurements. The THz bandwidth of the DAST emission as measured in diamond is shown in blue shading.

shapes. This is especially true for bromoform, whose eigenmode frequency intersect a region of very low spectral power in the IRF. Near perfect fits to the experimental TTR spectra of HMs in both the time and frequency domains were obtained by using model THz pulse shapes, which closely resemble the experimental pulse shapes measured in diamond. We believe the use of these model THz pulse shapes is adequate here considering the chromatic nature of the THz focus and the S/N limitations of the diamond TTR spectra (due to the inherently small $\chi^{(3)}$ constant).

The model THz pulse shapes were obtained with the following process. First, the bandwidths of the two THz pulses were optimized to fit both experimental HM TTR slices at eigenmode frequencies of bromoform and chloroform. To avoid overfitting, a simple asymmetric Gaussian functional form was assumed for the bandwidth of the THz pulses to minimize the number of parameters. The time domain IRF is calculated as the product of the THz pulse shapes

$$I(t_1, t_2) = E_1(t_1 + t_2)E_2(t_2)$$

and the Fourier transform of the IRF $\tilde{I}(f_1, f_2)$ is

$$\tilde{I}(f_1, f_2) = \tilde{E_1}(f_1)\tilde{E_2}(f_2 - f_1)$$

where $\tilde{E_1}$ and $\tilde{E_2}$ are the bandwidths of the THz pulses. The frequency domain optimization yields only the amplitude spectra, and a phase spectra is still required to

uniquely determine the time-domain representation. The hybrid input-output phase retrieval algorithm was used with the experimentally measured THz pulse shapes as targets. Convergence was generally obtained within 100 iterations. The resulting model THz pulses accurately reproduce the observed time and frequency domain results for both HMs, as shown in the main text. THz pulse shape measurements in general underestimate the available power at higher THz frequencies due to velocity mismatch between the probe (800 nm) and THz pulses, which further supports the increased power above 4 THz for the model pulse shapes.

SF-RDM model

Sum-frequency pathways were not considered in our previous RDM model Hamiltonian [13–15]:

$$H(t;t_1) = H_0 - M \cdot [E_2(t-t_1) + E_1(t)] \,. \tag{4.3}$$

A new Hamiltonian was constructed here, which accounts for the SF process:

$$H(t;t_1) = H_0 - \Pi \cdot [E_2(t-t_1) + E_1(t)]^2 \,. \tag{4.4}$$

Experimentally, differential chopping of the two THz fields automatically removes the single pulse contributions $\Pi \cdot E_2^2(t-t_1)$ and $\Pi \cdot E_1^2(t)$, so we are left with an effective Hamiltonian of the form:

$$H(t;t_1) = H_0 - \Pi \cdot E_2(t-t_1)E_1(t). \tag{4.5}$$

The time response is computed as described in our previous work [15], but now it corresponds to an SF signal:

$$S(t_2;t_1) = S_{SF}(t_2;t_1) = Tr(\Pi \cdot \rho(t_2;t_1)). \tag{4.6}$$

The complete signal S is obtained when E_1 and E_2 are replaced with the fitted pulse shapes, while the molecular response R when E_1 and E_2 are simple δ-functions. All operators are kept linear and harmonic.

References

[1] Dale Mcmorrow, William T. Lotshaw, and Geraldine A. Kenney-Wallace. "Femtosecond optical Kerr studies on the origin of the nonlinear responses in simple liquids." *IEEE Journal of Quantum Electronics* 24.2 (1988), pp. 443–454.

[2] Minhaeng Cho et al. "Off-resonant transient birefringence in liquids." *Journal of Chemical Physics* 99.4 (1993), p. 2410.

[3] A. Tokmakoff et al. “Two-dimensional Raman spectroscopy of vibrational interactions in liquids.” *Physical Review Letters* 79.14 (1997), pp. 2702–2705.

[4] David A. Blank, Laura J. Kaufman, and Graham R. Fleming. “Fifth-order two-dimensional Raman spectra of CS2 are dominated by third-order cascades.” *Journal of Chemical Physics* 111.7 (1999), pp. 3105–3114.

[5] Kevin J. Kubarych et al. “Diffractive optics-based six-wave mixing: Heterodyne detection of the full chi((5)) tensor of liquid CS2.” *Journal of Chemical Physics* 116.5 (2002), pp. 2016–2042.

[6] Toshiaki Hattori. “Classical theory of two-dimensional time-domain terahertz spectroscopy.” *Journal of Chemical Physics* 133.20 (2010).

[7] Tatsushi Ikeda, Hironobu Ito, and Yoshitaka Tanimura. “Analysis of 2D THz-Raman spectroscopy using a non-Markovian Brownian oscillator model with nonlinear system-bath interactions Analysis of 2D THz-Raman spectroscopy using a non-Markovian Brownian oscillator model with nonlinear system-bath interactions.” *The Journal of Chemical Physics* 212421 (2015), pp. 0–15.

[8] Janne Savolainen, Saima Ahmed, and Peter Hamm. “Two-dimensional Raman-terahertz spectroscopy of water.” *Proceedings of the National Academy of Sciences of the United States of America* 110.51 (2013), pp. 20402–20407.

[9] Andrey Shalit et al. “Terahertz echoes reveal the inhomogeneity of aqueous salt solutions.” *Nature Chemistry* 9.3 (2017), p. 273.

[10] Peter Hamm and Andrey Shalit. “Perspective: Echoes in 2D-Raman-THz spectroscopy.” *The Journal of Chemical Physics* 146.13 (2017), p. 130901.

[11] Gustavo Ciardi et al. “Signatures of intra- and intermolecular vibrational coupling in halogenated liquids revealed by two-dimensional Raman-terahertz spectroscopy.” *Journal of Physical Chemistry Letters* 10.15 (2019), pp. 4463–4468.

[12] Marco A. Allodi, Ian A. Finneran, and Geoffrey A. Blake. “Nonlinear terahertz coherent excitation of vibrational modes of liquids.” *Journal of Chemical Physics* 143.23 (2015), p. 234204.

[13] Ian A. Finneran et al. “Coherent two-dimensional terahertz-terahertz-Raman spectroscopy.” *Proceedings of the National Academy of Sciences* 113.25 (2016), pp. 6857–6861.

[14] Ian A. Finneran et al. “2D THz-THz-Raman photon-echo spectroscopy of molecular vibrations in liquid bromoform.” *Journal of Physical Chemistry Letters* 8.18 (2017), pp. 4640–4644.

[15] Ioan B. Magdău et al. “Interpretation of the THz-THz-Raman spectrum of bromoform.” *The Journal of Physical Chemistry A* (2019), acs.jpca.9b05165.

[16] Griffin Mead et al. “An echelon-based single shot optical and terahertz Kerr effect spectrometer.” *Review of Scientific Instruments* 90.5 (2019), p. 053107.

[17] Sebastian Maehrlein et al. “Terahertz sum-frequency excitation of a Raman-active phonon.” *Physical Review Letters* 119.12 (2017), pp. 1–6.

[18] Dominik M. Juraschek and Sebastian F. Maehrlein. “Sum-frequency ionic Raman scattering.” *Physical Review B* 97.17 (2018), pp. 1–8.

[19] Vladislav Yu. Shishkov et al. “Enhancement of the Raman effect by infrared pumping.” *Physical Review Letters* 122.15 (2019), p. 153905.

[20] David Sidler and Peter Hamm. “Feynman diagram description of 2D-Raman-THz spectroscopy applied to water.” *Journal of Chemical Physics* 150.4 (2019).

Chapter 5

MAPPING $LINBO_3$ PHONON-POLARITON NONLINEARITIES WITH 2D THZ-THZ-RAMAN SPECTROSCOPY

Adapted with permission from:

Haw-Wei Lin, Griffin Mead, Geoffrey A. Blake. "Mapping $LiNbO_3$ phonon-polariton nonlinearities with 2D THz-THz-Raman spectroscopy." *Physical Review Letters*, 129 (2020), pp. 207401. DOI: 10.1103/PhysRevLett.129.207401

5.1 Abstract

Two-dimensional terahertz-terahertz-Raman spectroscopy (2D-TTR) can provide insight into the anharmonicities of low-energy phonon modes—knowledge of which can help develop coherent control strategies of material properties. Measurements on $LiNbO_3$ reveal THz and Raman nonlinear transitions between the $E(TO_1)$ and $E(TO_3)$ phonon-polaritons. Distinct coherence pathways are observed with different THz polarizations. The observed pathways suggest that the origin of the third-order nonlinear responses is due to mechanical anharmonicities, as opposed to electronic anharmonicities. Further, we confirm that the $E(TO_1)$ and $E(TO_3)$ phonon-polaritons are excited through resonant one-photon THz excitation.

5.2 Main text

Coherent control of lattice dynamics using ultrafast optical techniques can alter macroscopic properties of materials. Notable demonstrations include driving reversals of ferrolectric polarization [1], initiating magnetic phase transitions [2], and enhancing superconductivity [3]. However, optical fields can also produce parasitic electronic excitations within materials [4] and are fundamentally limited from phase-sensitive access to THz-energy phonon modes that are coupled to bulk material properties [5–9].

Recent developments of intense ultrafast terahertz (THz) sources present an exciting, if under-explored, alternative to optical fields for coherent control experiments [4, 7, 10]. With THz fields, it becomes possible to resonantly drive specific phonon modes with phase sensitivity and with no parasitic excitations. Unlike optical pulses, THz fields also offer an extra dimension of control since phonon excitations can

proceed through both dipole- and polarizability-mediated transitions. Additionally, the fast-paced development of pulse shaping technologies [11–13] may present opportunities for creating tailored THz pulses which precisely manipulate specific material properties using knowledge of mechanical and electronic anharmonicities.

To reach this future degree of control over material properties, it is essential to be able to observe and interpret the multitude of different linear and nonlinear excitation pathways that occur within a material when pumped with an intense, broadband THz field. These kinds of "mapping" experiments reveal information on a material's potential energy landscape, excitation pathways, and dominant anharmonicities, thus laying the foundation for future mode-selective coherent control experiments and applications.

Lithium niobate ($LiNbO_3$) is a fundamental material in nonlinear optics due to its large ferroelectric response and nonlinear susceptibility [14, 15]. Phonon-polaritons (PhP) in $LiNbO_3$ have been linked to orders of magnitude enhancements of the second-order susceptibility in the low THz frequency regime [5]. $LiNbO_3$ is also notably used for generating intense THz pulses using velocity-matched tilted-pulse-fronts [16–20]. The unique properties and numerous applications of $LiNbO_3$ suggest it as an ideal model candidate for developing techniques which can map out phonon mode anharmonicities.

In this letter, we demonstrate the use of two-dimensional terahertz-terahertz-Raman (2D-TTR) spectroscopy to characterize the potential energy surface (PES) of E-symmetry phonon modes in x-cut congruent $LiNbO_3$. The excitation mechanism, nonlinear phonon-phonon couplings, and the primary source of anharmonicity for the E-symmetry phonon modes are directly determined from the third-order nonlinear response.

2D-TTR spectroscopy

While time intensive, multidimensional spectroscopy is a powerful tool for disentangling overlapping spectral features, determining the timescales of the underlying processes, and revealing couplings between spectral modes [24–27]. Hybrid THz-Raman third-order spectroscopies have been suggested as ideal tools for characterizing solid state PESs [6, 24]. We employ 2D-TTR spectroscopy, a multidimensional extension of THz Kerr effect (TKE) spectroscopy in which an additional time delay t_1 is introduced between two THz pump pulses [25, 28], to study $LiNbO_3$.

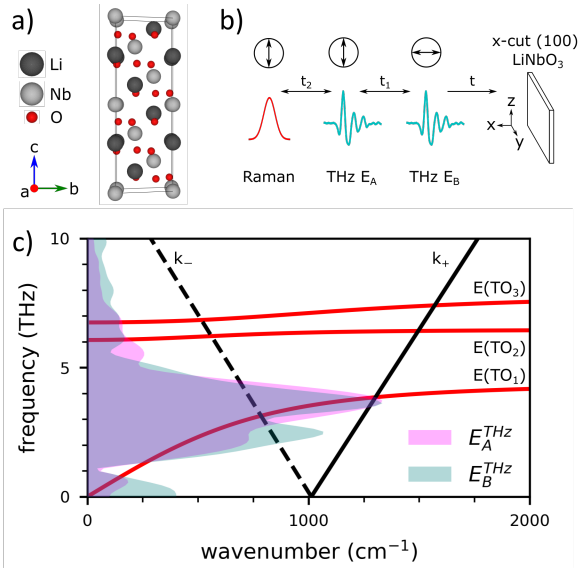

Figure 5.1: Experimental details. (a) $LiNbO_3$ crystal structure in the hexagonal unit cell [21, 22]. (b) Schematic of the 2D-TTR experiment, pulse sequence, and time definitions. The polarization of each pulse is indicated in the circles. Coordinates $\{x, y, z\}$ refer to the crystal axes of x-cut $LiNbO_3$, where x and z coincide with unit cell vectors a and c, and y is orthogonal to x and z. (c) Red: PhP dispersion curve for E-symmetry phonon modes [23]. Black: wavevector matching condition of the 800 nm probe for forward (k_+, solid) and backward (k_-, dashed) propagating PhPs [19]. The shaded regions show the THz bandwidth of E_A^{THz} and E_B^{THz}.

The third-order nonlinear polarization induced by the 2D-TTR pulse sequence (Fig. 5.1b) is given as

$$P^{(3)}(t) = E_{probe}(t) \iint dt_1 dt_2 R^{(3)}(t_1, t_2) \\ E_A^{THz}(t - t_2) E_B^{THz}(t - t_1 - t_2). \tag{5.1}$$

The third-order response function $R^{(3)}(t_1, t_2)$ contains both resonant one-photon absorption (1PA)

$$tr\langle \alpha(t_1 + t_2)[\mu(t_1), [\mu(0), \rho]]\rangle$$

and sum-frequency two-photon absorption (2PA)

$$tr\langle \alpha(t_1 + t_2)[\alpha(0), \rho]\rangle$$

. THz excitation pathways, where μ and α are the transition dipole and polarizability operators, respectively, and ρ is the equilibrium density matrix [25]. Both E- and A_1-symmetry phonons in $LiNbO_3$ (*R3c* space group) are Raman- and IR-active and

can be simultaneously excited with broadband THz pulses. However, the cross-polarized Raman probe setup is selectively sensitive to E-symmetry phonons (see SI for details). The wavevector matching condition for the E-symmetry PhPs and the available THz pump bandwidths are shown in Fig. 5.1c, highlighting the broadband pump pulses used have sufficient bandwidth to induce either 1PA or 2PA excitations up to the E(TO_3) mode.

While the optical excitation mechanism of PhPs in $LiNbO_3$ is quite well-understood [16, 19, 29], the excitation mechanism of PhPs with THz frequency pulses remains unclear. The forward-propagating E(TO_1) PhP has been studied with TKE spectroscopy [17] and 2D-TTR spectroscopy with two parallel-polarization THz pulses [6]. In this 2D-TTR setup, the single-pump, lower-order signals are also recorded, which are significantly more intense than the double-pump signals that strongly depend on excitation mechanism, phonon-phonon couplings, and anharmonicity. While these data are well-suited for coupled-equations of motion models for the phonon modes, the nonlinear signatures of interest can be obstructed in 2D frequency space and may require significant THz field strengths to be observable. This is the case in $LiNbO_3$, where 2D spectra modelling do not conclusively determine whether the excitation of the E(TO_1) PhP proceeds through a 2PA or anharmonic 1PA mechanism [6]. Higher frequency PhPs that are observed with optical Raman excitations [19] also remained unexplored with THz excitations due to the limited THz bandwidth available in previous TKE and 2D-TTR experimental studies of $LiNbO_3$.

In contrast to earlier 2D-TTR experiments on $LiNbO_3$ [6, 24], we utilized orthogonal THz pump pulses and careful differential chopping to rigorously remove single-pump and second-order contributions, which are difficult to remove in 1D-TKE spectroscopy and do not provide definitive information on excitation mechanism and anharmonic phonon-phonon couplings. This is crucial for studying phonon modes that are both Raman- and IR-active, where the large number of possible 1D excitation pathways can easily overwhelm weaker nonlinear features of the PES and overcrowd the 2D spectra. Two separate THz emitters are used for THz generation to prevent emitter dynamics from contaminating the 2D-TTR spectra. Further, by varying the crystal orientation and the time ordering of the THz pump pulses, four independent elements of $R^{(3)}$ are measured with 2D-TTR.

$LiNbO_3$ has also been studied by 2D-THz spectroscopy, the direct analog of 2D-IR in the THz frequency range [30]. The emitted signal in 2D-THz are attributed

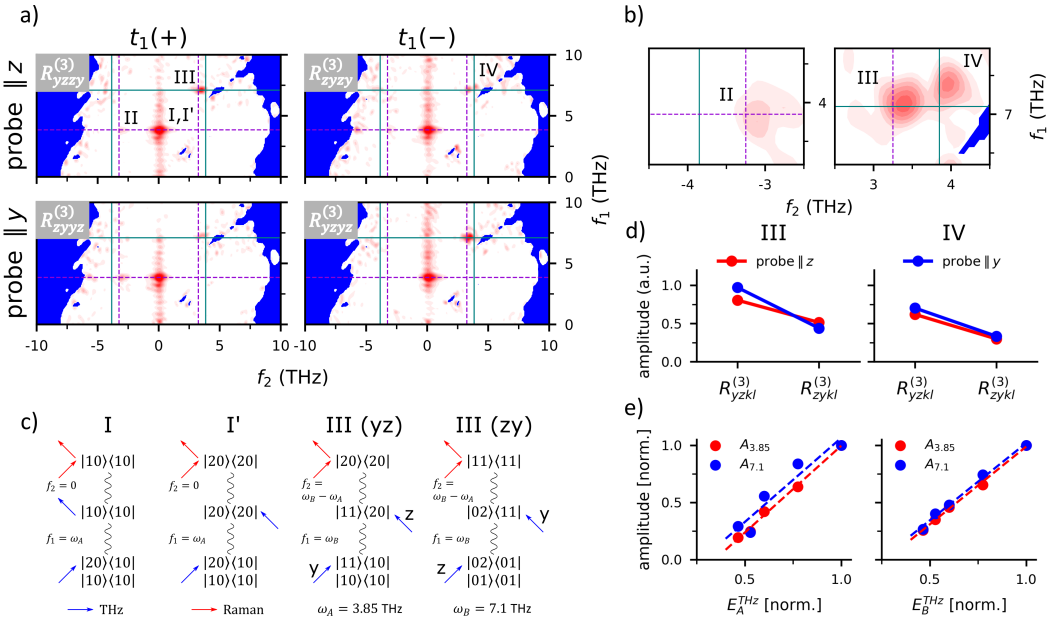

Figure 5.2: Analysis of the 2D-TTR spectra of $LiNbO_3$. (a) 2D-TTR spectra in the frequency domain for four pump-probe polarization configurations, taken from the combination of two crystal orientations and two THz polarization orderings (positive and negative t_1 quadrants). The spectra have been deconvolved by the IRF to reveal true intensity and frequency positions. Guiding lines are provided at f_1 = 3.85 THz (violet), f_1 = 7.1 THz (teal), f_2 = ±3.25 THz (violet) and f_2 = ±3.85 THz (teal). (b) Zoom-in of peaks II to IV for polarization $R^{(3)}_{zyzy}$. (c) Select Feynman pathways for the observed nonlinear peaks (I, I') and III. Depending on the THz polarizations, III (yz) or III (zy) is selectively observed. See SI for full assignment. (d) THz polarization dependence of the FT amplitude of peaks III and IV. (e) THz field strength dependence of the E(TO_1) ($A_{3.85}$) and E(TO_3) ($A_{7.1}$) features along f_1. Best linear fits are shown as dashed lines.

to THz field-induced interband-tunnelling of electrons into the conduction band. Due to the moderate THz frequency (< 2 THz) used in the 2D-THz experiment, near DC nonlinear effects are dominant and anharmonic phonon dynamics remain unexplored. Our experiments employ higher field strength (> 1 MV/cm) and bandwidth, which enables exploration of PhP modes up to ~ 9 THz to characterize the excitation pathways and nonlinearities.

Resonant excitation of E(TO_1) and E(TO_3)

The time domain 2D-TTR spectra of 0.5 mm thick x-cut $LiNbO_3$ measured at $E_{probe} \parallel z$ and $E_{probe} \parallel y$ are provided in the SI. Note that the coordinates $\{x, y, z\}$ refer to the crystal axes of x-cut $LiNbO_3$ throughout this letter. The response exhibits

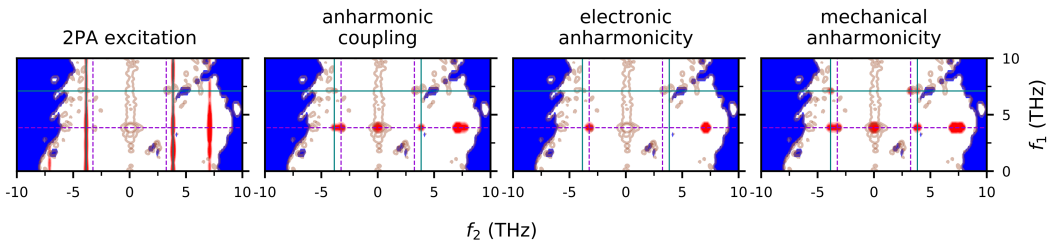

Figure 5.3: Third-order models based on different excitation mechanisms and sources of anharmonicity. Identical guiding lines are added. For reference, the overlayed contours depict the $R^{(3)}_{zyzy}$ experimental spectra.

an oscillatory behavior along t_1 and a damped exponential along t_2 with oscillatory features near $t_2 = 0$. A prolonged t_1 response extending far outside the THz field-overlap region (roughly $-0.5 \leq t_1 \leq 0.5$ ps) provides clear evidence of long-lived dynamics after the first THz pulse, indicating that the 1PA contribution to $R^{(3)}$ is dominant compared to that from 2PA pathways. The 2PA contribution to 2D-TTR only exists in the THz field overlap region near $t_1 = 0$ (see SI for details); whereas, the extent of the 1PA pathway is determined by the dephasing time of the coherent state, which typically extends several picoseconds outside the field overlap region.

The different nonlinear contributions to the time domain signal can be separated in 2D frequency space through a 2D fast Fourier transform (2D-FFT). To extract the nuclear components of $R^{(3)}$, the region $-0.75 \leq t_1 \leq 0.75$ ps is removed prior to 2D-FFT to avoid coherent artifacts present in the field-overlap region. After 2D-FFT, the spectra is deconvolved by the instrument response function (IRF) [25, 31]. As described in equation (1), the measured spectra are a convolution of $R^{(3)}$ with the structured THz pulses in the time domain. The IRF is experimentally measured using the third-order electronic response of 100 μm GaP [25]. Applying the convolution theorem, the deconvolution process becomes a simple division of the 2D-FFT spectra of $LiNbO_3$ by the IRF spectra in the frequency domain. The deconvolved 2D-FFT results for all four polarization configurations are shown in Fig. 5.2a. The regions of low deconvolution confidence (less than 5% IRF amplitude) are marked with solid blue. Tensor notation $R^{(3)}_{ijkl}$ is used to denote the pump-probe polarizations, in which $ijkl$ corresponds to the polarization of the first and second THz pulse, the probe pulse, and the detected third-order polarization, respectively.

Four main 2D spectral features, labelled I to IV, are observed. The pairs of spectra with identical THz polarization ($R^{(3)}_{yzzy}$ and $R^{(3)}_{yzyz}$; $R^{(3)}_{zyzy}$ and $R^{(3)}_{zyyz}$) show strong similarities in peak positions and intensity. This is due to selection rules for y and

z polarized THz pulses and will be discussed in detail below. A dominant peak (I,I') at $(f_1, f_2) = (3.85, 0)$ THz is apparent in the spectra, corresponding to the main features along t_1 ($E(TO_1)$ damped harmonic oscillation) and t_2 (exponential decay). Two weaker peaks (II and III) are observed at $(f_1, f_2) = (3.85, \sim -3.25)$ and $(\sim 7.1, \sim 3.25)$. An additional peak (IV) can be observed near peak III at $(\sim 7.1, \sim 3.85)$ for $R^{(3)}_{zyzy}$ and $R^{(3)}_{zyyz}$.

The ~ 7.1 THz features correspond to the $E(TO_3)$ PhP. Energy conservation and momentum considerations suggest that the forward-propagating PhP is excited by the THz pump pulses. This feature has not been observed in previous TKE studies of $LiNbO_3$ [6, 17] likely due to THz bandwidth limitations (< 5 THz). While the $E(TO_2)$ phonon is within the THz bandwidth, due to the order-of-magnitude lower transition dipole strength compared to $E(TO_1)$ and $E(TO_3)$ [23], no associated dynamics are observed. With $f_1 = 7.1$ assigned to $E(TO_3)$ PhP, it is natural to assign $f_2 = \pm 3.25$ to the difference frequency of $E(TO_1)$ and $E(TO_3)$ PhPs. The field strength dependence of the $f_1 = 3.85$ THz and $f_1 = 7.1$ THz features are measured (Fig. 5.2e), and both peaks show linear dependence with respect to the field strength of THz pump A and B, i.e., $S_{3.85}, S_{7.1} \propto E_A^{THz} \cdot E_B^{THz}$, confirming that the observed signals are third-order in nature. Thus, the linear power scaling and the extended dynamics along t_1 provide direct evidence that both $E(TO_1)$ and $E(TO_3)$ PhPs originate from resonant 1PA THz excitations.

Polarization dependence of nonlinear transitions

To analyze the intensity changes observed with different THz polarizations, we perform a Feynman pathway analysis to examine the quantum state of the system after each field interaction. Unlike 2D-IR spectroscopy, whose pathways only involve one-quanta transitions, 2D-TTR pathways must include a nonlinear transition due to its three-pulse sequence. The lowest-order pathways consist of two one-quanta transitions and one zero- or two-quanta transition [26]. Consequently, the peak positions can not only arise at resonant frequencies of the vibrational modes, but also at zero, second-harmonic, sum- and difference-frequencies. Feynman pathway assignments for peaks I and III are provided in Fig. 5.2c (full assignment in SI). The double-sided Feynman diagram notation $|n_1 n_3\rangle \langle n_1 n_3|$ is used to denote the density matrix of the system, where n_1 and n_3 are the number of quanta in $E(TO_1)$ and $E(TO_3)$, respectively. Field-induced excitation and de-excitation are represented by inward and outward arrows. Further, THz transitions are only allowed if the momentum of the THz photon maps onto the PhP dispersion curves. We confirmed

that conservation of momentum is preserved in the Feynman pathways presented (see SI for details on momentum conservation in nonlinear transitions).

Pathway I involves two one-quanta THz transitions and a final zero-quanta Raman transition. Symmetry analysis shows that the $|00\rangle \rightarrow |10\rangle$ transition is symmetry-forbidden for $E^{THz} \parallel z$; whereas, the transition $|10\rangle \rightarrow |20\rangle$ is symmetry-allowed for both $E^{THz} \parallel z$ and $E^{THz} \parallel y$. Thus, the proposed Feynman pathway I starts from the $|10\rangle\langle 10|$ population state and is symmetry-allowed for both THz polarization ordering $ij = yz$ and zy. The low energy of the phonon modes compared to thermal energy $k\mathrm{T} = 6.2$ THz at room temperature makes the excited population state available.

Next, we examine peaks II-IV, whose intensities are strongly dependent on THz polarization. For example, the FT amplitude is larger in THz polarization yz than zy for peaks III and IV (Fig. 5.2d). Due to selection rules for E-symmetry phonons, the two THz polarizations yz and zy result in distinct symmetry-allowed Feynman pathways (Fig. 5.2c for peak III). Notably, the starting state is different for the two polarizations. Considering only thermodynamic effects on the starting state population, the Boltzmann factor $e^{-(\omega_1-\omega_2)/k\mathrm{T}}$ predicts for peaks III and IV a 1.7-fold and 1.9-fold increase in amplitude for polarization yz over zy, which is consistent with the experiment for both probe polarization. Follow-up measurements of low temperature $LiNbO_3$ 2D-TTR spectra would be highly informative for the Feynman pathway assignments.

Origin of anharmonicity

A third-order 2D-TTR signal must involve a nonlinear transition in the resonant 1PA pathway. Consequently, 2D-TTR spectroscopy is highly sensitive to the anharmonicities present in the system, because the allowed nonlinear zero- or two-quanta transitions depend on the type of anharmonicity. We implement the anharmonic coupling model proposed by Sidler and coworkers [26], which considers resonant 1PA pathways induced via electronic and mechanical anharmonicities. Electronic anharmonicity refers to the nonlinear contributions to the transition dipole and polarizability operators of the vibrational mode [27]. For two normal modes $E(TO_1)$ and $E(TO_3)$ with coordinates $\hat{q}_{E_1}$ and $\hat{q}_{E_3}$, the lowest order nonlinear dipole operator can be written as

$$\hat{\mu} \approx \mu^{(0)}\hat{q}_{E_1} + \mu^{(1)}\hat{q}_{E_1}\hat{q}_{E_3}$$

. Alternatively, mechanical anharmonicity refers to perturbations to the Hamiltonian of the system, which includes both PES anharmonicity of the individual modes ($\hat{H}^{(1)}_{E_1}$ and $\hat{H}^{(1)}_{E_3}$) as well as cross-coupling terms between modes ($\hat{H}^{(1)}_{E_1E_3}$). Here, we considered an anharmonic cross-coupling term of the form

$$\hat{H}^{(1)}_{AB} = \lambda_{AAB}\hat{q}^2_A\hat{q}_B$$

with sum over all modes $A, B = \{\mathrm{E(TO_1)}, \mathrm{E(TO_3)}\}$.

For completeness, a model that considers the 2PA excitation pathway is also implemented (details in SI). As a first approximation, we assign equal intensity to all possible transitions. After applying convolution with the experimental IRF, the results are shown in Fig. 5.3. Critically, these models are constructed to include only third-order signals that involve both pump electric fields to account for the experimental differential chopping of 2D-TTR spectroscopy. One major benefit of selectively measuring the third-order 2D-TTR signal is the distinctness between signals from 2PA and 1PA pathways. The 2PA excitation pathway produces characteristic "streaking" patterns along f_1 [25], while 1PA pathways produce peaks at unique frequency positions [26]. Consistent with the Feynman pathway analysis presented above, the 2D-TTR spectra resemble much more closely to the 1PA anharmonic coupling model. By examining the individual sources of anharmonicity, it is clear that peaks I, III, IV can only be induced by mechanical anharmonicity, while peak II can be induced by both mechanical and electronic anharmonicity. These models strongly suggest that the observed 2D features are primarily induced via mechanical anharmonicity. A few additional peaks predicted by the mechanical anharmonicity model are not observed experimentally possibly due to limited THz power at the frequencies required for the nonlinear transition. For instance, the peaks at $(3.85, \pm 3.85)$ involve nonlinear zero- or two-quanta THz transitions of the $\mathrm{E(TO_1)}$ mode, which require significant power at near DC or $\sim$ 8 THz.

Conclusion

We demonstrate that 2D-TTR spectroscopy can provide detailed information on the excitation mechanism, nonlinear phonon-phonon couplings, and sources of anharmonicity in phonon-polariton (PhP) dynamics of x-cut $LiNbO_3$. The wider bandwidths employed in this study allow investigation of both $\mathrm{E(TO_1)}$ and $\mathrm{E(TO_3)}$ PhPs. The selective measurement of the third-order response removes the single-pump contributions that dominate the 1D-TKE response and focuses on 2D signatures that are highly sensitive to the anharmonicity of the potential energy landscape. Feynman

pathway analysis reveals THz and Raman nonlinear transitions between the E(TO_1) and E(TO_3) PhPs. We further determined that the E(TO_1) and E(TO_3) phonon-polaritons are excited through resonant 1PA THz excitations. Distinct Feynman coherent pathways are observed for different THz polarizations due to THz selection rules. 2PA excitation and 1PA anharmonic coupling models are constructed for third-order double-pumped pathways. The measured 2D-TTR spectra is most consistent with 1PA anharmonic coupling model induced via mechanical anharmonicity as opposed to electronic anharmonicity. These findings provide an important foundation for future coherent control applications. A key demonstration of coherent control of vibrational states is the selective transfer of population [32–34]. The $|01\rangle \rightarrow |10\rangle$ nonlinear transition revealed in this work could be exploited with two THz pulses with tailored phase and bandwidth to achieve efficient population transfer between E(TO_1) and E(TO_3).

5.3 Supplemental information

Experiment

2D-TTR spectroscopy is in the family of 2D hybrid nonlinear THz spectroscopies that employ two THz pulses and one Raman pulse. The pulse sequence of 2D-TTR is provided in the main text. Positive t_1 is defined where E_B^{THz} arrives at the sample before E_A^{THz}. Our 2D-TTR spectrometer has been described in detail in previous publications [25, 28]. Briefly, a 1 kHz regenerative amplifier (Coherent Legend Elite) is used to pump an optical parametric amplifier (Light Conversion TOPAS-C) to create 1.4 μm pulses that pump a DAST emitter (E_A^{THz}) and a DSTMS emitter (E_B^{THz}). The two orthogonal THz pulses are combined using a wiregrid polarizer. Precise spatial overlap of the two THz foci is achieved by direct imaging of the THz focus on a 1 mm ZnTe crystal with a sCMOS camera (ANDOR Zyla 5.5). The THz spot sizes are characterized with the same imaging method to be $1/e^2 \sim 160 - 180$ μm. The THz pulse shapes and bandwidths are shown in SI Fig. 5.4a. The experimental instrument response function (IRF) is measured with the third-order electronic response of 100 μm GaP. The IRF in the frequency domain is shown in SI Fig. 5.4b.

In this work, the conventional stage-scan method is used to measure the 2D-TTR spectra. While the single-shot setup provides a significant speed-up over the strictly colinear method, the dispersed probe beam creates a wide distribution of probe wavevectors that in turn, significantly complicates the phonon-polariton wavevector phase-matching conditions in crystalline $LiNbO_3$. The 2D-TTR spectra is measured

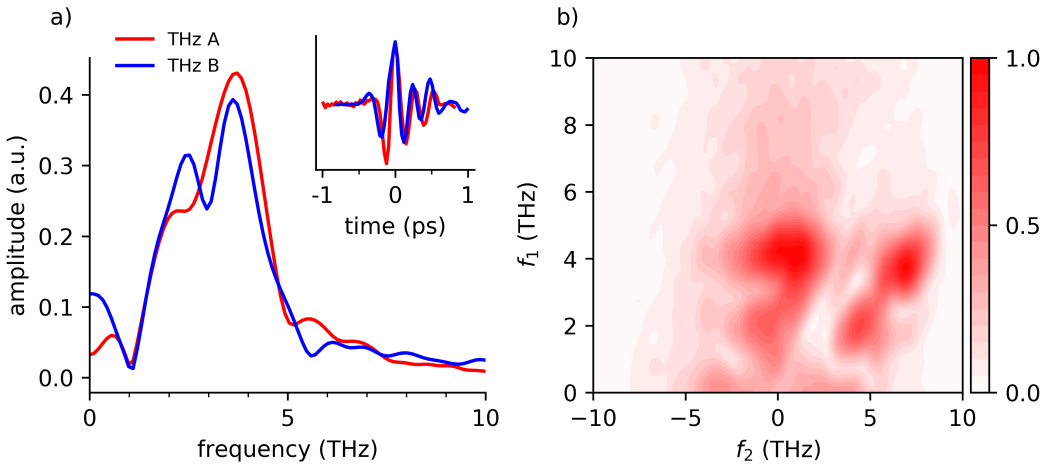

Figure 5.4: Characterization of the THz pulse shapes and instrument response function. (a) Bandwidths of the two THz pump pulses in 2D-TTR. The time domain pulse shapes are shown in the inset. (b) Instrument response function (IRF) of 2D-TTR in 2D frequency space.

by scanning the t_2 axis at discrete t_1 times. The t_1 axis is sampled at 30 fs (Nyquist frequency of 17 THz). The THz beam path is enclosed and purged with N_2 gas for at least 30 minutes to eliminate water vapor prior to data collection. A differential chopping scheme efficiently suppresses single-pump contributions. The two THz pump pulses are modulated by optical choppers at 1/2 and 1/3 of the laser repetition rate, respectively. The 2D-TTR signal is selectively detected at the difference frequency by a lock-in amplifier (Stanford Research Systems SR830) and digitized by a NI DAQ card. All 2D-TTR spectra measured span 6 ps along t_1 (-3 to 3 ps) and $\sim$ 7 ps along t_2. The averaging time was approximately 6 hours for each 2D data set. THz field strength dependence measurements are individually averaged for 40 minutes each.

10 mm by 10 mm wide, 0.5 mm thick, high-purity, two-side optical-quality, x-cut single crystal congruent $LiNbO_3$ samples (MTI corporation, growth method: CZ) are used as purchased. Sample positions are adjusted with custom machined mounts and a motorized linear stage (Newport MFA-PPD) to ensure that the front surface of the sample is positioned consistently. In the 2D-TTR experiments, the THz pump and probe polarizations are kept constant. In order to change the polarization configuration, the crystal mount is rotated to align the y or z crystalline axis to the probe polarization. Due to the inherent strong birefringence of $LiNbO_3$, precise alignment of the crystal orientation to the probe polarization is achieved by minimizing the

probe photon count through the crossed-polarizer setup. The crystalline axes of the $LiNbO_3$ samples are assigned from back-scattering polarized Raman spectroscopy [14] (micro-Raman InVia).

Symmetry-selectivity of the probing scheme

Both A_1- and E-symmetry phonon modes may be excited by the broadband THz pulses used in 2D-TTR spectroscopy. However, the cross-polarized 800 nm Raman probe requires the incoming and scattering light to be perpendicularly polarized. Thus, it is only sensitive to the off-diagonal elements of the Raman tensor. The Raman tensors for A_1- and E-symmetry phonon modes are [14]

$$A_1(z) = \begin{pmatrix} a & 0 & 0 \\ 0 & a & 0 \\ 0 & 0 & b \end{pmatrix}, \quad E(y) = \begin{pmatrix} c & 0 & 0 \\ 0 & -c & d \\ 0 & d & 0 \end{pmatrix}, \quad E(-x) = \begin{pmatrix} 0 & -c & -d \\ -c & 0 & 0 \\ -d & 0 & 0 \end{pmatrix}$$

. As a result, the 2D-TTR setup in this work is only sensitive to pathways whose final transition involves the E-symmetry phonon modes in $LiNbO_3$.

2PA excitation model

The 2PA model is adapted from our previous publication [25]. As described in the main text, the third-order nonlinear polarization measured in 2D-TTR is

$$P^{(3)}(t) = E_{probe}(t) \iint dt_1 dt_2 \, R^{(3)}(t_1, t_2) \cdot E_A^{THz}(t - t_2) \cdot E_B^{THz}(t - t_1 - t_2) \quad (5.2)$$

which is the convolution between the IRF and the third-order response function $R^{(3)}(t_1, t_2)$. The sum-frequency THz 2PA pathway is given as

$$tr\langle \alpha(t_1 + t_2)[\alpha(0), \rho] \rangle$$

. The first polarizability interaction is driven by the combination of the two THz pump fields, which has the form

$$\alpha(t; t_1) \propto \Pi \cdot [E_2(t - t_1) + E_1(t)]^2$$

. Through the implementation of differential chopping, the single-pump terms

$$\Pi \cdot E_2(t - t_1)^2$$

and

$$\Pi \cdot E_1(t)^2$$

are removed. Thus, the only contributing term is

$$\Pi \cdot E_2(t - t_1)E_1(t)$$

. While this term has the same field strength dependence as the resonant 1PA pathway, due to the instantaneous nature of the polarizability operator, the 2PA term is non-zero only if the electric fields E_1 and E_2 are overlap in time. Thus, the 2PA third-order response function $R^{(3)}(t_1, t_2)$ is a delta-function along t_1, which produces the characteristic "streaking" patterns along f_1 after 2D-FFT. Following 2PA excitation of either E(TO_1) or E(TO_3) PhPs, the density of states would be either $|10\rangle\langle 00|$ or $|01\rangle\langle 00|$. These coherent states oscillate at the frequency of the PhP mode at 3.85 or 7.1 THz, resulting in damped oscillatory responses along t_2. While the third-order response function do not have distinct features along f_1, peak-like features can emerge in the experimental spectra due to convolution with the IRF, as shown in equation 1. This highlights the need to account for the complex-structured IRF when multi-cycle THz pulses are used.

2D-TTR time domain spectra

The time domain 2D-TTR spectra of x-cut $LiNbO_3$ at two crystal orientations are shown in SI Fig. 5.5a. Because the true 2D signal can only occur after both THz interactions, a dogleg feature is observed in the time domain, where the signal begins at $t_2 = -t_1$ in the negative t_1 quadrant. The deskewing transformation

$$(t_2', t_1') = (t_2 + t_1, -t_1)$$

is applied to the negative t_1 quadrant prior to 2D-FFT analysis to ensure that each physical process is represented by a single peak [35]. This corrects the difference in time definition in the positive and negative t_1 quadrants shown in SI Fig. 5.5b.

Positive and negative t_1 quadrants have distinct THz polarization ordering due to the orthogonal THz pulses used in this work. The four polarization configurations measured are shown in SI Fig. 5.5b. For example, consider the positive t_1 quadrant in the probe $\parallel y$ spectra. The probe and analyzing polarizer polarizations are y- and z-polarized, respectively. In the positive t_1 quadrant, E_B^{THz} (z-polarized) arrives at the sample before E_A^{THz} (y-polarized). Thus, the element $R^{(3)}_{zyyz}$ is measured in this quadrant.

Feynman pathway analysis

SI Fig. 5.6 details the complete Feynman pathway analysis for the four 2D features observed [36]. For peaks II, III, and IV, distinct Feynman pathways are assigned

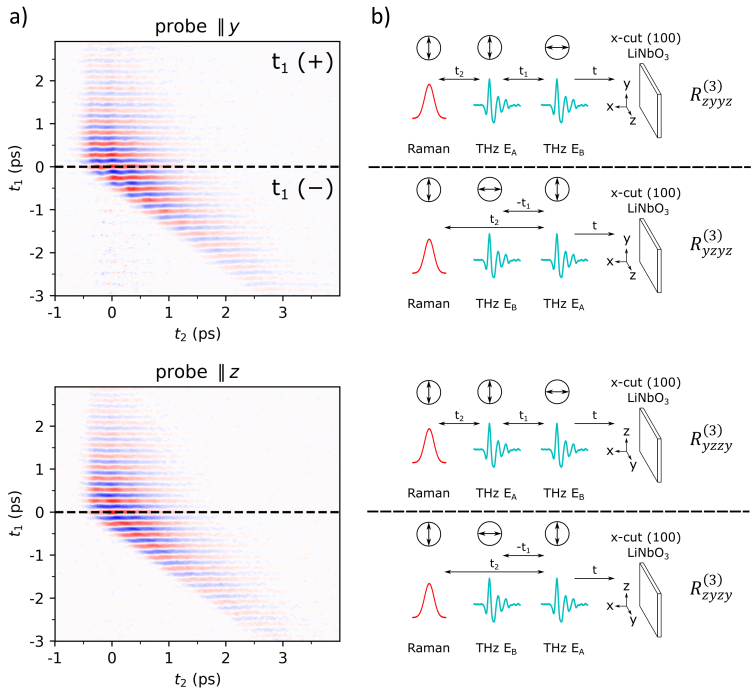

Figure 5.5: Time orderings and polarization configurations of 2D-TTR spectroscopy. (a) Time domain 2D-TTR spectra for two crystal orientations of x-cut $LiNbO_3$. (b) Polarization configurations, crystal orientation, and third-order element measured by each quadrant of the 2D-TTR spectra. Coordinates $\{x, y, z\}$ refer to the crystal axes of x-cut $LiNbO_3$, where x and z coincide with unit cell vectors a and c, and y is orthogonal to x and z.

for different THz polarization. As described in the main text, the starting phonon population states are different due to the selection rules of E-symmetry phonon modes. The required THz polarization ordering is labelled in parenthesis. Peaks I and I' are two pathways that both contribute to the peak at $(f_1, f_2) = (3.85, 0)$ THz. Because these Feynman pathways only involve $E(TO_1)$ transitions, they are symmetry-allowed for both yz and zy THz polarization orderings.

THz field strength dependence of the 2D-TTR signal

To confirm that the signal measured is the desired third-order response, THz field strength dependence of the 2D-TTR signal is measured for t_1 slices at $t_2 = 0$, as shown in SI Fig. 5.7. The time domain traces are shown in SI Fig. 5.7a and e, and the corresponding Fourier transforms are shown in SI Fig. 5.7b and f (zoom-in of 7.1 THz peak in SI Fig. 5.7c and g). The Fourier amplitudes at 3.85 THz and 7.1 THz, which corresponds to the frequency position of $E(TO_1)$ and $E(TO_3)$ features,

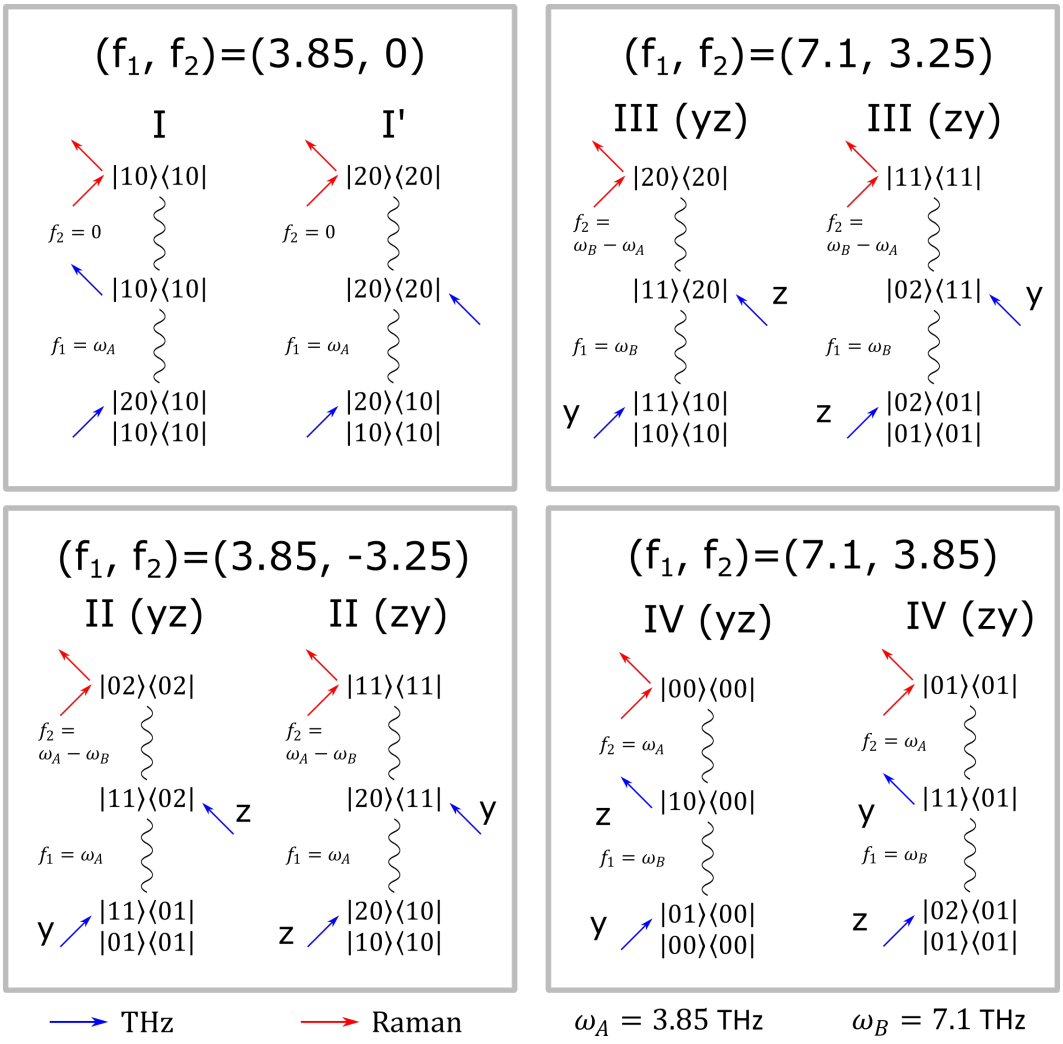

Figure 5.6: Complete Feynman pathway analysis for the four 2D features observed. Symmetry-allowed lowest energy pathways are assigned for each THz polarization. Polarization requirements for THz transitions are labelled.

are plotted against the field strength of the varied THz field, as shown in SI Fig. 5.7d and h. Both features are linearly proportional to the THz field strength, resulting in an overall field dependence of

$$S_{3.85\text{THz}}, S_{7.1\text{THz}} \propto E_A^{THz} \cdot E_B^{THz}$$

.

Conservation of momentum and energy in 2D-TTR spectroscopy of PhPs

In addition to the phase matching condition for the 800 nm probe pulse described in the main text, which determines the frequency and wavevector of the PhPs that

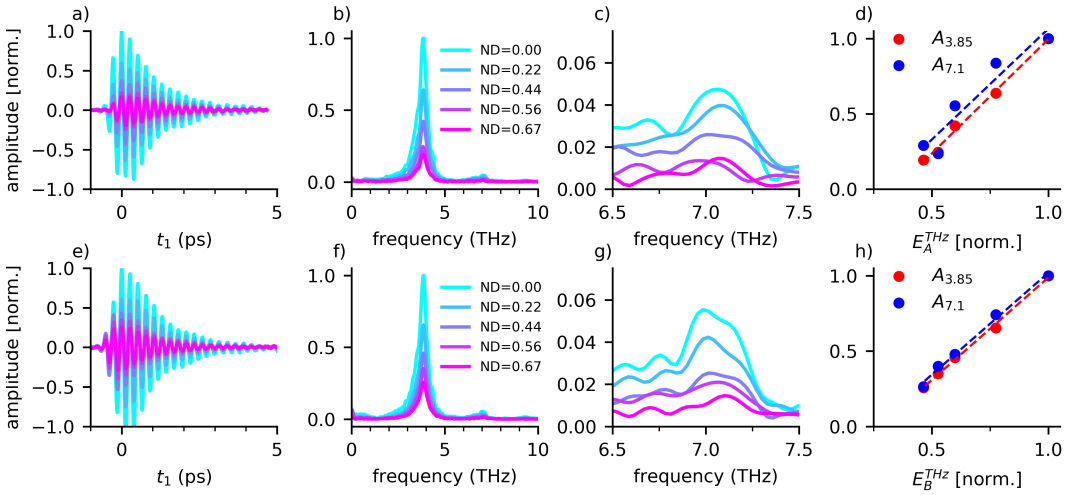

Figure 5.7: THz field strength dependence of the 2D-TTR signal along t_1 for (a-d) E_A^{THz} and (e-h) E_B^{THz}. The time domain signals are shown in a and e. The corresponding Fourier transforms are shown in b and f. Zoom-in of the 7.1 THz peak is shown in c and g. (d,h) Normalized amplitude at E(TO_1) (3.85 THz) and E(TO_3) (7.1 THz) PhP frequencies are plotted against the varied THz field strength. Best linear fits are provided as dashed lines.

can be probed, the THz interactions in the Feynman pathway assignments must also conserve momentum. Linear THz interactions that induce 1 quanta transitions are naturally phase-matched to PhPs over a wide range of wavevectors. Here, we focus on the nonlinear THz transition from E(TO_3) to E(TO_1) observed in pathway IV. SI Fig. 5.8 shows the THz dispersion curves and phase-matching conditions for THz polarization ordering a) zy and b) yz, respectively (the phonon branches and THz dispersion curves are obatined from two different publications [20, 23], which have minor discrepancies in the phonon mode frequencies derived). Experimentally measured f_2 frequency of peak IV (3.85 THz) indicates that the two THz interactions produce a phase-matched forward-propagating E(TO_1) PhP state with a wavevector of $\sim 1250\ \mathrm{cm}^{-1}$. For the zy THz polarization sequence, conservation of momentum and energy can be achieved with a z-polarized THz pulse at 7.1 THz (wavevector of $\sim 2000\ \mathrm{cm}^{-1}$) and a y-polarized pulse at 3.25 THz (wavevector of $\sim 850\ \mathrm{cm}^{-1}$). Specifically, the 3.25 THz nonlinear transition is a de-excitation process from the E(TO_3) branch to the E(TO_1) branch (see IV (zy) pathway in SI Fig. 5.6), which interacts with the "negative" frequency and momentum component of the incident pulse (similar to stimulated emission of a forward propagating THz photon) [36],

$$E_{THz}(r,t) = E \cdot \cos(\omega \cdot t + k \cdot r) = \frac{E}{2} \cdot (e^{\omega \cdot t + k \cdot r} + e^{-\omega \cdot t - k \cdot r})$$

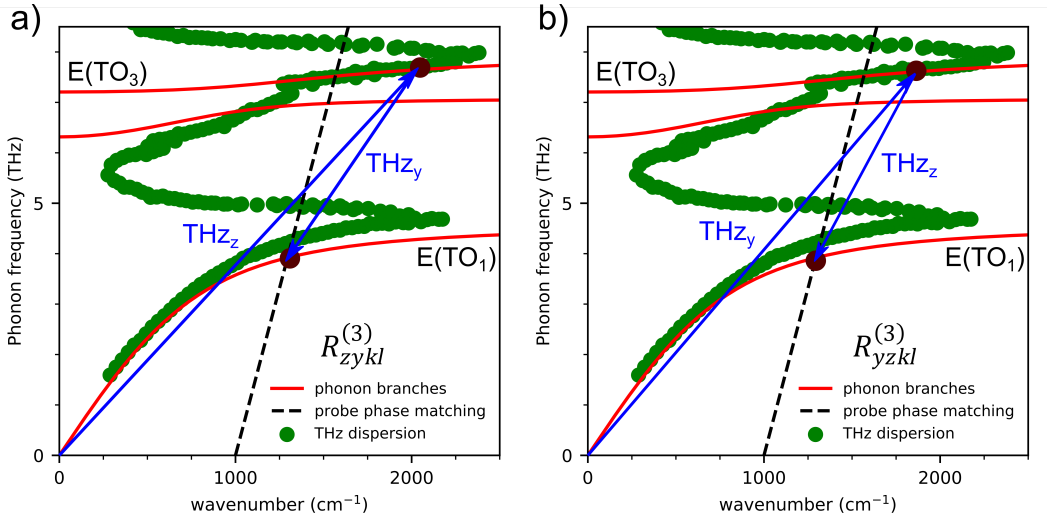

Figure 5.8: Energy and momentum conservation requirements for the THz transitions in Feynman pathways (a) IV (zy) and (b) IV (yz). Physical parameters of the E-symmetry phonon branches are obtained from Barker et al. [23]. The dispersion of the THz electric field is digitized from experimental measurements by Kojima et al. [20].

. To conserve momentum and energy, the THz-PhP interaction must have a negative wavevector, as shown by the negative arrow in SI Fig. 5. Similarly, for the yz THz polarization sequence, conservation of momentum and energy can be achieved with a y-polarized THz pulse at 7.1 THz (wavevector of $\sim$ 1800 cm^{-1}) and a z-polarized pulse at 3.25 THz (wavevector of $\sim$ 550 cm^{-1}). Due to the flatness of the E(TO$_3$) PhP branch, the E(TO$_3$) PhP at wavevectors $\sim$ 1800 cm^{-1} and $\sim$ 2000 cm^{-1} differ in energy by less than 0.1 THz, which is on the order of our experimental frequency resolution along f_1.

Nonlinear transitions mediated by A$_1$ symmetry PhP modes

An alternative mechanism for the nonlinear THz transition observed in pathway IV involves nonlinear scattering of A$_1$ symmetry PhPs. While A$_1$ PhPs are not detected in the anisotropic probing scheme, they are nevertheless excited by the z-polarized broadband THz pulses employed in this work. Scattering pathways that produce E-symmetry PhPs from only input A$_1$-symmetry PhPs, such as

$$\mathrm{A_1(TO_1) + A_1(TO_1) \longrightarrow E(TO_3)}$$

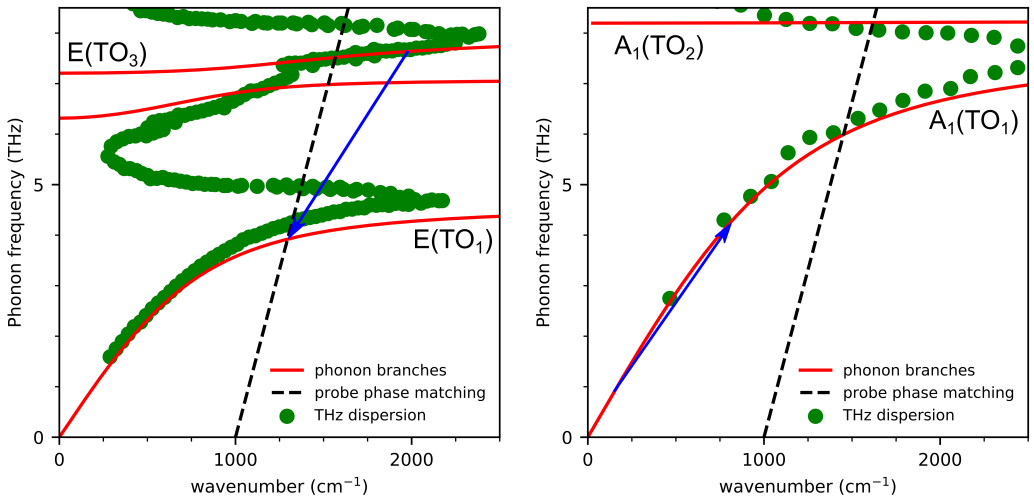

Figure 5.9: Energy and momentum conservation requirements for a nonlinear transition involving a scattered A_1-symmetry PhP. Physical parameters of the E- and A_1-symmetry phonon branches are obtained from Barker et al. [23]. The dispersion of the THz electric field is digitized from experimental measurements by Kojima et al. (E: [20], A_1: [37]).

are symmetry forbidden [38, 39]. Here, we consider the following symmetry-allowed scattering process:

$$E(TO_3) + A_1(TO_1) \longrightarrow E(TO_1) + A_1^*(TO_1)$$

where $A_1^*(TO_1)$ gains the energy and momentum difference between the $E(TO_3)$ and $E(TO_1)$ PhPs. The THz dispersion curves for both E and A_1 symmetry PhPs in $LiNbO_3$ are shown in SI Fig. 5.9. The blue arrows show an example of the nonlinear transition in the E-symmetry PhPs and the corresponding scattered $A_1(TO_1)$ PhP that conserves energy and momentum. Specifically, scattering of an $A_1(TO_1)$ PhP (1 THz, 150 cm^{-1}) with an $E(TO_3)$ PhP (7.1 THz, 1900 cm^{-1}) could result in the 800 nm phase-matched $E(TO_1)$ PhP (3.85 THz, 1250 cm^{-1}) and an $A_1^*(TO_1)$ PhP (4.25 THz, 800 cm^{-1}). A number of other combinations of $A_1(TO_1)$ and $E(TO_3)$ PhP momentum and energies can also lead to the observed 3.85 THz $E(TO_1)$ PhP. While this work is unable to investigate this scattering mechanism experimentally, the inherent randomness in the magnitude of energy and momentum transfer between scattered phonon-polaritons would limit the population of scattering products that are phase-matched with the 800 nm probe pulse. To provide a first-order estimate of the scarcity of phase-matched scatter products, we consider the range of energy and wavevectors that are phase-matched with the probe pulse. The probe pulse is

centered at 800 nm and has approximately 60 nm of bandwidth. For the $E(TO_1)$ branch, PhPs are only phase-matched in a 0.06 THz and 80 cm^{-1} energy and wavevector window. In contrast, $A_1(TO_1)$ PhPs can span over 7 THz and 1000 cm^{-1}. Thus, the majority of scattering products would not be phase-matched and detectable by the probe pulse, suggesting that nonlinear phonon scattering is not a major contributor for the features observed.

References

[1] Roman Mankowsky et al. "Ultrafast reversal of the ferroelectric polarization." *Physical Review Letters* 118.19 (2017), pp. 1–5.

[2] Dmytro Afanasiev et al. "Ultrafast control of magnetic interactions via light-driven phonons." *Nature Materials* 20.5 (2021), pp. 607–611.

[3] Roman Mankowsky et al. "Nonlinear lattice dynamics as a basis for enhanced superconductivity in YBa2Cu3O6.5." *Nature* 516.729 (2014), pp. 71–73.

[4] Sebastian Maehrlein et al. "Terahertz sum-frequency excitation of a Raman-active phonon." *Physical Review Letters* 119.12 (2017), pp. 1–6.

[5] Yao Lu et al. "Giant enhancement of THz-frequency optical nonlinearity by phonon polariton in ionic crystals." *Nature Communications* 12.1 (2021), pp. 1–8.

[6] Brittany E. Knighton et al. "Terahertz waveform considerations for nonlinearly driving lattice vibrations." *Journal of Applied Physics* 125.14 (2019).

[7] Aleksey A. Melnikov et al. "Coherent phonons in a Bi2Se3 film generated by an intense single-cycle THz pulse." *Physical Review B* 97.21 (2018), pp. 1–10.

[8] Martin J. Neugebauer et al. " Comparison of coherent phonon generation by electronic and ionic Raman scattering in LaAlO3." *Physical Review Research* 3.1 (2021), p. 13126.

[9] Dominik M. Juraschek, Derek S. Wang, and Prineha Narang. "Sum-frequency excitation of coherent magnons." *Physical Review B* 103.9 (2021).

[10] Dominik M. Juraschek and Sebastian F. Maehrlein. "Sum-frequency ionic Raman scattering." *Physical Review B* 97.17 (2018), pp. 1–8.

[11] Vincent Juvé et al. "Ultrafast tunable modulation of light polarization at terahertz frequencies." *Optics Letters* 43.24 (2018), p. 5905.

[12] Carlo Vicario et al. "Narrow-band and tunable intense terahertz pulses for mode-selective coherent phonon excitation." *Applied Physics Letters* 117.10 (2020), pp. 1–5.

[13] Biaolong Liu et al. “Generation of narrowband, high-intensity, carrier-envelope phase-stable pulses tunable between 4 and 18 THz.” *Optics Letters* 42.1 (2017), p. 129.

[14] Simone Sanna et al. “Raman scattering efficiency in LiTaO3 and LiNbO3 crystals.” *Physical Review B - Condensed Matter and Materials Physics* 91.22 (2015), pp. 1–9.

[15] Simone Sanna and Wolf Gero Schmidt. “Lithium niobate X -cut, y -cut, and Z -cut surfaces from ab initio theory.” *Physical Review B - Condensed Matter and Materials Physics* 81.21 (2010), pp. 1–11.

[16] Yuki Ikegaya et al. “Real-time observation of phonon-polariton dynamics in ferroelectric LiNbO3 in time-frequency space.” *Applied Physics Letters* 107.6 (2015).

[17] Blake S. Dastrup, Jacob R. Hall, and Jeremy A. Johnson. “Experimental determination of the interatomic potential in LiNbO3 via ultrafast lattice control.” *Applied Physics Letters* 110.16 (2017).

[18] Brittany E. Knighton et al. “Measurement of a phonon-polariton dispersion curve by varying the excitation wavelength.” *Physical Review B* 97.21 (2018), pp. 1–6.

[19] Tomonori Kuribayashi et al. “Anharmonic phonon-polariton dynamics in ferroelectric LiNbO3 studied with single-shot pump-probe imaging spectroscopy.” *Journal of Applied Physics* 123.17 (2018).

[20] Seiji Kojima. “Broadband terahertz spectroscopy of phonon-polariton dispersion in ferroelectrics.” *Photonics* 5.4 (2018), pp. 1–12.

[21] Vasile Caciuc, Andrei V. Postnikov, and Gunnar Borstel. “Ab initio structure and zone-center phonons in LiNbO 3.” *Physical Review B* 61.13 (2000), pp. 8806–8813.

[22] Koichi Momma and Fujio Izumi. “VESTA 3 for three-dimensional visualization of crystal, volumetric and morphology data.” *Journal of Applied Crystallography* 44.6 (2011), pp. 1272–1276.

[23] Alfred S. Barker and Rodney Loudon. “Dielectric properties and optical phonons in LiNbO3.” *Physical Review* 158.2 (1967), pp. 433–445.

[24] Courtney L. Johnson, Brittany E. Knighton, and Jeremy A. Johnson. “Distinguishing nonlinear terahertz excitation pathways with two-dimensional spectroscopy.” *Physical Review Letters* 122.7 (2019), p. 73901.

[25] Griffin Mead et al. “Sum-frequency signals in 2D-Terahertz-Terahertz-Raman spectroscopy.” *The Journal of Physical Chemistry B* 124.40 (2020), pp. 8904–8908.

[26] David Sidler and Peter Hamm. “A Feynman diagram description of the 2D-Raman-THz response of amorphous ice.” *Journal of Chemical Physics* 153.4 (2020).

[27] David Sidler and Peter Hamm. “Feynman diagram description of 2D-Raman-THz spectroscopy applied to water.” *Journal of Chemical Physics* 150.4 (2019).

[28] Ian A. Finneran et al. “Coherent two-dimensional terahertz-terahertz-Raman spectroscopy.” *Proceedings of the National Academy of Sciences* 113.25 (2016), pp. 6857–6861.

[29] Keita Matsumoto and Takuya Satoh. “Selective imaging of the terahertz electric field of the phonon-polariton in LiNbO3.” *Physical Review B* 102.9 (2020), pp. 1–6.

[30] Carmine Somma et al. “High-field terahertz bulk photovoltaic effect in lithium niobate.” *Physical Review Letters* 112.14 (2014).

[31] Gustavo Ciardi et al. “Signatures of intra- and intermolecular vibrational coupling in halogenated liquids revealed by two-dimensional Raman-terahertz spectroscopy.” *Journal of Physical Chemistry Letters* 10.15 (2019), pp. 4463–4468.

[32] Alec Owens, Andrey Yachmenev, and Jochen Küpper. “Coherent control of the rotation axis of molecular superrotors.” *Journal of Physical Chemistry Letters* 9.15 (2018), pp. 4206–4209.

[33] Tae Gwan Park et al. “Coherent control of interlayer vibrations in Bi2Se3van der Waals thin-films.” *Nanoscale* 13.45 (2021), pp. 19264–19273.

[34] Jan Gerrit Horstmann et al. “Coherenat control of a surface structural phase transition.” *Nature* 583.7815 (2020), pp. 232–236.

[35] Ioan B. Magdău et al. “Interpretation of the THz-THz-Raman spectrum of bromoform.” *The Journal of Physical Chemistry A* (2019), acs.jpca.9b05165.

[36] Peter Hamm and Martin Zanni. *Concepts and Methods of 2D Infrared Spectroscopy*. Cambridge: Cambridge University Press, 2011.

[37] Seiji Kojima. “Terahertz polariton dispersion in uniaxial optical crystals.” *Progress in Electromagnetics Research Letters* 77.July (2018), pp. 109–115.

[38] Antonio Cammarata. “Phonon-phonon scattering selection rules and control: An application to nanofriction and thermal transport.” *RSC Advances* 9.64 (2019), pp. 37491–37496.

[39] Runqing Yang et al. “Crystal symmetry based selection rules for anharmonic phonon-phonon scattering from a group theory formalism.” *Physical Review B* 103.18 (2021), p. 184302.

Chapter 6

TERAHERTZ SUM-FREQUENCY EXCITATION OF COHERENT OPTICAL PHONONS IN THE TWO-DIMENSIONAL SEMICONDUCTOR WSE_2

The work presented in this chapter was conducted in collaboration with postdoc Satoshi Kusaba, Prof. Ikufumi Katayama, and Prof. Jun Takeda from the Yokohama National University (YNU) in Japan.

6.1 Introduction

The advancement of intense ultrafast light fields has opened up new avenues to control material properties via elementary excitations of carriers and lattice dynamics [1–9]. Transition metal dichalcogenides, TMDs, are promising layered semiconductor platforms due to their attractive opto-electronic properties, including layer-dependent tunable electronic structures [10, 11] and non-trivial spin-valley couplings [12]. Recent works using mid-IR radiation have observed coherently-driven valley carriers [3, 5–7] and displayed possible control of the excitonic states [9] in TMDs, demonstrating promise as a new light source and a platform for attosecond physics. The nuclear degrees of freedom, on the other hand, are significantly under-explored despite its fundamental importance. The in-plane phonon modes are highly conserved between monolayer, multilayer, and bulk TMDs [13]. While a number of optical phonon modes in the THz frequency range have been observed and assigned with non-resonant Raman and coherent phonon spectroscopies in the visible and near-IR wavelengths [14, 15], their driven dynamics, which are most accessible with THz excitations, have yet to be investigated. To date, THz spectroscopic studies on TMDs have mainly focused on the carrier dynamics at near 1 THz [16–18]. In contrast, broadband THz irradiation, which is capable of efficient excitation of both IR- and Raman-active phonon modes, enables comprehensive investigation of THz phonon dynamics in TMDs, including excitation mechanisms [19, 20], phonon-phonon couplings [1], and anharmonicities [21]. These insights are foundation to potential nonlinear phononic schemes to manipulate the material properties of TMDs [22].

In this chapter, we report direct observation of THz-induced coherent phonon oscillations in thin bulk WSe_2, one of the TMDs. Specifically, we performed THz

Kerr effect (TKE) spectroscopy, which employs intense and broadband ultrafast THz pulses to coherently drive phonon excitations and detects the transient birefringence caused by the phonon wavepackets. The observed phonon wavepackets are at 7-8 THz, which we attribute to the E_{2g} optical phonon modes. The oscillation amplitude of the phonon signal is proportional to the square of the THz electric field strength, suggesting a sum-frequency (SF) THz excitation mechanism. Further, we present a quantum mode-specific picture of the SF THz excitation process via the polarizability operator. Alternative mechanisms, including nonlinear phonon-phonon coupling and carrier-phonon coupling, are discussed and ruled out.

6.2 Sample preparation and experimental setup

The THz pulse shape and bandwidth employed in this work is shown in Fig. 6.1a and b, respectively. The THz bandwidth extends up to $\sim$ 12 THz (-20 dB), which is capable of both resonant one-photon and SF two-photon excitations of the various IR- and Raman-active phonon modes of WSe_2 within the THz bandwidth. The TKE spectrometer employed in this work has been described in detail previously [21, 23]. A schematic is provided in Fig. 6.1c. The inset shows the polarization of the THz and probe pulses relative to the crystalline axes of WSe_2, named the armchair (AC) and the zigzag (ZZ) directions. Polarization of the probe pulse is controlled by a half-wave plate ($\lambda/2$). The polarizers P1 and P2 are parallel and perpendicular to the probe polarization, respectively.

Bulk WSe_2 single crystals are provided by our collaborators at YNU. Thin ($< 1\mu$m) WSe_2 films of 3-4 mm in diameter were obtained by mechanical exfoliation using an adhesive tape (Nitto ELP BT-130E-SL). Due to the optical absorption of WSe_2 at the probe wavelength (800 nm), the sample thickness needs to be carefully chosen to maximize signal-to-noise. While thinner crystals absorb less probe photons, the total phase delay over the thickness of the crystal is also decreased.

For TKE measurements, we employ free-standing WSe_2 thin film samples to eliminate substrate effects on the phonon mode frequencies of WSe_2 and potential nonlinear signals from the substrate. The sample is mounted free-standing across a 400 μm pinhole (Thorlabs), as shown in Fig. 6.2. The pinhole serves two primary purposes. First, the thin WSe_2 samples typically varied in thickness across the few mm sample, with regions of the same thickness $\sim$ 1 mm^2 in size. We positioned the WSe_2 sample such that the thickness is uniform within the pinhole. Secondly, the boundaries between different thickness regions cause scatter of the probe beam,

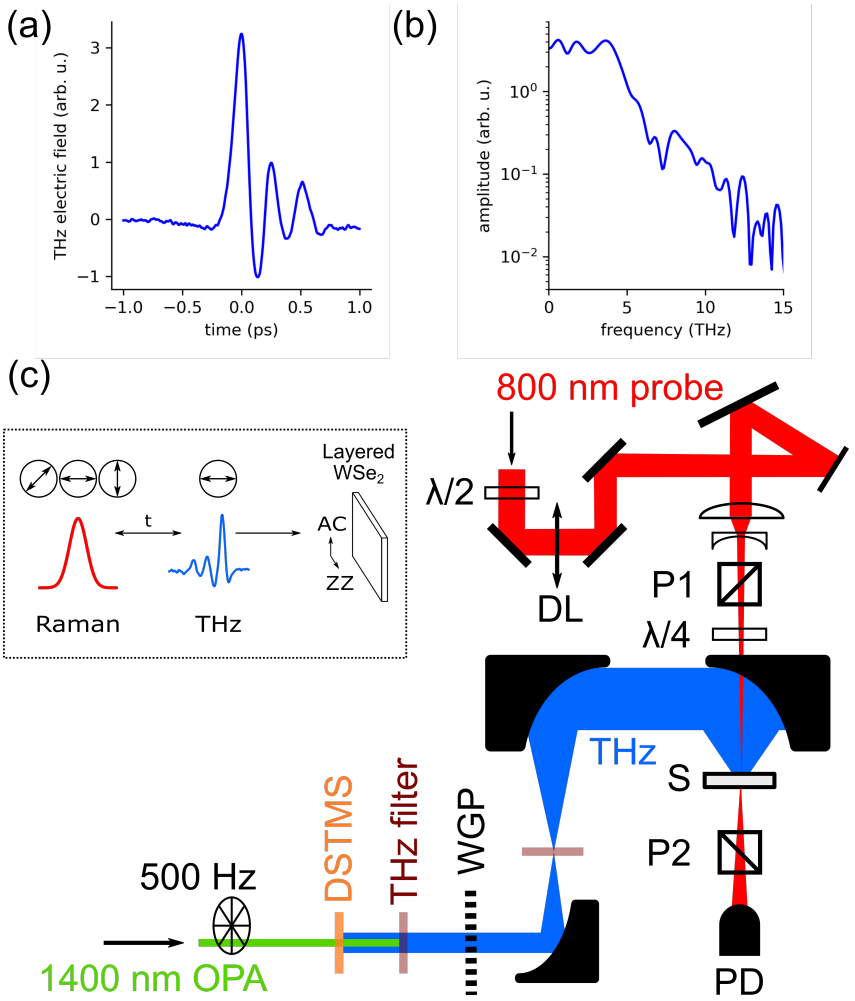

Figure 6.1: TKE spectroscopy of WSe_2. (a) THz pulse shape measured with electro-optic sampling (EOS) on 100 μm GaP. (b) Corresponding THz bandwidth of (a). (c) Schematic of the TKE spectrometer. WGP: wire-grid polarizer; P1, P2: polarizers; S: sample; PD: photodiode; DL: optical delay line; $\lambda/2$: half-wave plate; $\lambda/4$: quarter-wave plate. Inset: Polarization of the THz pump and optical probe pulses relative to the crystal axes of WSe_2.

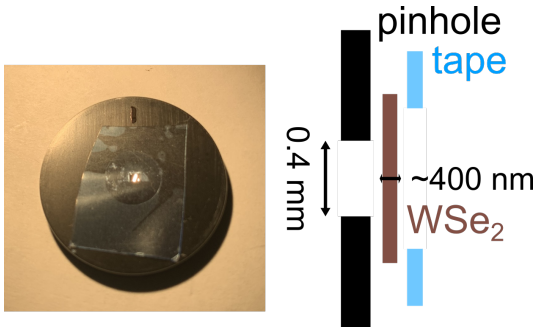

Figure 6.2: Free standing sample mount for thin film WSe_2 samples. (left) Photo of the free standing WSe_2 mounted on a 400 μm diameter pinhole. (right) Schematic of the WSe_2 sample assembly.

which increases the background noise of TKE spectroscopy significantly. A pinhole with a diameter that matches the THz-pumped region of the sample (roughly 400-500 μm in diameter) serves to spatially filter the scattered photons to enable detection of weak nonlinear signals.

6.3 Results and discussion

1D TKE results

The crystal structure of WSe_2 is shown in Fig. 6.3. The two in-plane axes of WSe_2, known as the AC and ZZ directions, are shown by red and blue arrows. The crystal orientations of the WSe_2 thin films were assigned using polarization-resolved second harmonic generation (SHG) spectroscopy, where the polarization-dependent SHG amplitudes show six-fold symmetry with respect to polarization angle due to the point group of the monolayers of WSe_2 (D_{3h}) [24]. The optically-active phonon modes and their corresponding lattice motion is also shown in Fig. 6.3 [25, 26]. Note that the $E-$ and $A-$symmetry phonons modes are in-plane and out-of-plane modes, respectively. The E^1_{2g} and A_{1g} modes are at 248 and 250 cm^{-1}, respectively [25]. The E^2_{2g} mode appears at frequencies below 50 cm^{-1} [25].

In TKE spectroscopy, the WSe_2 samples are subject to intense and broadband ultrafast THz pulses to drive coherent phonon dynamics [27, 28]. Figure 6.4 shows the TKE spepctra of WSe_2, where the polarization of both the THz and probe pulses are parallel to the AC direction. The TKE signal consists of two main features: an oscillatory signal and an exponential decay component. The exponential decay component was fit by a bi-exponential function, which yield $\sim$ 100 fs (fast) and $\sim$ 400 fs (slow) decay components. Similar features have previously been reported in TKE signals of other semiconductors, such as Bi_2Se_3, and were attributed to the

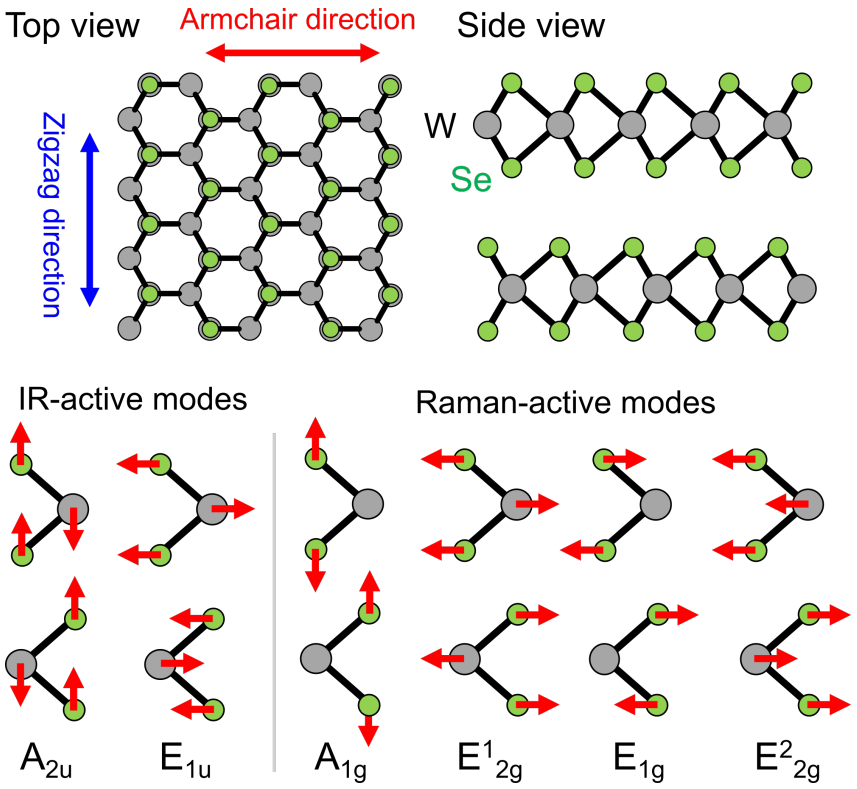

Figure 6.3: Crystal structure and phonon modes of WSe_2. (top) Crystal lattice structure of WSe_2. (bottom) Lattice motion of IR- and Raman-active modes of WSe_2.

relaxation of thermalized electron population perturbed by the intense THz pump electric field [27]. We assign the observed exponential decay signal to similar origins due to the comparable THz field strength employed in this work. Subtraction of the exponential decay signal isolates the oscillatory component, as shown by the green difference trace in Fig. 6.4, which has a lifetime of $\sim$ 1 ps. The Fourier transform (FT) spectra of the isolated oscillatory component is shown in the inset of Fig. 6.4, which reveals a clear peak at $\sim$ 7.5 THz. The frequency of this peak matches that of the E_{2g} and A_{1g} phonon modes of WSe_2. Note that TKE spectroscopy is only sensitive to anisotropic vibrational modes due to the cross-polarized detection scheme. Thus, we attribute the observed oscillatory signal to transient anisotropy induced by coherently excited vibrational wavepackets of the E_{2g} symmetry phonon mode (A_{1g} is the totally symmetric phonon mode).

To further elucidate the underlying excitation mechanism of the coherent phonon signal, TKE signals were measured with varying THz pump field strengths. The THz field strength is systematically decreased by reducing the mid-IR pump power

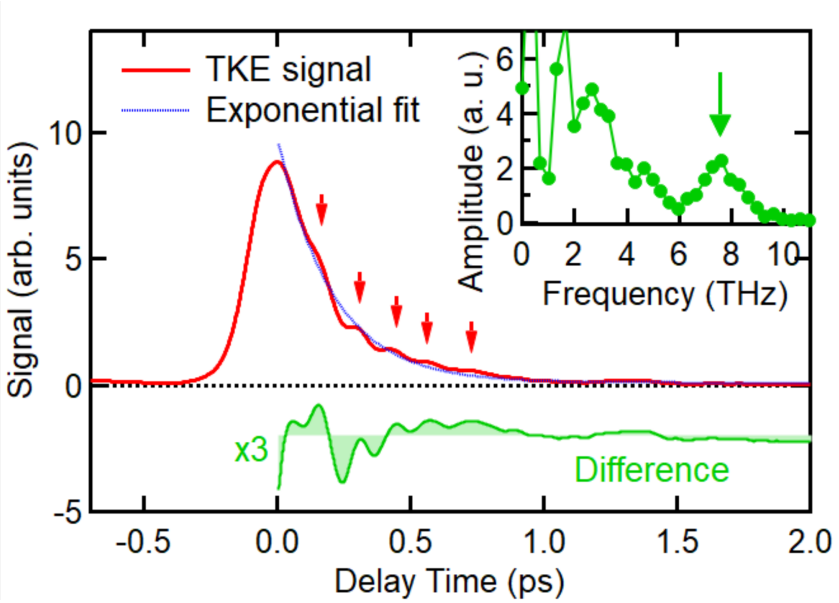

Figure 6.4: TKE spectra for WSe_2. (red) TKE time domain signal of WSe_2 thin films. The polarization of the THz pump and optical probe pulses are parallel to the AC direction. (green) Difference trace with the exponential decay component subtracted to isolate the oscillatory signal. (inset) The corresponding FT of the difference signal, which reveals the ~ 7.5 THz E_{2g} phonon peak.

incident on the THz generation crystal (DSTMS) with a neutral density (ND) filter wheel. Linearity between the power of the mid-IR pump pulse and that of the generated THz pulse has been verified with EOS techniques. The TKE signals for WSe_2 at different THz field strengths are shown in Fig. 6.5a. The corresponding FT spectra are shown in Fig. 6.5b and zoomed into the phonon peak in Fig. 6.5c. Two regions of the FT spectra are analyzed, namely, the relaxation of the thermalized electrons (1-2 THz) and the coherent excitation of the E_{2g} phonon wavepackets (7-8 THz). The region between 0-1 THz was avoided due to higher contributions of potential systematic noise sources. The integrated intensity in each of the regions as a function of normalized THz field strength is shown in Fig. 6.5d and 6.5e, respectively. Both features display clear quadratic dependence with respect to the incident THz electric field, indicating the involvement of two THz photons via a SF excitation process. Similar SF THz excitation processes have also been observed in solids (diamond [4]) and liquids (halogenated methane [20]).

Below, we provide a quantum-state specific explanation for the SF THz excitation of the E_{2g} mode in WSe_2. The phonon modes with E_{2g} symmetry in WSe_2 is Raman-active and IR-inactive. Using the double-sided Feynman pathway notation

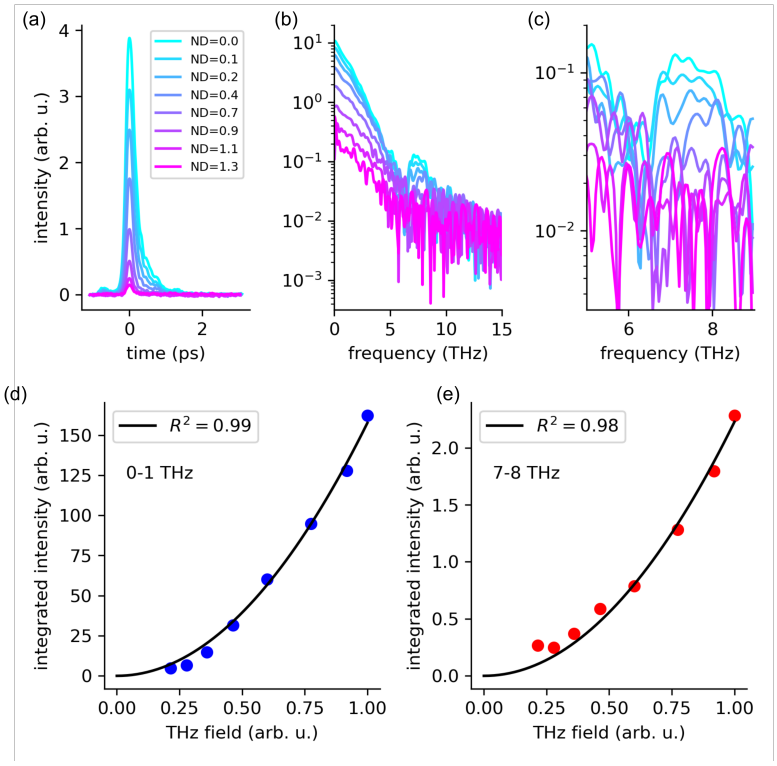

Figure 6.5: THz field strength dependence of the TKE spectra for WSe_2. (a) TKE signal of WSe_2 at different THz electric field strengths. (b) Corresponding FT spectra of (a). (c) The FT spectra in (b) zoomed in to highlight the phonon peak. Integrated FT amplitude between (d) 1-2 THz and (e) 7-8 THz as a function of THz field strength.

for the density matrix, the coherent state after every field interaction is denoted using $|n\rangle\langle m|$, where n and m are the number of quanta in the E_{2g} phonon state on the ket and bra side of the density matrix [21]. If two resonant THz interactions were to take place, the resulting state will be either $|2\rangle\langle 0|$, which will induce oscillations at twice the phonon frequency, or $|1\rangle\langle 1|$, which is a population state and does not produce an oscillatory signal. Both of these coherent states are inconsistent with our observed experimental spectra. In contrast, the resulting state after the SF THz process is $|1\rangle\langle 0|$, which oscillates at the observed frequency of $\sim$ 7.5 THz. The $|1\rangle\langle 0|$ coherent state can then undergo a Raman interaction with the probe pulse to end in the ground state $|0\rangle\langle 0|$, forming a Feynman pathway that is linear in polarizability and fully-allowed for the E_{2g} mode [20].

An alternative mechanism that also has quadratic scaling with respect to the THz field strength is the trilinear coupling of phonon modes [19, 27]. Specifically, two IR-active phonon modes are coherent excited and nonlinearly coupled to excite the

E_{2g} Raman-active phonon mode observed. Such processes require both symmetry and energy matching to occur. The IR-active phonon modes in WSe_2 are of A_{2u} and E_{1u} symmetry. The relevant symmetry products are $\langle E_{2g}|A_{2u}E_{1u}\rangle$, $\langle E_{2g}|E_{1u}E_{1u}\rangle$, $\langle E_{2g}|A_{2u}A_{2u}\rangle$. Only $\langle E_{2g}|E_{1u}E_{1u}\rangle \supset A_{1g}$ is symmetry allowed. However, the E_{1u} phonon modes in WSe_2 has almost identical energy as the E_{2g} phonon modes. Therefore, conservation of energy is not satisfied in the trilinear coupling mechanism that involves the scattering of two E_{1u} phonons into one E_{2g} phonon. We also note that the excitation of the E_{2g} mode through electron-phonon coupling mechanisms are unlikely because the THz photon energy (< 40 meV) is substantially lower than the bandgap of WSe_2 (1.2 eV).

6.4 Conclusion

In summary, we demonstrate coherent phonon excitation for layered semiconductor WSe_2 via intense and broadband ultrafast THz pulses. In addition to the thermalized electron response, we directly observe oscillatory signals with a frequency of ~ 7.5 THz and a lifetime of ~ 1 ps, which we attribute to coherently-excited wavepackets of the E_{2g} phonon mode. The amplitude of the phonon signals scales quadratically with respect to THz electric field strength, which implies a sum-frequency excitation mechanism where the sum of the two incident photons' energies matches that of the excited phonon mode. We further justify the sum-frequency excitation mechanism in a quantum-state specific picture and rule out alternative mechanisms, including nonlinear phonon-phonon coupling and electron-phonon coupling. Our results provide helpful mechanistic insights into the driven-dynamics and coherent control of phonons by strong THz fields in solid materials.

References

[1] Matteo Rini et al. "Control of the electronic phase of a manganite by mode-selective vibrational excitation." *Nature* 449.7158 (2007), pp. 72–74.

[2] Tobias Kampfrath, Koichiro Tanaka, and Keith A. Nelson. "Resonant and nonresonant control over matter and light by intense terahertz transients." *Nature Photonics* 7.9 (2013), pp. 680–690.

[3] Hanzhe Liu et al. "High-harmonic generation from an atomically thin semiconductor." *Nature Physics* 13.3 (2017), pp. 262–265.

[4] Sebastian Maehrlein et al. "Terahertz sum-frequency excitation of a Raman-active phonon." *Physical Review Letters* 119.12 (2017), pp. 1–6.

[5] Naotaka Yoshikawa, Tomohiro Tamaya, and Koichiro Tanaka. “Optics: High-harmonic generation in graphene enhanced by elliptically polarized light excitation.” *Science* 356.6339 (2017), pp. 736–738.

[6] Shambhu Ghimire and David A. Reis. “High-harmonic generation from solids.” *Nature Physics* 15.1 (2019), pp. 10–16.

[7] Naotaka Yoshikawa et al. “Interband resonant high-harmonic generation by valley polarized electron–hole pairs.” *Nature Communications* 10.1 (2019), pp. 1–7.

[8] Kento Uchida et al. “Inherent limit to coherent phonon generation under nonresonant light-field driving.” *Physical Review B* 101.9 (2020), pp. 1–5.

[9] Kento Uchida et al. “Diabatic and adiabatic transitions between Floquet states imprinted in coherent exciton emission in monolayer WSe2.” *Science Advances* 8.51 (2022), pp. 1–8.

[10] Andrea Splendiani et al. “Emerging photoluminescence in monolayer MoS2.” *Nano Letters* 10.4 (2010), pp. 1271–1275.

[11] Kin Fai Mak et al. “Atomically thin MoS2: A new direct-gap semiconductor.” *Physical Review Letters* 105.13 (2010), pp. 2–5.

[12] Di Xiao et al. “Coupled spin and valley physics in monolayers of MoS 2 and other group-VI dichalcogenides.” *Physical Review Letters* 108.19 (2012), pp. 1–5.

[13] Qingan Cai et al. “Monolayer-like lattice dynamics in bulk WSe2.” *Materials Today Physics* 28.July (2022), p. 100856.

[14] Tae Young Jeong et al. “Coherent lattice vibrations in mono- and few-layer WSe2.” *ACS Nano* 10.5 (2016), pp. 5560–5566.

[15] Soungmin Bae et al. “K-point longitudinal acoustic phonons are responsible for ultrafast intervalley scattering in monolayer MoSe2.” *Nature Communications* 13.1 (2022), pp. 1–8.

[16] Chun Hung Lui et al. “Trion-induced negative photoconductivity in monolayer MoS2.” *Physical Review Letters* 113.16 (2014), pp. 1–5.

[17] Callum J. Docherty et al. “Ultrafast transient terahertz conductivity of monolayer MoS2and WSe2 grown by chemical vapor deposition.” *ACS Nano* 8.11 (2014), pp. 11147–11153.

[18] Xianding Yan et al. “Dielectric property of MoS_2 crystal in terahertz and visible regions.” *Applied Optics* 54.22 (2015), p. 6732.

[19] Courtney L. Johnson, Brittany E. Knighton, and Jeremy A. Johnson. “Distinguishing nonlinear terahertz excitation pathways with two-dimensional spectroscopy.” *Physical Review Letters* 122.7 (2019), p. 73901.

[20] Griffin Mead et al. “Sum-frequency signals in 2D-Terahertz-Terahertz-Raman spectroscopy.” *The Journal of Physical Chemistry B* 124.40 (2020), pp. 8904–8908.

[21] Haw-Wei Lin, Griffin Mead, and Geoffrey A. Blake. “Mapping LiNbO$_3$ phonon-polariton nonlinearities with 2D THz-THz-Raman spectroscopy.” *Physical Review Letters* 129.20 (2022), p. 207401.

[22] Ankit S. Disa, Tobia F. Nova, and Andrea Cavalleri. “Engineering crystal structures with light.” *Nature Physics* 17.10 (2021), pp. 1087–1092.

[23] Marco A. Allodi, Ian A. Finneran, and Geoffrey A. Blake. “Nonlinear terahertz coherent excitation of vibrational modes of liquids.” *Journal of Chemical Physics* 143.23 (2015).

[24] Nardeep Kumar et al. “Second harmonic microscopy of monolayer MoS2.” *Physical Review B - Condensed Matter and Materials Physics* 87.16 (2013), pp. 1–6.

[25] Weijie Zhao et al. “Lattice dynamics in mono- and few-layer sheets of WS2 and WSe2.” *Nanoscale* 5.20 (2013), pp. 9677–9683.

[26] Elena Corro et al. “Excited excitonic states in 1L, 2L, 3L, and bulk WSe2 observed by resonant Raman spectroscopy.” *ACS Nano* 8.9 (2014), pp. 9629–9635.

[27] Aleksey A. Melnikov et al. “Coherent phonons in a Bi2Se3 film generated by an intense single-cycle THz pulse.” *Physical Review B* 97.21 (2018), pp. 1–10.

[28] Blake S. Dastrup, Jacob R. Hall, and Jeremy A. Johnson. “Experimental determination of the interatomic potential in LiNbO3 via ultrafast lattice control.” *Applied Physics Letters* 110.16 (2017).

Chapter 7

CONCLUSION AND FUTURE DIRECTIONS

7.1 Summary

The delocalized intermolecular degrees of freedom in condensed matter systems have long been under-explored, yet these fundamental motions, most clearly probed in the THz region, are perhaps the most important contributor to their room temperature chemical and physical properties. Recent, and ongoing, advancements in THz generation and detection technologies have led to rapid development of various ultrafast THz spectroscopic techniques that are specially designed to investigate the dynamics and correlative behaviors of these THz soft modes.

My thesis work has been focused on the development and demonstration of nonlinear THz spectroscopic techniques that measure strongly photo-driven dynamics of THz vibrational modes in both liquid and solid systems, which provide quantum-mechanical insight into the underlying coherent excitation mechanisms, nonlinear coupling interactions, and sources of anharmonicities in the system. In order to expand the range of possible samples, we have continued to pursue instrument advancements of 2D-TTR spectroscopy. Specifically, we have developed a novel nonlinear imaging method utilizing the $\chi^{(3)}$ response of GaP to allow direct optimization of the nonlinear signals, providing significant improvement to the consistency of two-emitter 2D THz spectroscopies. Further, we have extended the single-shot detection scheme to 2D-TTR spectroscopy to reduce experimental acquisition time by up to two orders-of-magnitude, making measurements of weaker signals and longer-lived vibrational dynamics practical.

Beyond instrument advancements, we have partaken in the effort to provide clarity and develop the theory behind hybrid 2D Raman-THz spectroscopies. Our work identified competing non-resonant THz sum-frequency (two-photon) pathways in 2D-TTR spectroscopy, which may easily be misinterpreted as anharmonic contributions to the 2D spectra. This work further highlights the unique experimental circumstances common in ultrafast THz spectroscopies, in which broadband THz pulses are capable of inducing both resonant and non-resonant interactions. Our findings have prompted other hybrid 2D THz spectroscopies, such as 2D TIRV spectroscopy [1], to re-examine previous spectral interpretations to ensure the ac-

curacy of their analysis. While hybrid 2D Raman-THz spectroscopies were initially proposed to investigate intermolecular interactions in liquids, significant research interests into photo-driven dynamics of phonon modes have drawn these techniques to a wide range of material applications. Our work on $LiNbO_3$ serves to demonstrate the rigorous experimental implementation and spectral interpretation of 2D-TTR spectroscopy that is necessary to extract insights that are foundational to coherent control applications, including excitation mechanisms, nonlinear coupling interactions, and the dominant source(s) of anharmonicity. Finally, in collaboration with National Yokohama University, we explored driven-phonon dynamics in TMDs, a type of layered semiconductor material, where we were able to overcome several experimental challenges (sample physical dimension, roughness, etc.) that are common in novel materials. Using 1D nonlinear THz spectroscopies, we gained insight into the excitation mechanism and important polarization selection rules, which are foundational to future investigations with 2D THz spectroscopies.

7.2 Future work

Fundamental phonon physics

A powerful aspect of 2D spectroscopies, in general, is the ability to resolve the temporal evolution of the system states after each field interaction. To date, most material systems investigated by 2D-TTR spectroscopies contain only few anharmonic modes within the bandwidth of the THz pulses. For samples with significant nonlinear contributions, substantial mixing of the phonon branches have been observed by complementary neutron scattering techniques [2]. Application of 2D-TTR spectroscopies on these samples will directly probe the photo-driven dynamics and may reveal the nature of these mixed states.

In addition, 2D-TTR spectroscopy may be applied to investigate the dependence of anharmonic lattice dynamics on atomic composition in materials. Our previous works have explored phonon dynamics in $LiNbO_3$ and WSe_2 and revealed the dominant excitation mechanisms to be a resonant and a sum-frequency process, respectively. A number of related material systems with identical space groups but different atomic compositions, including $LiTaO_3$, WS_2, and $MoTe_2$, provide natural targets to further understand the fundamental interplay between the two primary phonon excitation mechanisms in solids. With identical space groups, these materials will share many common properties, including the non-zero terms in the nonlinear susceptibility tensors, the symmetries of the phonon branches, and the polarization selection rules for the photo-induced phenomena. However, the

frequency positions, phase-matching conditions, and anharmonicities are distinct, due to changes in lattice constants and the electronic structures. For instance, preliminary 2D-TTR results for $LiTaO_3$ suggest that the dominant excitation pathway may be sum-frequency in nature, which is in stark contrast to the resonant nonlinear pathways observed for $LiNbO_3$. Additional experiments will be necessary to unveil the underlying phonon physics that led to this distinction.

Cascaded second order processes

A few recent reports have also suggested that excited phonons and phonon-polaritons can lead to strongly enhanced nonlinear coefficients due to their large induced distortions of the lattice, especially for second-order processes in materials. These enhanced second-order processes may produce cascaded-second order signals, which have been observed using THz imaging techniques and 1D nonlinear THz spectroscopies in $LiNbO_3$ [3] and ZnTe [4]. However, these signals have yet to be observed in the 2D-TTR spectra of the same materials for reasons that are currently unclear. Investigation into cascaded second-order processes in 2D-TTR spectroscopies may further enrich the current theoretical understanding of the competing excitation pathways in 2D-TTR spectroscopies. In particular, these samples may help build intuition for the interplay between second- and third-order nonlinearities in non-centrosymmetric crystals in 2D-TTR spectroscopy.

Spintronic THz emitters

Water and its hydrogen-bonding dynamics has remained a significant research focus in THz science. However, the weak nonlinear response of water and the rapid relaxation lifetimes ($\sim$ 100 fs) have made 2D-TTR spectroscopic investigations of water extremely challenging. Extension of single-shot detection schemes, which reduce experimental time by one to two orders-of-magnitude, have enabled measurements of 1D TKE spectra for water and aqueous solutions in our group. Advancing these 1D spectroscopic studies of water to 2D-TTR spectroscopy requires careful consideration of the instrument response function (IRF) due to their weak signal strength. The IRF of 2D-TTR spectroscopy is given as the product of the incident THz electric fields and the probe intensity envelope, which is simply approximated as a Gaussian function. Thus, the temporal extent and frequency complexity of the IRF is largely dependent on the THz pulse shapes. In our 2D-TTR spectrometer, we currently employ organic emitter crystals, such as DSTMS and DAST, which provides the highest possible THz field strengths with the drawback of an overall $\sim$ 500 fs few-cycle THz

pulse. Recall that the measured 2D-TTR signal is a convolution of the IRF and the molecular response function. The longer-lasting oscillatory tail in the generated THz pulse shape leads to complex spectral artifacts [5] that require rigorous removal through deconvolution routines to reveal the underlying weak molecular response of water. Hamm and coworkers have instead chosen to employ GaP as the THz emitter crystal for their 2D-RTT/TRT setup [6], which produces unipolar half-cycle THz pulses that result in clean and uniform IRFs. However, the achievable THz electric field strength is roughly two orders-of-magnitude lower for GaP compared to that of organic crystals, which makes it impractical for 2D-TTR spectroscopy where two THz pump pulses are required.

A novel type of THz emitter based on ultrafast spin currents in nanofilms, known as spintronic THz emitters (STE) [7], have gained significantly attention recently due to their ultra-broadband performance (up to 30 THz), ease of use (colinear THz emission; agnostic to pump wavelength and polarization), and flexible tunability through tailored external magnetic fields. In particular, commercial suppliers have recently manufactured large-area STEs that, when properly focused to a near diffraction-limited spot size, can achieve THz electric field strengths of order MV/cm, which is lower than organic emitters but remains sufficient for nonlinear THz spectroscopies. Further, the generated ultra-broadband THz pulses can be tailored to be one- or two-cycle, which simplifies the IRF of 2D-TTR spectroscopy. Thus, STEs may provide the right trade-offs between THz field strength and IRF complexity to enable the investigation of elusive hydrogen-bonding dynamics and anharmonicities in water.

References

[1] Laura Vietze et al. “Distinguishing different excitation pathways in two-dimensional terahertz-infrared-visible spectroscopy.” *Journal of Chemical Physics* 154.17 (2021).

[2] Yang Shen et al. “Anharmonic origin of the giant thermal expansion of NaBr.” *Physical Review Letters* 125.8 (2020), p. 085504.

[3] Bo Wang et al. “Observation of Kerr nonlinearity and Kerr-like nonlinearity induced by terahertz generation in LiNbO3.” *Applied Physics Letters* 114.20 (2019).

[4] Jean P. Caumes et al. “Kerr-like nonlinearity induced via terahertz generation and the electro-optical effect in zinc blende crystals.” *Physical Review Letters* 89.4 (2002), pp. 4–7.

[5] Griffin Mead et al. “Sum-frequency signals in 2D-Terahertz-Terahertz-Raman spectroscopy.” *The Journal of Physical Chemistry B* 124.40 (2020), pp. 8904–8908.

[6] Janne Savolainen, Saima Ahmed, and Peter Hamm. “Two-dimensional Raman-terahertz spectroscopy of water.” *Proceedings of the National Academy of Sciences* 110.51 (2013), pp. 20402–20407.

[7] Ruidong Ji et al. “Tunable multi-cycle terahertz pulse generation from a spintronic emitter.” *Applied Physics Letters* 123.21 (2023).

Appendix A

OPERATION PROCEDURES FOR THE NONLINEAR THZ SPECTROMETER

In this appendix chapter, I will provide a basic operation manual for the home-built nonlinear THz spectroscopy system. Specific procedures for the alignment and maintenance of the laser and spectroscopy system can be found on CaltechDATA, which contains step-by-step instructions guided with photos. The procedures below assume the Micra oscillator, the Legend Elite amplifier, and the TOPAS OPA laser systems have been fully warmed up following the "Legend Turn-on Procedure." It also assumes that the spectrometer is generally well-aligned following the "2D-TTR realignment procedure."

Stage-scan control GUI

I have developed a dedicated GUI for both 1D TKE and 2D-TTR experiments, as shown in Fig. A.1. Comments have been added to note the usage of each input field and button. The GUI is written in Matlab's app designer. It communicates with several hardware components of the spectrometer to automate 1D and 2D spectroscopic measurements, including the optical delay stage controller (which controls both optical delay lines), sample delay stage controller, and the DAQ card.

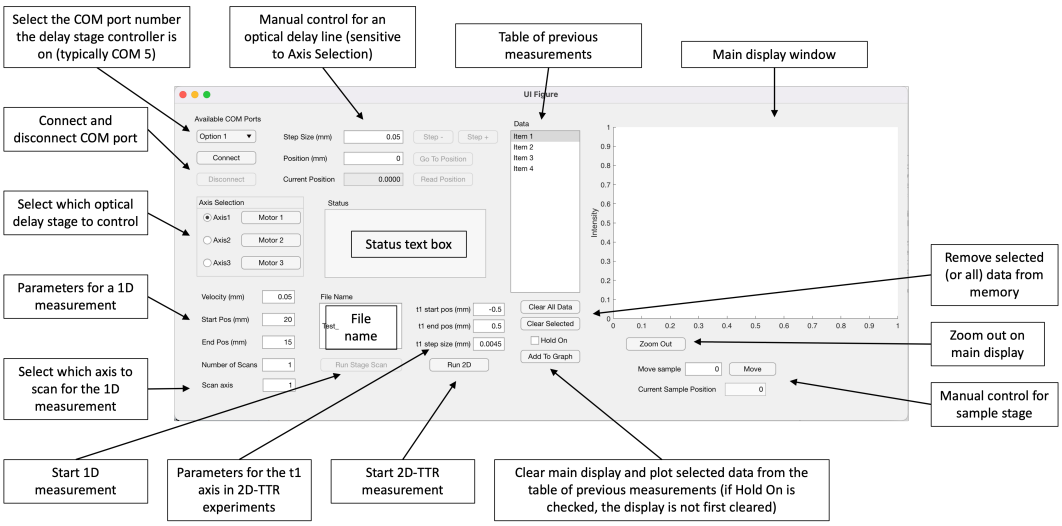

Figure A.1: Screenshot of the stage-scan control GUI.

Optimization for nonlinear THz spectroscopy

This section describes the optimization factors that are essential for both 1D and 2D THz spectroscopic measurements. The order in which they are listed reflects the general order of operation. Note that depending on the signal strength of the sample and the alignment condition of the spectrometer, earlier steps may be omitted. The common EO crystal GaP is used in the alignment steps to provide a convenient handle for optimization.

1. **Spatial and temporal overlap of the two THz pump pulses.** This is achieved by following the 2D EO imaging procedures with 100 μm GaP detailed in "2D-TTR realignment procedure" to characterize the THz beam profiles in real-time. THz pump B will be carefully walked and optimized to achieve precise spatial overlap with THz pump A. Temporal overlap will be achieved by adjusting delay line 2, which controls the optical path length of THz pump B. The position of the THz focus is obtained by minimizing the spot size on the GaP crystal surface with the sample delay stage. Note that the THz pump lines are considered aligned and fixed for all the later optimization steps. Thus, it is crucial to ensure the best possible THz focusing and spatial overlap before proceeding (see Chapter 3 for an example of well-aligned THz pulses). In general, several iterations of fine-adjustments on the GaP position and delay line 2 position would be necessary.

2. **Pump-probe spatial and temporal overlap.** In this step, it is crucial to keep the optimized THz optics fixed and only adjust optics on the probe beam path. Rough pump-probe spatial overlap is generally first achieved by eye. Next, we take advantage of the nonlinear electronic response of GaP (positioned at the THz focus from the previous step), which is maximized when the pump and probe pulses are temporally overlapped. For simplicity, the response from THz pump A is typically used in this step. Delay stage 1 may be manually adjusted or scanned using the GUI. Once a signal is observed on the lock-in amplifier, fine-adjust the delay stage 1 position to find the peak of the signal (temporal overlap).

3. **Optimization of the nonlinear THz response of GaP.** Again, adjustments are only made to the probe beam pointing in this step. Position delay line 1 at the peak of the GaP response. Fine-adjust the last two turning mirrors and the Barlow lens pair in the probe beam path to maximize the nonlinear

response. Then, fine-adjust the delay stage 1 position to maximize signal, as the adjustments will change the pump-probe temporal overlap slightly. Iterate these optimization steps until the signal is maximized.

Sample measurements with 1D TKE and 2D TTR spectroscopy

Successful execution of the previous optimization steps will result in optimized spatial overlap between the two THz pump pulses and the probe pulse at the focus. In addition, the delay stage positions for the temporal overlap of all three beams are also obtained. This section describes the procedures to measure a 1D or 2D spectra for a sample of interest.

1. **Optimization of the sample position.** The sample position is optimized with the computer controlled sample stage using the GUI. Due to the tight focusing of the OAP relay, the signal decreases sharply if the sample is mis-positioned. We are generally able to estimate the position for the sample based on the form factor of the mount and the optimized position for the GaP crystal in previous steps. We typically adjust the sample position in 0.1 mm increments to maximize signal.

2. **Measurement of 1D TKE spectra.** The 1D TKE spectra is measured by scanning delay line 1 (probe). The THz pump pulse with the desired polarization is let through. The output of the corresponding optical chopper is connected to the lock-in amplifier to supply the sync signal. Measurements are typically taken with a stage velocity of 0.03 mm/s and a lock-in amplifier time constant of 30 ms. If the stage velocity is set too high or the time constant too low, the signal will be broadened in the time domain and high frequency features may be altered. The temporal window is typically set to be $\sim$ 1 ps before and after the start and end of the signal. Depending on the signal strength, 10 to 100 averages are generally taken for our published data, which can take up to ~30 minutes per measurement. The GUI saves the settings of the run and each scan as individual files. The average spectra can be quickly obtained with the "make_avg.py" script in the data directory.

3. **Measurement of 2D-TTR spectra.** 2D-TTR spectra are time-consuming to measure, where each average generally takes ~2 hours. Thus, we generally perform several measurements along 1D slices of the 2D spectra prior to full 2D-TTR measurements to ensure we obtain high quality spectra. To set up a

2D-TTR experiment, the output of both optical choppers are connected to a frequency mixer, which generates the difference frequency at 166.66 Hz for the lock-in amplifier. To determine the temporal extent of the 2D-TTR signal, we measure two perpendicular 1D slices, one along the t_2 axis at $t_1 = 0$ ps (called the t_2 slice) and the other along the t_1 axis at $t_2 = 0$ ps (called the t_1 slice). Practically, these measurements are obtained by moving both delay stages to the temporal overlap position and scanning either delay stage 1 (t_2 slice) or 2 (t_1 slice). The temporal extent of the 2D-TTR signal is generally symmetric about $t_1 = 0$, with a dog-leg skew in the negative t_1 half due to the definition of the time variables [1]. Assuming the signal in the t_1 and t_2 slices span x and y ps, respectively, the full 2D-TTR spectra should span $-x$ to x ps along t_1 and -1 to $x + y$ ps along t_2 ($t_2 = 0$ is shifted horizontally by x ps in the negative half). The full 2D-TTR spectra may be measured with the GUI by inputting the t_1 and t_2 parameters into the appropriate fields and pressing the "Run 2D" button to start. The program moves delay stage 2 (t_1) in discrete steps (typically in 30 fs intervals) and scans along delay stage 1 (t_2). The scans are saved individually by the GUI program with the suffix denoting the delay stage 2 position. The program "combine_2D_stage_scan.py" may be used to combine the individual files into a 2D array file with the full time-domain 2D-TTR spectra.

References

[1] Ioan B. Magdău et al. "Interpretation of the THz-THz-Raman spectrum of bromoform." *The Journal of Physical Chemistry A* (2019), acs.jpca.9b05165.